Institute of Thermoelectricity, Academy of Sciences and Ministry of Education and Science of Ukraine

Journal of THERMOELECTRICITY

International Research

Founded in December, 1993

published 6 times a year

No. 4 *2013*

Editorial Board

International Editorial Board

Founders - National Academy of Sciences, Ukraine
Institute of Thermoelectricity of National Academy of Sciences and Ministry of Education and Science of Ukraine

Certificate of state registration № КВ 15496-4068 ПР

Editorial office manager D. Taschuk

Editors:

L. Vikhor, L. Kosyachenko, A. Farion, V. Kramar, V. Katerynchuk

Published by decision of Scientific Board of Institute of Thermoelectricity
of National Academy of Sciences and Ministry of Education and Science of Ukraine

Address of editorial office:
Ukraine, 58002, Chernivtsi, General Post Office, P.O. Box 86.
Phone: +(380-3722) 7 58 60.
Fax: +(380-3722) 4 19 17.
E-mail: jt@inst.cv.ua
http:// www.jt.cv.ua

Signed for publication 25.08.13. Format 70×108/16. Offset paper №1. Offset printing.
Printer's sheet 11.1. Publisher's signature 9.2. Circulation 400 copies. Order 6.

Printed by "Bukrek" publishers,
10, Radischev Street, 58000, Chernivtsi, Ukraine.

CONTENTS

P.V. Gorsky, V.P. Mikhalchenko

P.V. Gorsky

Institute of Thermoelectricity
NAS and MES of Ukraine, 1, Nauky Str.,
Chernivtsi, 58029, Ukraine

V.P. Mikhalchenko

METHOD FOR KINETIC COEFFICIENTS AVERAGING OVER THE SIZE OF PARTICLES AND ITS IMPACT ON PREDICTED FIGURE OF MERIT OF NANOSTRUCTURED THERMOELECTRIC MATERIAL

This paper deals with the four methods for averaging the electric conductivity and lattice thermal conductivity of nanostructured thermoelectric material over the size of particles, namely effective medium method with regard to the volume share of various-size particles, effective medium method with regard to the fraction of various-size particles, simple averaging of kinetic coefficients with regard to the volume share of various-size particles and simple averaging of kinetic coefficients with regard to the fraction of various-size particles. These methods are used for the calculation of dimensionless thermoelectric figure of merit of material with respect to a single crystal depending on the most probable radius of its particle based on the model Rayleigh distribution. Moreover, for comparison, dimensionless thermoelectric figure of merit of material is calculated on the assumption of equal size of its particles. Calculations have been made for the case of Bi_2Te_3 It is shown that despite the difference in the results obtained by these methods, in all the cases there is an optimal radius of thermoelectric material particle, whereby its dimensionless thermoelectric figure of merit is maximum. This radius lies in the range of 0.02 – 0.04 μm, and its respective dimensionless thermoelectric figure of merit at 300 K is of the order of 2.08 ÷ 2.12 with respect to a single crystal on condition that cleavage planes of individual particles are oriented parallel to temperature gradient and electric current, and there are no thermopower losses when passing from a single crystal to nanostructured thermoelectric material.

Key words: nanostructured material, thermoelectric figure of merit, phonons, electrons, scattering, relaxation time, normal processes, Umklapp processes, Rayleigh distribution, effective medium method, averaging over size.

Introduction

Methods for determination of the effective kinetic coefficients of thermoelectric material produced by hot pressing, extrusion or spark plasma sintering techniques via the kinetic coefficients of its component particles or, in other words, its shape-forming elements, have been considered in a variety of theoretical papers [1-4]. These methods can be divided into two big classes, namely the methods based on solving phenomenological equations of electric and thermal conductivity for shape-forming elements and the methods based on constructing from shape-forming elements of the so-called "effective thermoelectric medium". The former in the strict sense of the word is applicable only when the characteristic sizes of shape-forming elements of material structure are much in excess of the characteristic mean free paths of charge carriers and phonons, and, hence, their application to nanostructured thermoelectric materials based on Bi_2Te_3 provokes certain objections from the authors of this paper. These objections are as follows. First, the mean free path, for instance, of electrons in Bi_2Te_3 at 300 K is of the order of 36 nm [5], hence, phenomenological equations for electric potential distribution are hardly applicable to particles of

comparable or, the more so, smaller dimensions. Second, the lattice conductivity of Bi_2Te_3 at 300 K and higher temperature is mainly caused by phonon Umklapp processes [6]. If such processes are available, the relaxation time of phonons with their mutual scattering is a function of frequency ω, and, hence, introduction of phonon mean free path in the usual sense of this concept is hardly possible, though some formal parameter having dimensions of length and depending on scattering mechanisms, namely $l_p(\omega) = \nu\tau(\omega)$, where ν – average sound velocity in material, $\tau(\omega)$ – phonon relaxation time, can be introduced. The disadvantage of this method is also the fact that the analytical solution of phenomenological equations for arbitrary-shaped particles, the more so with account of thermoelectric effects, is difficult or impossible, and one has to resort to somewhat artificial simulation of this shape. On the other hand, the effective medium method also requires certain modification with regard to thermoelectric phenomena. Some aspects of this problem have been considered in [4].

Taking into account the foregoing, our purpose in this paper is to consider and compare a number of methods for determination of the effective kinetic coefficients of nanostructured thermoelectric material with regard to size distribution of its particles. The methods in hand do not call for solution of phenomenological equations of thermal conductivity and thermal conductivity for an individual nanoparticle.

Kinetic coefficients of a nanoparticle as a function of its size

We first will determine the electric conductivity of an individual nanoparticle as a function of its size. To simplify the calculations, the nanoparticle will be considered to be spherical. Moreover, we will take into account that the electric conductivity of Bi_2Te_3 at temperatures 300 K and higher is determined by the acoustic phonon deformation potential scattering charge carriers. And for this case the approximation of constant mean free path is valid. Therefore, the ratio between the electric conductivity $\sigma_n(r)$ of a nanoparticle of radius r and the electric conductivity σ_0 of a single crystal will give:

$$\sigma_n(r)/\sigma_0 = 1.5\int_0^1\int_{-1}^1 \frac{(r/l_e)\sqrt{y^2+2zy+1}\,y^2\,dz\,dy}{(r/l_e)\sqrt{y^2+2zy+1}+1}. \tag{1}$$

In this formula, l_e is the electron mean free path. Double integral here results from averaging the expression for the electric conductivity over the mean free paths inside the sphere. It can be shown that within this approximation the thermopower is not changed, as long as both thermal diffusion flux and electric current are proportional to relaxation time. Therefore, a change in thermoelectric figure of merit in this case is completely governed by a change in the electric conductivity – thermal conductivity ratio.

We now turn to determination of lattice thermal conductivity of a nanoparticle with regard to both phonon Umklapp processes and normal processes. The ratio between the thermal conductivity κ_n of a nanoparticle of radius r and the thermal conductivity κ_0 of a single crystal, provided its cleavage planes oriented in parallel to temperature gradient in conformity with the results of [7-9] is determined by the expression:

$$\kappa_n/\kappa_0 = 1.5\int_0^1\int_0^1\int_{-1}^1 \frac{z^2x^4\exp(x/\theta)}{\left[\exp(x/\theta)-1\right]^2}\left(\frac{(r/L^*)\sqrt{z^2-2zy+1}}{1+(r/L^*)Q_{l\|}(x)\sqrt{z^2-2zy+1}}+\right.$$
$$\left.+\frac{2(r/L^*)\sqrt{z^2-2zy+1}}{1+(r/L^*)Q_{t\|}(x)\sqrt{z^2-2zy+1}}\right)dy\,dz\,dx\left\{\int_0^1\frac{x^4\exp(x/\theta)}{\left[\exp(x/\theta)-1\right]^2}\left(\frac{1}{Q_{l\|}(x)}+\frac{2}{Q_{t\|}(x)}\right)dx\right\}^{-1}. \tag{2}$$

In so doing, $L^* = \rho\hbar^4\nu_{\|}^6/\gamma^2(k_BT_D)^5$, where ρ is the material density, $\nu_{\|}$ is the sound velocity in it along the direction of cleavage planes, γ is the Gruneisen parameter, k_B is the Boltzmann constant, T_D is the Debye temperature, $\theta = T/T_D$, the rest of designations are generally accepted. Frequency polynomials $Q_{l\|}(x)$ and $Q_{t\|}(x)$ are of the form:

$$Q_{l\|}(x) = x^4 + \mu_{\|}x, \tag{3}$$

$$Q_{t\|,\perp} = \left(\mu_{\|} + 3.125\theta^3\right)x. \tag{4}$$

where $\mu_{\|} = 0.022$ for Bi_2Te_3 [7-9].

Determination of the effective kinetic coefficients of material as a whole

In the determination of the effective kinetic coefficients of nanostructured thermoelectric material as a whole, for simplicity of calculations we will ignore the influence of material pores on these coefficients, i.e. we will not consider the effects of tunnelling or charge carrier emission, as well as convective and radiation mechanisms of energy transfer and the effects related to intercommunication of pores. Then, with account of particle size distribution function $w(r)$, these coefficients can be determined by the four different methods.

The first method consists in using the Odelevsky formula [1] with regard to the volume share of various-size particles. In this case the effective electric conductivity σ_{ef} and thermal conductivity κ_{ef} of material as a whole are determined as solutions of the following equations:

$$\int_0^\infty \frac{\sigma_{ef} - \sigma_n(r)}{2\sigma_{ef} + \sigma_n(r)} r^3 w(r)\,\mathrm{d}r = 0, \tag{5}$$

$$\int_0^\infty \frac{\kappa_{ef} - \kappa_n(r)}{2\kappa_{ef} + \kappa_n(r)} r^3 w(r)\,\mathrm{d}r = 0. \tag{6}$$

The second method consists in using the Odelevsky formula with regard to the fraction of various-size particles. In this case equations (5) and (6) acquire the form:

$$\int_0^\infty \frac{\sigma_{ef} - \sigma_n(r)}{2\sigma_{ef} + \sigma_n(r)} w(r)\,\mathrm{d}r = 0, \tag{7}$$

$$\int_0^\infty \frac{\kappa_{ef} - \kappa_n(r)}{2\kappa_{ef} + \kappa_n(r)} w(r)\,\mathrm{d}r = 0. \tag{8}$$

The third method consists in averaging the electric conductivity and lattice thermal conductivity over the volume share of various-size particles. In this case the effective kinetic coefficients of nanostructured material are determined directly:

$$\begin{pmatrix}\sigma_{ef}\\ \kappa_{ef}\end{pmatrix} = \int_0^\infty \begin{pmatrix}\sigma_n(r)\\ \kappa_n(r)\end{pmatrix} r^3 w(r)\mathrm{d}r. \tag{9}$$

The fourth method consists in averaging the electric conductivity and lattice thermal conductivity over the fraction of various-size particles. In this case the ratio (9) acquires the form:

$$\begin{pmatrix}\sigma_{ef}\\ \kappa_{ef}\end{pmatrix} = \int_0^\infty \begin{pmatrix}\sigma_n(r)\\ \kappa_n(r)\end{pmatrix} w(r)\mathrm{d}r. \tag{10}$$

In Eqs. (5) – (8) normalization factors are omitted because they have no effect on the results of calculation of the effective kinetic coefficients, as well as in Eqs. (9) and (10), because they have no effect on the dimensionless thermoelectric figure of merit of nanostructured material with respect to a single crystal whose calculation in the framework of the outlined methods is the purpose of this paper.

For concrete calculations we take particle size distribution function $w(r)$ as follows:

$$w(r) = \frac{r}{r_0^2}\exp\left(-r^2/2r_0^2\right). \tag{11}$$

This particle size distribution function is called the Rayleigh distribution, which has been assumed because it is the simplest single-parameter distribution. Parameter r_0 is the most probable particle radius. This function, as it must be, satisfies normalization condition $\int_0^\infty w(r)\,\mathrm{d}r = 1$.

With regard to (11), the relations (5) – (10) acquire the form as follows:

$$\int_0^\infty \frac{\sigma_{ef} - \sigma_n\left(r_0\sqrt{2t}\right)}{2\sigma_{ef} + \sigma_n\left(r_0\sqrt{2t}\right)}\sqrt{t^3}\exp(-t)\,\mathrm{d}t = 0, \tag{12}$$

$$\int_0^\infty \frac{\kappa_{ef} - \kappa_n\left(r_0\sqrt{2t}\right)}{2\kappa_{ef} + \kappa_n\left(r_0\sqrt{2t}\right)}\sqrt{t^3}\exp(-t)\,\mathrm{d}t = 0, \tag{13}$$

$$\int_0^\infty \frac{\sigma_{ef} - \sigma_n\left(r_0\sqrt{2t}\right)}{2\sigma_{ef} + \sigma_n\left(r_0\sqrt{2t}\right)}\exp(-t)\,\mathrm{d}t = 0\,, \tag{14}$$

$$\int_0^\infty \frac{\kappa_{ef} - \kappa_n\left(r_0\sqrt{2t}\right)}{2\kappa_{ef} + \kappa_n\left(r_0\sqrt{2t}\right)}\exp(-t)\,\mathrm{d}t = 0, \tag{15}$$

$$\begin{pmatrix}\sigma_{ef}\\ \kappa_{ef}\end{pmatrix} = \int_0^\infty \begin{pmatrix}\sigma_n\left(r_0\sqrt{2t}\right)\\ \kappa_n\left(r_0\sqrt{2t}\right)\end{pmatrix}\sqrt{t^3}\exp(-t)\,\mathrm{d}t, \tag{16}$$

$$\begin{pmatrix}\sigma_{ef}\\ \kappa_{ef}\end{pmatrix} = \int_0^\infty \begin{pmatrix}\sigma_n\left(r_0\sqrt{2t}\right)\\ \kappa_n\left(r_0\sqrt{2t}\right)\end{pmatrix}\exp(-t)\,\mathrm{d}t. \tag{17}$$

The results of calculation of the dimensionless thermoelectric figure of merit of the bulk nanostructured material based on Bi_2Te_3 with respect to a single crystal using different methods of determination of the effective kinetic coefficients are shown in Fig. 1.

It is seen from the figure that curves 1 and 3 coincide to a high degree of accuracy. This would imply that in determining the effective kinetic coefficients of thermoelectric material via the kinetic coefficients of shape-forming elements, instead of the Odelevsky formulae on condition of α = const one can employ the usual averaging over the volume share of particles with regard to size distribution function. In so doing, the maximum dimensionless thermoelectric figure of merit of the bulk nanostructured thermoelectric material, on condition that particle cleavage planes are oriented parallel to electric current and thermal flux, is a factor of $2.06 \div 2.1$ larger than the dimensionless thermoelectric figure of merit of a single crystal and is achieved with the most probable particle radius 0.02 μm. Curves

2 and 4 are also close to each other which means that in determining the effective kinetic coefficients of thermoelectric material by the fraction of particles with regard to size distribution function, instead of the Odelevsky formulae with a reasonable degree of accuracy one can also use the usual averaging of the kinetic coefficients by the fraction of various-size particles. With such method of averaging, the maximum dimensionless thermoelectric figure of merit of the bulk nanostructured thermoelectric material is a factor of 1.076 ÷ 2.082 greater than the dimensionless thermoelectric figure of merit of a single crystal and is achieved with the most probable nanoparticle radius 0.02 ÷ 0.03 μm. Curve 5 has been constructed on the assumption of equal size of all nanoparticles. In this case the maximum dimensionless thermoelectric figure of merit of the bulk nanostructured thermoelectric material is a factor of 2.12 greater than the thermoelectric figure of merit of a single crystal and is achieved with nanoparticle radius 0.03 μm. Hence it follows that the method of averaging in determining the effective kinetic coefficients of the bulk nanostructured thermoelectric material scarcely affects the predicted value of its dimensionless thermoelectric figure of merit, but markedly affects the estimation of the optimal value of the most probable particle radius.

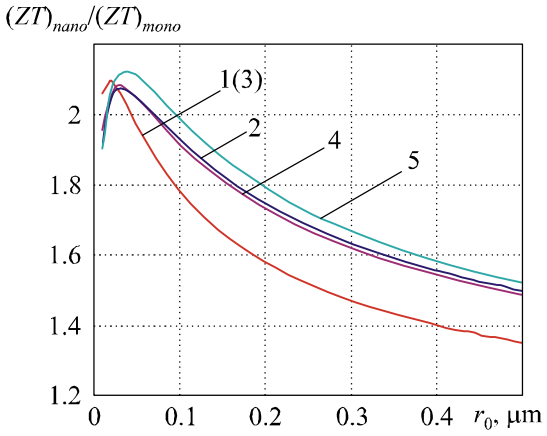

Fig. 1. Dependence of the dimensionless thermoelectric figure of merit of the bulk nanostructured thermoelectric material based on Bi_2Te_3 on the most probable particle radius with different methods of determination of the effective kinetic coefficients. Curve numbers 1 – 4 correspond to conventional serial numbers of averaging methods described in the text. Curve 5 corresponds to the case of zero particle size dispersion, where there is no need in averaging.

If equivalent-result methods for averaging over the volume share of particles with regard to size distribution function are assumed to be most correct, then the optimal value of the most probable particle radius of the bulk nanostructured thermoelectric material is 0.02 μm.

Conclusions and recommendations

1. This paper is concerned with the four methods of taking into account the size distribution of the bulk nanostructured thermoelectric material particles in determining its dimensionless thermoelecric figure of merit with respect to a single crystal.
2. The most correct are equivalent-result methods for determination of the effective kinetic coefficients of the bulk nanostructured thermoelectric material as a whole via the kinetic coefficients of shape-forming elements using the Odelevsky formulae with regard to the volume share of various-size particles and by simple averaging the electric conductivity and lattice thermal conductivity over the volume share of various-size particles. In this case, the maximum thermoelectric figure of merit of the bulk nanostructured material is about 2.1 times greater than the

thermoelectric figure of merit of a single crystal and is achieved with the most probable particle radius equal to 0.02 μm.

3. Determination of the effective kinetic coefficients of the bulk nanostructured thermoelectric material using the Odelevsky formulae with regard to the fraction of various-size particles and by simple averaging the electric conductivity and lattice thermal conductivity over the fraction of various-size particles yields the dimensionless thermoelectric figure of merit of the bulk nanostructure material which is about 2.076 ÷ 2.082 times greater than the thermoelectric figure of merit of a single crystal, this value being achieved with the most probable particle radius equal to 0.03 μm.
4. Determination of the effective kinetic coefficients of the bulk nanostructured material with neglect of size particle distribution yields the dimensionless thermoelectric figure of merit of the bulk nanostructured material 2.12 times greater than the thermoelectric figure of merit of a single crystal which is achieved at particle radius equal to 0.04 μm.
5. Thus, the method of averaging over particle size in determining the effective kinetic coefficients of the bulk nanostructured material with neglecting the influence of pores and tunneling effects scarcely affects the predicted maximum value of the dimensionless thermoelectric figure of merit of the bulk nanostructured material, but markedly affects the optimal value of the most probable radius of its particle that should be approached. Therefore, the most probable radius equal to 0.02 μm should be considered optimal on condition that size distribution of material particles is the Rayleigh distribution.

References

1. N.S. Lidorenko, O.M. Narva, L.D. Dudkin, and P.S. Yerofeev, Effect of Porosity and Quality of Intergrain Boundaries on the Electric and Thermal Conductivity of Semiconductor Thermoelectric Materials, *Inorganic Materials* **6**, 2112 – 2117 (1970).
2. L.P. Bulat, D.A. Pshenai-Severin, Tunneling Effect on the Thermoelectric Figure of Merit of the Bulk Nanostructured Materials, *Semiconductors* **52,** 2010, 452.
3. L.P. Bulat, V.V. Osvensky, Yu.N. Parkhomenko, and D.A. Pshenai-Severin, Study on the Possibilities of Thermoelectric Figure of Merit Improvement in Nanostructured Materials Based on Bi_2Te_3-Sb_2Te_3, *Physics of the Solid State* **54**, 20 – 26 (2012).
4. A.A. Snarskii, A.K. Sarychev, I.V. Bezsudnov, and A.N. Lagarkov, Thermoelectric Figure of Merit of the Bulk Nanostructured Composites with Distributed Parameters, *Semiconductors* **46**, 677 – 683 (2012).
5. B.M. Goltsman, V.A. Kudinov, and I.A. Smirnov, *Semiconductor Thermoelectric Materials Based on* Bi_2Te_3 (Moscow: Nauka, 1972), 320 p.
6. P.G. Klemens, Lattice thermal conductivity. In: *Solid State Physics. Advances in Research and Applications.* Vol. 7, pp. 1 – 98 (New York: Academic Press. Inc. Publishers, 1958), 526 p.
7. P.V. Gorsky, V.P. Mikhalchenko, Reduction of Thermoelectric Material Lattice Thermal Conductivity Using Shape-Forming Element Optimization, *J. Thermoelectricity* **1**, 18 – 25 (2013).
8. P.V. Gorsky, V.P. Mikhalchenko, On the electric conductivity of contacting particles of thermoelectric material, *J. Thermoelectricity* **2**, 12 – 18 (2013).
9. P.V. Gorsky, V.P. Mikhalchenko, Effect of Thermoelectric Material Anisotropy on the Electric Conductivity and Lattice Thermal Conductivity of its Contacting Particles, *J. Thermoelectricity* **3**, 5 – 10 (2013).

Submitted 28.03.2013.

C. de Tomás[1, 2], A. Cantarero[1], A.F. Lopeandia[2], F.X. Alvarez[2]

[1]University of Valencia, PO Box 22085, Valencia, 46071, Spain;
[2]Autonomous University of Barcelona, Bellaterra, Barcelona, 08193, Spain

LATTICE THERMAL CONDUCTIVITY OF SILICON NANOWIRES

We have calculated the lattice thermal conductivity of silicon nanowires using the Boltzmann transport equation for bulk phonons within the relaxation time approximation. The model includes anharmonic phonon scattering, both Umklapp and normal processes, the scattering of phonons due to isotopic disorder and the scattering by the boundaries, needed to avoid the divergence of the thermal conductivity at low temperatures. This minimum set of relaxation times allows us to verify the validity of the classical approaches in the study of the thermal conductivity of small diameter nanowires. From the comparison with experimental data for silicon nanowires, we conclude that the classical limit is valid for nanowires larger than 30 nm in diameter. There is no need to include the folding of acoustic phonons or confinement of optical phonons.
Key words: lattice heat conduction, semiconductor nanowires, Boltzmann transport equation.

Introduction

Semiconductors have a larger Seebeck (S) coefficient than metals and their thermal conductivity (κ) is not directly related to the electrical conductivity (σ) as is the case of the formers, through the Lorentz number $L = \kappa/\sigma T \approx 2.44 \times 10^{-8}$ W·Ω/K^2. The reason is that the heat flow in semiconductors is mainly due to phonons, i.e. the heat flow is dragged by the phonons, not by the electrons. The low carrier concentration as compared to metals makes the electrical contribution to the thermal conductivity negligible, at least in bulk materials. As it is well known, the fingerprint of this behavior is the typical T^3 law shown at low temperatures, instead of the linear behavior present in metals.

Actually, although for some applications it is important to have a large thermal conductivity in order to dissipate heat (microelectronic substrates, for instance), the large thermal conductivity of semiconductors is one of the drawbacks in the development of efficient thermoelectric devices. The reason is that the efficiency of a thermoelectric device is inversely proportional to the thermal conductivity. If we are able to decrease substantially the thermal conductivity, which in practice means to reduce it to that corresponding to the electronic contribution, we will drastically improve the efficiency of the thermoelectric device. Twenty years ago, Hicks and Dresselhaus [1] showed that the lattice thermal conductivity κ_L can be reduced by engineering different semiconductors or combining semiconductor alloys with different concentration in the form of superlattices. Quantum dots and, more recently, nanowires (NWs) are the subject of intensive research in the field of thermoelectricity [2].

The fast decrease of the thermal conductivity with decreasing nanowire diameter has been experimentally demonstrated [3]. On the other hand, several theoretical approaches have been published to account for the variation of κ_L with NW diameter [4-6]. In these works, phonon confinement, anharmonic processes by optical phonons at low temperature, or interface scattering with a variable specularity parameter, have been proposed to contribute to the lowering of the thermal conductivity in NWs. Unfortunately, several concepts have been used, many times with

unclear physical arguments: the need of a classical or quantum behavior, the presence of new scattering mechanisms like the decay of optical phonons into acoustical phonons, even at very low temperatures, interference scattering, while essential scattering mechanisms, like the existence of normal scattering processes, have been neglected. This panorama has contributed to mix up physical concepts and to the misunderstanding of the real physics behind the reduction of the lattice thermal conductivity in nanowires.

In the present work, we show that the behavior of the κ_L in semiconductor nanowires can be explained classically, in the whole temperature range, with an appropriate treatment of the different scattering processes, in particular the normal scattering processes, or *N*-processes. Phonon confinement, boundary scattering and other exotic processes are not necessary if the problem is correctly focused. The developed model predicts, using the parameters obtained from a fit of bulk silicon, the thermal conductivity of silicon nanowires down to 30 nm in diameter.

Lattice thermal conductivity derived from the Boltzmann transport equation

To deduce an eigenvalue solution of the Boltzmann transport equation (BTE), it is convenient to write it in terms of a symmetrized perturbed phonon distribution function,

$$N_q^*(r,t) = \frac{1}{2\sqrt{N_q^0\left(N_q^0+1\right)}} N_q(r,t), \tag{1}$$

where the equilibrium distribution function

$$N_q^0 = \frac{1}{e^{\hbar\omega/k_BT}-1}. \tag{2}$$

In Eq. (2), the phonon branch has been omitted for simplicity. The BTE for phonons, in a symmetric form [7] is:

$$\frac{\partial N_q^*(r,t)}{\partial t} + v_q \nabla N_q^*(r,t) = -\sum_{qq'} S_{qq'}^* N_q^*(r,t). \tag{3}$$

The scattering matrix which appears in the right hand side of Eq. (3) is symmetric in q and q'. The left-hand side operator, containing the time derivative and the convective term with the group velocity, is named drift operator. In general, the scattering matrix is unknown, but we can write it as

$$S_{qq'}^* = N_{qq'}^* + R_{qq'}^* \tag{4}$$

separating the normal and resistive processes. As it is well known [8], *N*-processes do not contribute in a direct way to the thermal conductivity, they only redistribute the energy and momentum between the different phonon modes and give rise to a drifted distribution function when we are not far from equilibrium:

$$N_q^0 = \frac{1}{e^{(\hbar\omega_q - \mu q_0)/k_BT}-1}. \tag{5}$$

At low temperatures, and neglecting boundary effects, we have partial information on the *N*-matrix, which appears in Eq. (4). Let us write the eigenvalue equation

$$\sum_{q'} N_{qq'}^* \phi_{q'}^\alpha = \lambda_\alpha \phi_q^\alpha. \tag{6}$$

It is straightforward to check that the matrix of the *N*-operator is diagonal and that there are, at least, four eigenvalues equal to zero. These eigenvalues correspond to the equilibrium distribution function given by Eq. (2) ($\lambda_0 = 0$) and to the drifted distribution function corresponding to Eq. (5) ($\lambda_1 = \lambda_2 = \lambda_3 = 0$). Thus, in the limit of low perturbation (low temperature gradient and low drift), the matrix corresponding to *N*-processes has the simple form [7]

$$N^* = \left(\begin{array}{c|ccc|ccc} 0 & 0 & 0 & 0 & & 0 & \\ \hline 0 & 0 & 0 & 0 & & 0 & \\ 0 & 0 & 0 & 0 & & 0 & \\ 0 & 0 & 0 & 0 & & 0 & \\ \hline & & & & \lambda_4 & & \\ & & & & & \lambda_5 & \\ 0 & 0 & 0 & 0 & & & \lambda_6 \\ & & & & & & & \ddots \end{array}\right) \equiv \left(\begin{array}{ccc} 0 & 0 & 0 \\ 0 & 0 & 0 \\ 0 & 0 & N_{22}^* \end{array}\right),$$

where the eigenvalues can be written in terms of

$$\lambda_4 = \lambda_5 = \lambda_6 = \ldots = \frac{1}{\tau_N} \tag{7}$$

the relaxation time in the limit where *N*-processes are dominant. On the other hand, the equilibrium distribution function is also an eigenvector of the *R*-operator with zero eigenvalue. The form of the BTE is, finally,

$$\left[\begin{pmatrix} 0 & 0 & 0 \\ 0 & 0 & 0 \\ 0 & 0 & N_{22}^* \end{pmatrix} + \begin{pmatrix} 0 & 0 & 0 \\ 0 & R_{11}^* & R_{12}^* \\ 0 & R_{21}^* & R_{22}^* \end{pmatrix} - \begin{pmatrix} D_{00}^* & D_{01}^* & 0 \\ D_{10}^* & D_{11}^* & D_{12}^* \\ 0 & D_{21}^* & D_{22}^* \end{pmatrix}\right]\begin{pmatrix} a_0 \\ a_1 \\ a_2 \end{pmatrix} = 0, \tag{8}$$

which gives rise to three equations:

$$\begin{gathered} D_{00}a_0 + D_{01}a_1 = 0 \\ -D_{10}a_0 + \left(R_{11} - D_{11}\right)a_1 + \left(R_{12} - D_{12}\right)a_2 = 0 \\ D_{21}a_1 + \left(N_{22} + R_{22} - D_{22}\right)a_2 = 0, \end{gathered} \tag{9}$$

where a_0 is a scalar, a_1 is a vector or order 3, and a_2 is a vector of infinite length. The dimensions of the matrices can be derived correspondingly. The eigenvectors a_j can be written, in general, as a linear combination of the eigenvectors of the *N*-operator. But, since we do not know a_2, we can combine the last two terms of Eq. (9) and we will have, finally, a set of two equations [7], containing a_0 and a_1, which gives rise to the energy conservation,

$$\frac{\partial \varepsilon}{\partial t} + \nabla j_Q = 0 \tag{10}$$

and to the vector equation

$$\frac{\partial j_Q}{\partial t} + \frac{1}{3}v^2 C_v \nabla T = -\left(\tau^{-1}\right)_{11} j_Q \tag{11}$$

representing the momentum conservation. We have made use of the fact that $\nabla\varepsilon = C_v \nabla T$, C_v being the specific heat and v the average group velocity. The term multiplying the heat current can be called phonon momentum relaxation operator, and it can be written in terms of the 3 × 3 matrices:

$$\left(\tau^{-1}\right)_{11} = R^*_{11} - R^*_{12}R^*_{21}\left(N^*_{22} + R^*_{22}\right)^{-1}. \tag{12}$$

In the steady state, Eq. (11) can be inverted and define a thermal conductivity operator, which will be also a 3×3 matrix. Considering the heat flow in the same direction of the temperature gradient, it is easy to arrive to the expression

$$j_Q = -\frac{1}{3}C_v v^2 \tau \nabla T, \tag{13}$$

where the average

$$\tau = \frac{\int \tau\omega^2 \frac{\partial f}{\partial \omega} D(\omega) \mathrm{d}\omega}{\int \omega^2 \frac{\partial f}{\partial \omega} D(\omega) \mathrm{d}\omega}. \tag{14}$$

Going to the limit where *N*-processes dominate, the following equation can be deduced:

$$R^*_{11} = 1/\langle \tau_R \rangle. \tag{15}$$

On the other hand, in the limit where *N*-processes are negligible,

$$R^{*-1}_{11} = \langle \tau_R \rangle. \tag{16}$$

We can combine the equations of the resistive matrix and its inverse and deduce the non-diagonal terms,

$$R^*_{11} = \sqrt{R^*_{11}\left[R^*_{11} - 1/R^{*-1}_{11}\right]}. \tag{17}$$

The final expression of the momentum relaxation time is

$$\tau_{11} = \langle \tau_R \rangle \frac{\tau_N + \langle \tau_R^{-1} \rangle^{-1}}{\tau_N + \langle \tau_R \rangle} \tag{18}$$

and the thermal conductivity has the expression

$$\kappa = \frac{1}{3}C_v v^2 \left[\langle \tau_R \rangle (1-\Sigma) + \langle \tau_R^{-1} \rangle^{-1} \Sigma\right], \tag{19}$$

where we have defined the switching factor

$$\Sigma = \frac{\langle \tau_R \rangle}{\tau_N + \langle \tau_R \rangle}. \tag{20}$$

At low temperature, when the *N*-processes dominate, the switching factor is 1 and the second term of the thermal conductivity expression is dominant. This temperature regime is called the Ziman regime [9]. On the other hand, when the normal processes are negligible (at very high temperatures) the switching factor is zero and the first term dominates. This is called the kinetic regime. The switching factor thus indicates the dominant regime and, depending on its value, the conductivity "switches" from one regime to the other.

In spite of the isotropic boundary relaxation time, it is convenient to introduce a geometrical factor taking into account the sample geometry. Guyer and Krumhansl [10] did it for cylindrical geometry, but in terms of a complicated expression containing cylindrical Bessel functions. Here, we have used a geometrical factor derived from non equilibrium irreversible thermodynamics for any geometry, in particular valid for nanowires [11]. The expression of the geometrical factor is very simple,

$$F\left(\frac{\ell}{L_{eff}}\right)=\frac{1}{2\pi^2}\frac{L_{eff}^2}{\ell^2}\left(\sqrt{1+4\pi^2\frac{\ell^2}{L_{eff}^2}}-1\right), \tag{21}$$

where the phonon mean free path

$$\ell = v\tau \tag{22}$$

depends on the temperature through the scattering mechanisms (relaxation time) and L_{eff} is the effective size of the sample. In the case of nanowires, $L_{eff} = d$, the diameter of the nanowire. Since the mean free path of the phonons is much larger that the diameter of the nanowires, the geometrical factor will be basically

$$F\left(\frac{\ell}{L_{eff}}\right)=\frac{L_{eff}}{\pi\ell}. \tag{23}$$

Introducing the geometrical factor into the expression for the lattice thermal conductivity, we obtain

$$\kappa = \kappa_K\left(1-\Sigma\right)+\kappa_Z F\left(\frac{\ell}{L_{eff}}\right)\Sigma, \tag{24}$$

which is the final expression used to calculate the thermal conductivity.

Lattice dynamics and phonon relaxation times

The lattice thermal conductivity is proportional to the average phonon group velocity. This is the reason why the acoustic longitudinal branches are contributing in great extent to the heat transport. Optical phonons do not contribute, basically, since the dispersion is very small. For a confident calculation of the thermal conductivity, a reliable model of the lattice dynamics is needed. In this work, we have used the bond charge model of Weber [12] and its original data. The advantage of the bond charge model is that utilizes a minimum set of parameters and reproduces quite well even the flat region of the acoustical branches close to the border of the Brillouin zone (BZ), and it can be extended to other technologically interesting compounds [13].

In undoped semiconductors, the most important scattering mechanisms are phonon-phonon processes or phonon anharmonicity. At high temperatures, the Umklapp processes are dominant. Recently, Ward and Broido [14] have performed ab initio calculations of the thermal conductivity of bulk silicon in the temperature range from 100 to 800 K. In this temperature range, boundary scattering is of no importance and was not taken into account. They deduced a functional form for the relaxation time of *U*-processes which has been corrected by us to account for the low temperature behavior (below 100 K):

$$\tau_U^{-1} = B_U\omega^4 T e^{-\Theta_U/T}\left[1-e^{-3T/\Theta_D}\right]. \tag{25}$$

The extra term $e^{-\Theta_U/T}$ limits the efficiency of *U*-processes at low temperature. Since *U*-processes do not conserve momentum, the sum of three (or four) phonon wave vectors must be as large as a reciprocal lattice vector, and this is not possible at low temperatures. If we consider a phonon energy of the order of *kT* and draw a horizontal line in the dispersion relations, clearly the phonon wave vectors are far from the limit of the BZ. In order to select Θ_U and not to use it as a fitting parameter, we have divided the BZ into three and looked at the crossing point of the acoustical longitudinal branch, giving us a phonon energy, which can be transformed into temperature dividing the Boltzmann

constant. Concerning the relaxation time for *N*-processes, the expression of Ward and Broido [14] does not behave properly at low temperatures as well, where the temperature behavior must follow the T^3 law. We have added an extra term to account for this behavior:

$$\tau_N^{-1} = \left(\frac{1}{B_N T} + \frac{1}{B'_N T^3} \right)^{-1} \omega^2 \left[1 - e^{-3T/\Theta_D} \right]. \tag{26}$$

Silicon, or any other material, has an isotopic disorder in its natural form [15]. In particular, *Si* has only three stable isotopes, ^{28}Si, with 92.2297(7) % abundance, ^{29}Si, with 4.6832(5) % abundance, and ^{30}Si, with 3.0872(5) % abundance. The isotopic disorder is a very important mechanism in the undoped materials. Isotopically pure *Si*, for instance, has thermal conductivity one order of magnitude larger than natural *Si* [16]. A well established expression for isotopic disorder or mass defect scattering relaxation time is [17]:

$$\tau_I^{-1}(q) = A\omega^4(q) = \frac{V_0 g}{4\pi} \frac{\omega^4(q)}{v^3(q)}, \tag{27}$$

where the factor *g* gives the mass fluctuation,

$$g = \sum_i f_i \left(\frac{\bar{M} - M_i}{M_i} \right)^2, \tag{28}$$

f_i is the mass fraction, $\bar{M}$ is the average mass and M_i is the mass of individual isotopes. Finally, in order to fit the low temperature region and limit the thermal conductivity to finite values, it is necessary to introduce a relaxation time to account for the boundary (otherwise the thermal conductivity diverges at low temperature) [9]:

$$\tau_B^{-1}(q) = \frac{v(q)}{L_{eff}}. \tag{29}$$

In the last two expressions, the parameters have been obtained from the literature. Our model has three parameters that correspond to the phonon-phonon relaxation times: B_U, B_N and B'_N.

Results and discussion

Figure 1 shows the fitting of our model, using Eq. (24) with the relaxation times given by Eqs. (25 – 27) and (29), for natural silicon. The Mathiessen rule has been used to calculate the average relaxation time. The experimental data are from Inyushkin et al. [16], which gives an effective length of the sample of 2.8 mm. The fitting of natural silicon provides us the following parameters: $B_U = 1.8 \times 10^{-46}$ s^3·K^{-1}, $B_N = 2.0 \times 10^8$ s·K^{-1}, and $B'_N = 1.9 \times 10^{-23}$ s·K^{-3}. The dots in Fig. 1 correspond to the experimental data [16], while the solid line is the theoretical fit with the parameters given above. The two contributions, Ziman (dashed line – green on line) and kinetic (dotted line – navy on line), to the thermal conductivity have also been plotted in the graph. The Ziman contribution, dominant when the switching factor approaches 1, is the most important at low temperature, while the kinetic contribution ($\sum = 0$) is more important at high temperatures. However, in the temperature range starting in 50 K to higher temperatures, we can observe that both contributions are necessary to obtain a reasonable fit of the thermal conductivity. That means that *N*-processes are also important at high temperature. Actually, in the work of Ward and Broido [16], where both relaxation times have been depicted as a function of frequency, they are of the same order of magnitude in the region of 10 – 15 THz (at 300 K). Clearly, *N*-processes cannot be neglected even at room temperature.

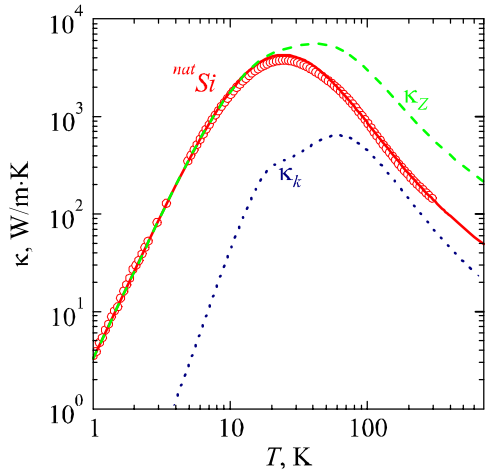

Fig. 1. Fitting of natural Si with the parameters given in the text. The open circles are the experimental data of Inyushkin et al. [16], while the solid line is the theoretical fitting. The dashed line (green online) is the Ziman contribution to the thermal conductivity, while the dotted line (navy online) is the kinetic contribution.

The contribution of isotopic disorder is concentrated basically in the region of 10 – 30 K, around the peak of the thermal conductivity. In the case of isotopically pure *Si* [16], only this region is affected by the disorder.

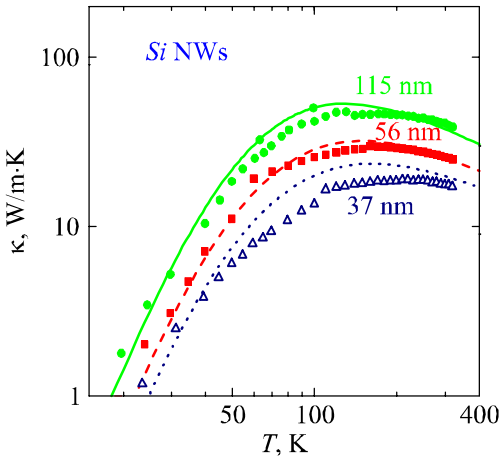

Fig. 2. Calculation of the thermal conductivity of nanowires with three different diameters using the model parameters obtained from the fitting of natural Si.

Figure 2 shows the calculated values of the thermal conductivity, using Eq. (24) with the parameters which fits the bulk silicon, for three different *Si* nanowires, with 115 (dots and solid line – green on line), 56 (full squares and dashed line – red on line) and 37 nm (up triangles and dotted line – navy on line). The only additional parameter which differs from the fitting to bulk silicon is the effective length of the sample, i.e. the diameter of the nanowire. At a given temperature (a given phonon mean free path), the thermal conductivity is reduced basically to the geometrical factor (in the approximated expression F is proportional to the nanowire diameter). By comparing the 115 nm NW with that of 37 nm, the reduction in the thermal conductivity at 50 K is two times larger than at room temperature. The reason is that at room temperature, the kinetic factor has a larger influence and the geometrical factor plays a smaller role. It was shown several years ago [18] that optical confinement in nanowires is important when the NW diameter is or the order of 2 – 3 nm. In the case of folded acoustic phonons, the experience can tell us that above 10 – 15 nm diameter, the number of phonon branches is so high that the use of a model considering the folding or a model considering bulk phonons will give a similar result on

the thermal conductivity. The essential points are the scattering mechanisms and, in particular, the correct treatment of *N*-processes, without neglecting the influence of the geometry.

Conclusions

A theoretical model able to predict the thermal conductivity of semiconductor nanowires has been proposed. The model considers properly phonon-phonon scattering. A geometrical factor has been included to account for the nanowire dimensions. A reliable model for the lattice dynamics with bulk phonons has been used. A minimum set of relaxation times has been taken into account in order to prove the validity of the model in the case of silicon nanowires down to 30 nm in diameter. Possibly, phonon folding effects are important below 10 – 15 nanometers.

Acknowledgements. The authors are grateful to the Ministry of Finances and Competitiveness of Spain for financial support through Grants CSD2010-00044 of the Programme ‘‘Consolider Ingenio 2010’’ and MAT2012-33483. Thanks are due to the University of Valencia for the use of the supercomputer TIRANT.

References

1. L.D. Hicks and M.S. Dresselhaus, *Phys. Rev.* B **47**, 16631 (1993).
2. J.P. Heremans, *Acta Phys. Pol.* A **108**, 609 (2005).
3. D. Li, Y. Wu, P. Kim, L. Shi, P. Yang, A. Majumdar, *Appl. Phys. Lett.* **83**, 2934 (2003).
4. M. Kazan, G. Guisbiers, S. Pereira, M.R. Correia, P. Masri, A. Bruyant, S. Volz, P. Royer, *J. Appl. Phys.* **107**, 083503 (2010).
5. P. Chantrenne, J.L. Barrat, X. Blase, J.D. Gale, *J. Appl. Phys.* **97**, 104318 (2005).
6. N. Neophytou, H. Kosina, *Phys. Rev.* B **83**, 245305 (2011).
7. R.A. Guyer, J.A. Krumhansl, *Phys. Rev.* **148**, 766 (1966).
8. I.G. Kuleev, I.I. Kuleev, J. Exp. *Theor. Phys.* **95**, 480 (2002).
9. J.M. Ziman, Electrons and phonons (Clarendon Press, Oxford), 1979.
10. R.A. Guyer, J.A. Krumhansl, *Phys. Rev.* **148**, 778 (1966).
11. F.X. Alvarez, D. Jour, and A. Sellitto, *J. Appl. Phys.* **105**, 014317 (2009).
12. W. Weber, *Phys. Rev. Lett.* **33**, 371 (1974).
13. J. Camacho and A. Cantarero, *Phys. Stat. Sol.* (b) **215**, 181 (1999).
14. A. Ward, D.A. Broido, *Phys. Rev.* B **81**, 085205 (2010).
15. F. Widulle, T. Ruf, A. Gobel, I. Silier, E. Schonherr, M. Cardona, J. Camacho, A. Cantarero, W. Kriegseis, V.I. Ozhogin, *Physica* B **263**, 381 (1999).
16. A.V. Inyushkin, A.N. Taldenkov, A.M. Gibin, A.V. Gusev, and H.J. Pohl, *Phys. Stat. Sol.* (c) **1**, 2995 (2004).
17. P.G. Klemens, Proc. Phys. Soc. London Sect. A **68**, 1113 (1955).
18. F. Comas, A. Cantarero, C. Trallero-Giner, M. Moshinsky, *J. Phys. Cond. Matt.* **7**, 1789 (1995); F. Comas, C. Trallero-Giner and A. Cantarero, *Phys. Rev.* B **47**, 7602 (1993).

Submitted 30.05.2013.

A.V. Budnik, E.I. Rogacheva, A.Yu. Sipatov

National Technical University "Kharkiv Polytechnic Institute"
21, Frunze Str., Kharkiv, 61002, Ukraine

EFFECT OF FABRICATION TECHNIQUE ON THE STRUCTURE AND THERMOELECTRIC PROPERTIES OF Bi_2Te_3 FILMS

Considerable increase in thermoelectric (TE) figure of merit of Bi_2Te_3 thin films under the effect of annealing has been emphasized in several papers. However, there are practically no works on the effect of annealing on TE properties and structure of Bi_2Te_3, films prepared by one-source thermal evaporation in vacuum. This investigation is concerned with unannealed and annealed at 500 K for 1 hour Bi_2Te_3 thin films of thickness d ~ 200 nm, prepared by one-source thermal evaporation in vacuum using different initial charge compositions (60 and 62.8 at.% Te) and different substrate temperatures (T_{sub} = 320 – 500 K). It is shown that regardless of the initial charge composition and substrate temperature, annealing contributes to structural perfection of Bi_2Te_3 films and formation of a well-expressed texture, however, unlike the films grown from a charge with 60 at.% Te, TE power P of films prepared from a charge with Te excess is reduced. Optimal parameters of Bi_2Te_3 films growth have been determined, yielding maximum P values comparable to TE power of films prepared by more costly and labour-consuming methods.

Key words: bismuth telluride, film, annealing, structure, thermoelectric properties.

Introduction

Semiconductor compound Bi_2Te_3 and solid solutions on its basis are among the best low-temperature thermoelectric (TE) materials possessing TE figure of merit Z within $1.0 – 2.9 \cdot 10^{-3}$ K^{-1} [1-3]. These materials have found a wide application when creating coolers, temperature and infrared sensors and other TE devices.

New vistas for practical application of low-dimensional structures draw attention to investigation of bismuth telluride in the thin-film state. Bi_2Te_3 films are prepared by various methods: molecular-beam epitaxy, magnetron sputtering, hot wall, liquid-phase epitaxy, laser evaporation, two-source thermal evaporation, etc. [4-10].

It is known that annealing produces a considerable effect on TE properties of Bi_2Te_3 [4-9]. Owing to recrystallization and homogenization during annealing, the material approaches the equilibrium state, the degree of perfection of crystalline structure is improved, the size of grains is increased, the width of their boundaries is reduced and well-expressed texture is formed. These processes are particularly important in the fabrication of bismuth telluride films tending to formation of concentration inhomogeneities during crystallization, resulting in the emergence of additional antisite defects and concentration growth of major charge carrier [4-10]. On the other hand, high-temperature annealing can lead to activation of tellurium re-evaporation processes, violating film stoichiometry and causing formation of additional number of defects.

It should be also noted that positive impact of annealing on TE and galvanomagnetic properties of Bi_2Te_3 films differs essentially with the use of different sputtering methods. Thus, for films prepared by one-source magnetron sputtering just a slight growth of TE power P (by ~ 20 %) is recorded [4],

whereas for films prepared with the use of molecular beam epitaxy (MBE), P is increased by a factor of almost 4. In so doing, all the works mention the emergence of a well-expressed texture and grain size increase in the structure of annealed films. In the majority of papers [4-6], films with the best TE properties were obtained after annealing for 1 hour at T_a = 570 K, though with the use of two-source magnetron sputtering [7] optimal film parameters were observed after 8 hours of annealing at T_a = 470 K. This indicates the necessity of special research of the effect of annealing for each method of growing the Bi_2Te_3 films.

One of the simple, accessible and cheap methods for preparation of bismuth telluride films is one-source thermal evaporation in vacuum. As compared to other, technologically more complicated methods, such as molecular beam epitaxy, it requires considerably less time for the fabrication of one film, which is important for large production volumes. However, the main disadvantage of this method is a restricted control of evaporation process resulting in formation of microstresses, concentration inhomogeneities and defects in synthesized films. This disadvantage can be at least partially removed by annealing.

The subject of research are bismuth telluride thin films of thickness $d \sim 200$ nm, prepared by one-source thermal evaporation in vacuum with the use of different initial charge compositions (60 and 62.8 at.% *Te*) and different substrate temperatures (T_{sub} = 320 – 500 K), and unannealed and annealed at a temperature of T_a = 500 K for 1 hour.

The purpose of the work is to study the effect of annealing on TE properties of Bi_2Te_3 films.

Experimental procedure

Polycrystalline samples of both stoichiometric composition (60.0 at. % *Te*) and with tellurium excess (62.8 at. %), used as a charge for preparation of films, were made by direct alloying of *Bi* and *Te* components of high purity (99.999 %). The initial components were placed into quartz ampoules, evacuated (to $\sim 10^{-5}$ Pa), then synthesized at a temperature of 800 K with subsequent annealing at 670 K within 300 hours.

Films were grown by thermal evaporation of charge in oil-free vacuum ($10^{-5} – 10^{-6}$ Pa) and subsequent condensation on glass substrates heated to temperatures in the range of T_{sub} = 320 – 500 K. Annealing was performed directly in the installation, immediately after evaporation of the film. The accuracy of measuring substrate temperature T_{sub} was 5 %. Prior to evaporation, the substrates were consecutively cleaned with acid, distilled water and alcohol. Film thickness d and condensation rate were controlled by means of a calibrated quartz resonator located beside the substrates. The resonator calibration for films up to 100 nm thick was made with the use of *X*-ray diffraction patterns of small-angle scattering for single-layer films by comparing the experimental and calculated *X*-ray patterns. Diffraction curves were obtained on DRON-2.0 diffractometer with a primary-beam graphite monochromator. For fitting the calculated curve to the experimental one, two parameters were varied independently: film thickness and roughness. The accuracy of d determination by *X*-ray diffraction method was not lower than ~ 0.5 nm. Resonator calibration for large thicknesses ($d > 100$ nm) was performed using MII-4 interferometer to an accuracy of ± 10 %. Fig. 1 exemplifies the experimental and calculated diffraction curves for a film of 26 nm in thickness and 2 nm in roughness. *X*-ray diffraction analysis of the bulk crystals and Bi_2Te_3 thin films was performed on DRON-2 setup in CuK_α-radiation in the mode $\Theta – 2\Theta$.

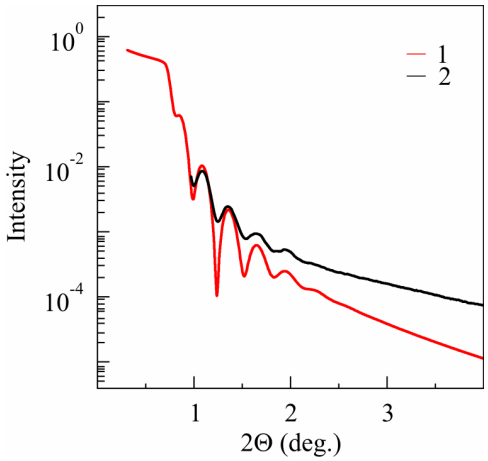

Fig. 1. Fitting of calculated curve (1) to experimental curve (2) for a film 26 nm in thickness and 2 nm in roughness.

The Hall coefficient R_H and electric conductivity σ were measured by direct current and constant magnetic field method on polycrystalline samples shaped as a parallelepiped of size $3 \times 2 \times 10$ mm and film samples shaped as a double Hall cross of size 3×1 mm. The Seebeck coefficient S was determined by compensation method with respect to copper electrodes. The error in measuring σ, R_H and S did not exceed ± 5 %. The Hall concentration $n_H(p_H)$ and mobility μ_H were determined by the formulae for one type of charge carriers: $n_H(p_H) = 1/e{\cdot}R_H$ (where e is electron charge) and νδ $\mu_H = \sigma{\cdot}R_H$. All investigations were performed at room temperature.

Discussion of results

Based on the results of other works [4-9], annealing was first performed at a temperature of $T_a \sim 570$ K, however, under conditions of oil-free vacuum this caused partial film evaporation, as testified by the absence of electrical conductivity, reduction of film thicknessи, structural imperfection, as well as considerable inhomogeneity, noticeable even during visual inspection of the film. Therefore, as the annealing temperature we selected maximum temperature ($T_a = 500$ K) causing no visible imperfections of film structure.

X-ray structural analysis of the resulting films showed an improved degree of structural perfection and grain enlargement under the influence of annealing (Fig. 2).

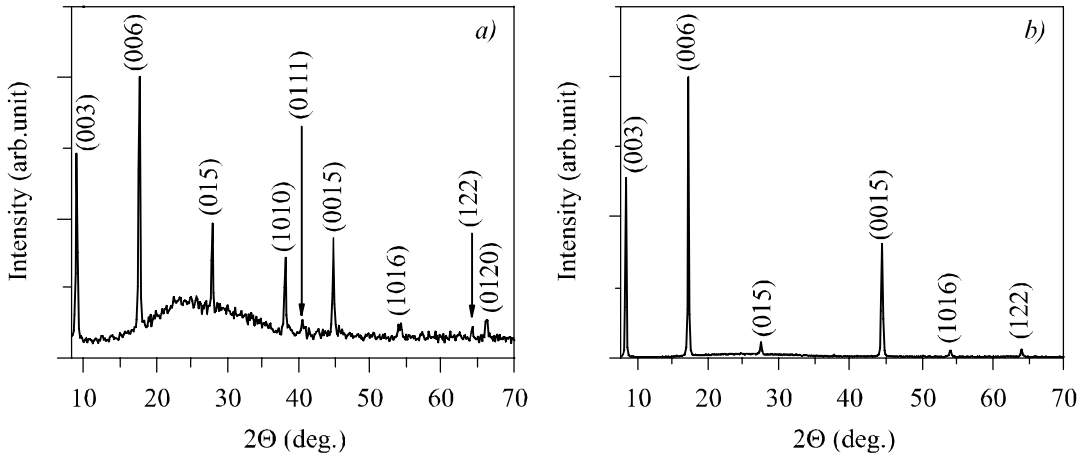

Fig. 2. X-ray diffraction patterns of Bi_2Te_3 (60 at.% Te) films prepared at $T_{sub} = 500$ K: without annealing (a) and with annealing at temperature $T_a = 500$ K within 1 hour (b).

For comparison, peak (006) was selected as the most intensive peak present on *X*-diffraction patterns of films subjected to annealing and prepared without the use of annealing. The half-width of the peak was determined by means of NewProfile 3.4 program. It was established that for films obtained from a charge of stoichiometric composition the half-width of the peak (006) on *X*-ray diffraction patterns of annealed films is ~ 40 % smaller than the half-width of a similar peak in the case of unannealed films. Moreover, on *X*-ray diffraction patterns of annealed films obtained from a charge of stoichiometric composition, considerable increase is recorded in the intensity of peaks (003), (006), (0015) corresponding to crystallographic direction (001), which can testify to formation of texture in this direction.

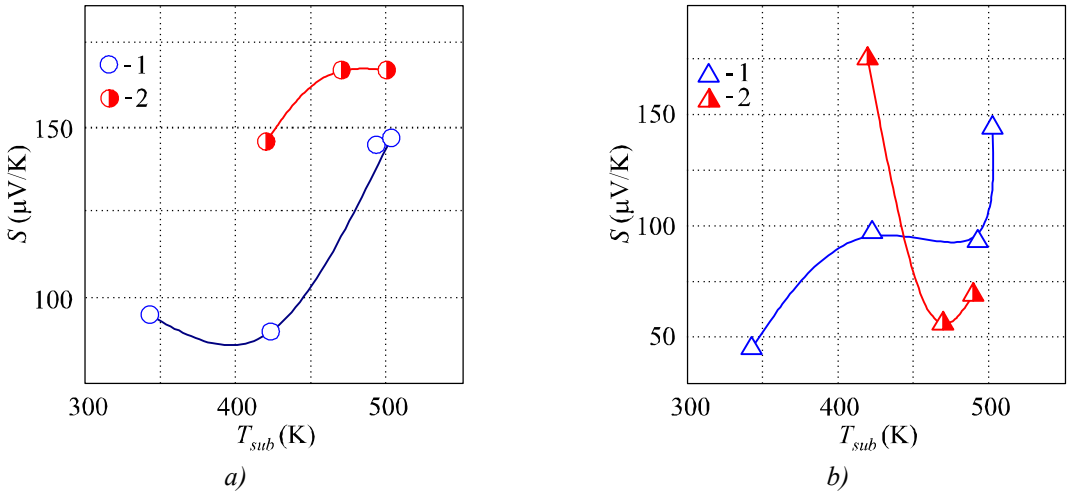

Fig. 3. The Seebeck coefficient S as a function of substrate temperature T_{sub} for films prepared from Bi_2Te_3 (60.0 at. % Te) charge (a) and films prepared from a charge with tellurium excess (62.8 at. % Te) (b): 1 – films manufactured without annealing, 2 – films manufactured with the use of annealing (T_a = 500 K within 1 hour).

To establish the effect of annealing on the basic TE properties (S, σ, μ_H and n_H (p_H)), the dependences of respective properties on substrate temperature (Figs. 3 – 7) were obtained for unannealed and annealed films. Conduction type in the unannealed and annealed films coincided with the conduction type of the initial crystals of which films were prepared: *p*-type conduction in stoichiometric crystals and *n*-type conduction in bismuth telluride crystals with tellurium excess.

Table 1

Thermoelectric parameters of unannealed and annealed films

Initial charge composition, at. % *Te*		60		62.8	
T_{sub}, K		420	500	420	490
S, μV/K	prior to annealing	90	147	–97	–93
	after annealing	146	167	–175	–69
σ, Ω^{-1} cm^{-1}	prior to annealing	456	357	272	387
	after annealing	640	603	21	363
μ_H, cm^2/V·s	prior to annealing	53	71	22	49
	after annealing	131	436	84	25
$n_H(p_H)$, 10^{19} cm^{-3}	prior to annealing	5	3	79	4
	after annealing	3	1	2	9
P, 10^{-4} W/K^2·m	prior to annealing	4	8	26	34
	after annealing	14	18	6	17

As is clear from Fig. 3 *a*, in the case of films obtained from a charge of stoichiometric composition, regardless of substrate temperature, annealing contributes to *S* increase apparently caused by p_H reduction (Fig. 6 *a*). It can be explained by improved perfection of crystal structure and increased size of grains leading to reduced concentration of antisite defects, i.e., the main reason for high charge carrier concentrations in Bi_2Te_3 films [1]. This hypothesis is confirmed by the results of *X*-ray structural analysis and is in good agreement with the observed growth of μ_H (Fig. 5 *a*).

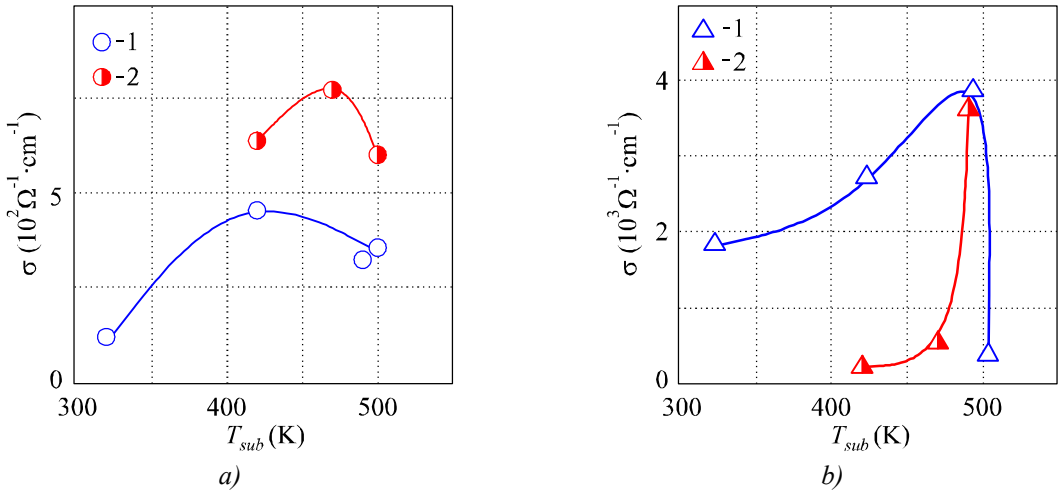

Fig. 4. Electric conductivity σ as a function of substrate temperature T_{sub} for films prepared from Bi_2Te_3 (60.0 at. % Te) charge (a) and films prepared from a charge with tellurium excess (62.8 at. % Te) (b): 1 – films manufactured without annealing, 2 – films manufactured with the use of annealing (T_a = 500K within 1 hour).

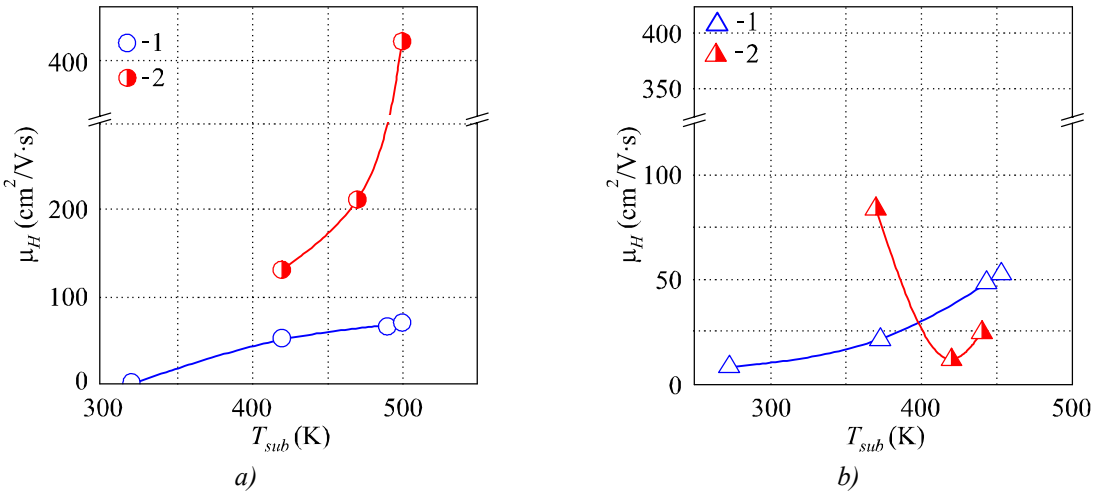

Fig. 5. Charge carrier mobility μ_H as a function of substrate temperature T_{sub} for films prepared from Bi_2Te_3 (60.0 at. % Te) charge (a) and films prepared from a charge with tellurium excess (62.8 at. % Te) (b): 1 – films manufactured without annealing, 2 – films manufactured with the use of annealing (T_a = 500 K within 1 hour).

It should be noted that positive effect of annealing on TE properties of films prepared from a charge of stoichiometric composition is observed over the entire range of substrate temperatures, but annealing produces different effect at different T_{sub}. The effect of annealing is increased with a rise in substrate temperature for all TE and galvanomagnetic properties, except for the value of *S* which at $T_{sub} > 470$ K achieves its maximum and essentially does not increase with further growth of T_{sub}. At the

same time, increase in T_{sub} above 470 K leads to further reduction of hole concentration and, despite mobility growth, leads to electric conductivity reduction. Thus, the optimal substrate temperature for films prepared from a charge of stoichiometric composition and subjected to annealing is $T_{sub} = 470$ K (Fig. 7 *a*), rather than 500 K, as in the case of films grown without annealing [10]. In so doing, TE power of annealed films is about 2.5 times higher than that of unannealed ones and is comparable to the highest values of TE power obtained in the films grown by other methods. Thus, the value of TE power obtained in this paper ($P \sim 20 \cdot 10^{-4}$ W/K^2·m) practically coincides with the P value of films obtained by magnetron sputtering method or two-source thermal evaporation method [7, 8], but is lower than for films prepared by ion-beam sputtering method ($P \sim 65 \cdot 10^{-4}$ W/K^2·m) [9].

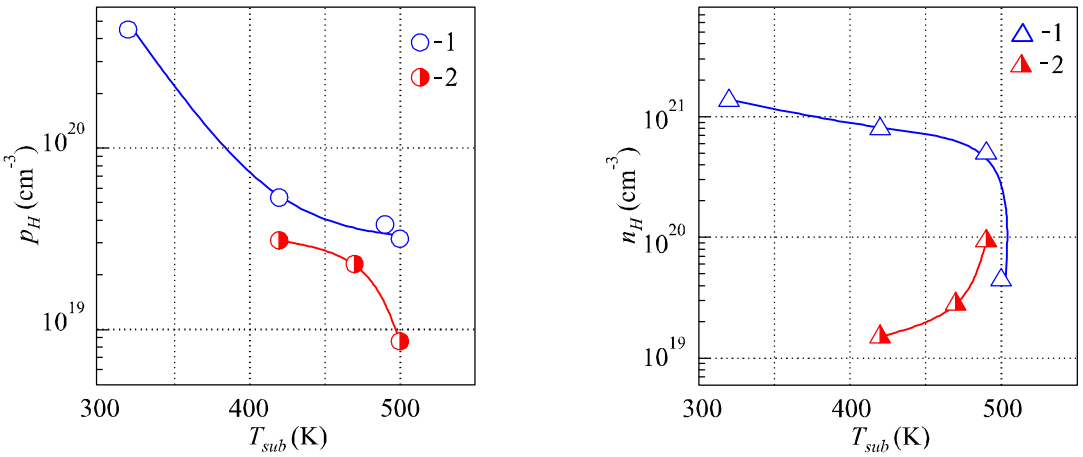

Fig. 6. Concentration of charge majority carriers $n_H(p_H)$ as a function of substrate temperature T_{sub} for films prepared from Bi_2Te_3 (60.0 at. % Te) charge (a) and films prepared from a charge with tellurium excess (62.8 at. % Te) (b): 1 – films manufactured without annealing, 2 – films manufactured with the use of annealing (T_a = 500 K within 1 hour).

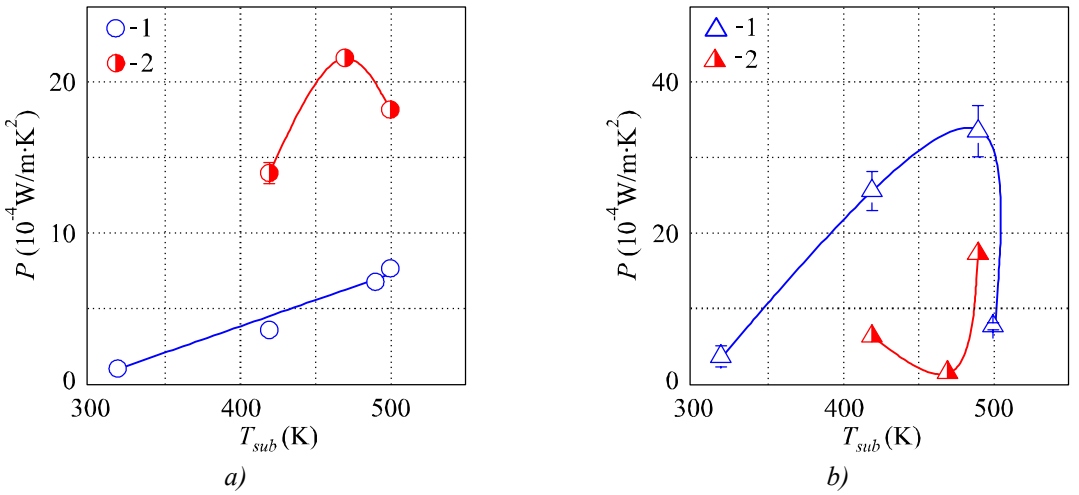

Fig. 7. Thermoelectric power P as a function of substrate temperature T_{sub} for films prepared from Bi_2Te_3 (60.0 at. % Te) charge (a) and films prepared from a charge with tellurium excess (62.8 at. % Te) (b): 1 – films manufactured without annealing, 2 – films manufactured with the use of annealing (T_a = 500 K within 1 hour).

The situation is quite different with the use of annealing the films prepared from a charge with *Te* excess. As in the case of films prepared from a charge of stoichiometric composition, annealing

leads to crystal structure perfection and reduction of crystal lattice defects concentration. This is supported by the fact of increase in electron mobility μ_H after the use of annealing (Fig. 5 *b*), testifying to reduced scattering on crystal lattice defects, as well as a decrease in n_H (Fig. 6 *b*), which, as mentioned before, is related to a reduced concentration of intrinsic defects [1]. Nevertheless, in the annealed films, *S* does not increase more than ~ 2 times, whereas σ is reduced by a factor of almost 20 (Fig. 4 *b*), which yields a considerable reduction of TE power (Fig. 7 *b*). It can be supposed that at optimal substrate temperature $T_{sub} = 490$ K the unannealed films are in the nonequilibrium state characterized by concentration inhomogeneity, high content of antisite defects and high charge carrier concentration ($n_H \sim 10^{20} - 10^{21}$ cm^{-3}) [11], and that in this state there is mainly low-energy electron scattering, which creates energy filtration of current carriers and, accordingly, preserves high values of *S*. Annealing results in relaxation processes leading not only to reduction of n_H and increase of μ_H, but also disturbing the energy filtration with a consequent reduction of *S*. Thus, it can be concluded that although annealing contributes to structural perfection of Bi_2Te_3 films prepared from a charge with *Te* excess, on the whole, TE parameters of unannealed films are higher due the nonequilibrium state. Therefore, annealing of films prepared from a charge with tellurium excess is unreasonable.

Conclusions

1. The method of one-source thermal evaporation in vacuum at different substrate temperatures ($T_{sub} = 300 - 500$ K) has been used to prepare bismuth telluride films from a charge of stoichiometric composition (60 at. % *Te*) and from a charge comprising 62.8 at. % *Te* without annealing and with the use of annealing at $T_{sub} = 500$ K within 1 hour.
2. It has been established that regardless of the initial charge composition, annealing contributes to structural perfection, increase of grain size and formation of a well-expressed texture.
3. It has been shown that for films prepared from a charge of stoichiometric composition annealing leads to increase in thermoelectric power *P*, the maximum value of which ($P = 20 \cdot 10^{-4}$ W/K^2·m) is observed at substrate temperature $T_{sub} = 470$ K and is 2.5 times larger than the maximum value of *P* in a film prepared under optimal conditions, but without the use of annealing.
4. It has been established that although annealing contributes to structural perfection of Bi_2Te_3 films prepared from a charge with *Te* excess, annealed films have lower values of TE power than unannealed ones, which is due to the nonequilibrium state in the latter.
5. The results of this work are of practical interest, since they can be used for improvement of TE parameters of Bi_2Te_3 films grown by the method of one-source thermal evaporation in vacuum.

The work was supported by the State Foundation for Basic Research of Ukraine (grant № UU 42/006 2011).

References

1. G. Goldsmid, *Application of Thermoelectricity* (Moscow: Fizmatlit, 1963), P. 320.
2. D.M. Rowe, *CRC Handbook of Thermoelectrics, CRC Press* (Boca Raton, London, New York, Washington, 1995), P. 701.
3. J.-P. Fleurial, L. Gailliard, R. Triboulet, H. Scherrer, and S. Scherrer, Thermal Properties of High Quality Single Crystals of Bismuth Telluride – Part I: Experimental Characterization, *J. Phys. Chem. Solids* **49** (10), 1237 – 1247 (1988).
4. H. Huang, W.-L. Luan, Sh.-T. Tu, Influence of Annealing on Thermoelectric Properties of Bismuth

Telluride Films Grown via Radio Frequency Magnetron Sputtering. *Thin Solid Films* **517** (13), 3731 – 3734 (2009).

5. A. Taylor, C. Mortensen, R. Roster, N. Nguyen, and D.C. Jonson, Vapor Annealing as a Post-Processing Technique to Control Carrier Concentrations of Bi_2Te_3 Thin Films, *J. Electron. Mater.* **39** (9), 1981 – 1986 (2010).
6. Z.-H. Zheng, P. Fan, G.-X. Lang, D.-P. Zhang, X.-M. Cai, and T.-B. Chen, Annealing Temperature Influence on Electrical Properties of Ion Beam Sputtered Bi_2Te_3 Thin Films. *J. Phys. Chem. Solids* **71**, 1713 – 1716 (2010)
7. S. Jeon, M. Oh, H. Jeon, S. Hyun, and H. Lee, Effects of Post-Annealing on Thermoelectric Properties of Bismuth-Tellurium Thin Films Deposited by *Co*-Sputtering. *Microelectronic Engineering* **88** (5), 541 – 544 (2011).
8. H. Zou, D.M. Rowe, and S.G.K. Williams, Peltier effect in a *Co*-Evaporated $Sb_2Te_3(P)$-$Bi_2Te_3(N)$ Thin Film Thermocouple, *J. Appl. Phys* **408**, 270 – 274 (2002).
9. Z.H. Zheng, P. Fan, T.B. Chen, Z.X. Cai, P.J. Lui, D.P. Zhang, and X.M. Cai, Optimization in Fabricating Bismuth Telluride Thin Flms by Ion Beam Sputtering Deposition, *Thin Solid Films* **520**, 5245 – 5248 (2012).
10. A.V. Budnik, E.I. Rogacheva, V.I. Pinegin, A.Yu. Sipatov, and A.G. Fedorov, Effect of Initial Bulk Material Composition on Thermoelectric Properties of Bi_2Te_3 Thin Films, *J. Electron. Mater.* (2013) doi: 10.1007/s11664-012-2439-1.
11. Z.M. Dashevsky, T.M. Yerusalimskaya, Ya.A. Kaller, et al. Manufacturing and some Properties of $Bi_2Te_{3-x}Se_x$ Solid Solution Films, Izvestia *AN SSSR: Inorganic Materials* **13** (6), 963 – 965 (1977).

Submitted 27.05.2013.

N.V. Morozova, V.V. Shchennikov

Institute of Metal Physics, Ural Division of the Russian Academy of Sciences, 18, S. Kovalevskaya Str., Yekaterinburg, 620990, GSP-170, Russia

N.V. Morozova

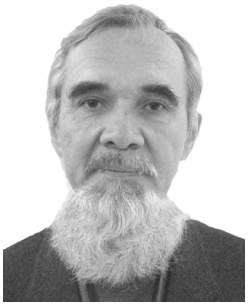

V.V. Shchennikov

THERMOELECTRIC POWER OF RARE-EARTH METAL ROW OVER A WIDE RANGE OF PRESSURES

The results of investigations of thermoelectric properties of rare-earth metals under high pressure application up to 20 GPa at room temperature are reported. This study has experimentally confirmed that a high-pressure behavior of thermoelectric power of lanthanide metals follows a general trend due to the electron s → d transfer. A distinctive behavior of thermopower of divalent europium and ytterbium has been found under pressure application. Possible influence of valence change as well as the variation of the occupancy of s-, p-, d-electronic states under pressure on the behavior of the thermoelectric power of europium and ytterbium is discussed.

Key words: thermopower, high pressure, rare-earth metals.

Introduction

Thermoelectric effect (Seebeck effect, *S*) is a very efficient tool to study the electronic structure modification of materials at the variations of temperature (*T*) [1, 2] or pressure (*P*) [3]. The *S*(*P*) data allow studying phase transitions as well as thermoelectric properties of high-pressure phases. The study of *S*(*P*) of the rare-earth metals group allows summarizing the contribution of *f*- and *d*-states to the electron structure near the Fermi level over a wide range of pressures.

The range of applications of rare-earth metals is extraordinarily wide, from the petroleum cracking catalysts and pigments for glass and ceramics to the miniature nuclear batteries, superconductors and miniature magnets. So the knowledge of their electronic properties under stress application is critically important for technologies.

Rare-earth metals include the fifteen lanthanides as well as yttrium and scandium. Under high pressure most rare-earth metals suffer a sequence of phase transformations as follows: hcp → *Sm*-type → dhcp → fcc → distorted-fcc (*d*-fcc) [4-6]. This tendency involves the majority of rare-earth metals (*Sc*, *Y*, *La*, *Pr*, *Nd*, *Pm*, *Sm*, *Gd*, *Tb*, *Dy*, *Ho*, *Er*, *Tm*, and *Lu*). While some of them (*Ce*, *Eu*, and *Yb*) demonstrate very peculiar behavior.

The purpose of the present work is the investigation of the thermoelectric power of the rare-earth metal row under high pressure up to 20 GPa. The results of investigations of thermoelectric properties of typical lanthanides (*Gd*, *Tb*, *Dy*) that follow a commonly accepted sequence of structural transformations as well as peculiar ones: lanthanum (*La*), europium (*Eu*) and ytterbium (*Yb*) are presented. The latter metals have also peculiar electronic configurations: trivalent *La* has empty *f*-band and divalent *Eu* and divalent *Yb* possess one-half filled and completely filled 4*f* electron shell, respectively.

Experimental details

The experiments were carried out on pure polycrystalline samples of the rare-earth metals. Purity of the samples was as follows: *Sc* (99.9 %), *Y* (99.9 %), *La* (99.9 %), *Ce* (99.84 %), *Pr* (99.81 %), *Nd* (99.65 %), *Sm* (99.77 %), *Eu* (99.89 %), *Gd* (99.91 %), *Tb* (99.79 %), *Dy* (99.85 %), *Ho* (99.90 %), *Er* (99.91 %), and *Yb* (99.85 %). The measurements were performed on disk-shaped samples of ~ 200 μm in the diameter and ~ 30 μm in the thickness cut from the bulk ingots. Several samples of each element were examined one by one in the same conditions for verification of data reproducibility [7].

$S(P)$ measurements were carried out using the automated setup operating with high-pressure cells with synthetic diamond anvils [3]. A sample was loaded in a container made of the lithographic stone (soft $CaCO_3$ based mineral) that served both as a gasket and a pressure-transmitting medium. The ratio of container thickness (h) to a diameter of the top of diamond anvils d = 600 μm·h/d < 0.055 provides the quasi-hydrostatic condition of pressure created [3, 8, 9]. The automated measurements permit obtaining high-quality data on pressure evolution of the thermoelectric properties. A good agreement has been obtained between the values of S at ambient pressure [2] and those measured on high-pressure setup at $P \approx 0$ GPa. The details of high-pressure experiments are described in the previous works [3, 7-9].

Results

A representative set of the data obtained is shown in Figure 1. Tables 1 and 2 summarize structural and thermoelectric data for the investigated rare-earth metals.

Table 1

Structural and thermoelectric properties of the selected rare-earth metals in the pressure range below 20 GPa

Element	Z	Electronic configuration	Ambient structure	Phase transition pressures (GPa) from Refs. [4, 10-40]					
				Sm-type	dhcp	fcc	*d*-fcc	hcp	bcc
La	57	$4f^0(5d6s)^3$	dhcp	–	–	2 – 3	5.3 – 7	–	–
Eu	63	$4f^7(5d6s)^2$	bcc	–	–	–	–	12 – 14	–
Gd	64	$4f^7(5d6s)^3$	hcp	1 – 3.5	6.5 – 10	–	–	–	–
Tb	65	$4f^9(5d6s)^3$	hcp	3 – 5	12 – 16	–	–	–	–
Dy	66	$4f^{10}(5d6s)^3$	hcp	5 – 7.5	15 – 19	–	–	–	–
Yb	70	$4f^{14}(5d6s)^2$	fcc	–	–	–	–	–	3.5 – 4.5

Gadolinium, terbium and dysprosium crystallize in hcp lattice at ambient conditions. They show the standard transformation sequence: hcp → *Sm*-type → dhcp (Table 1). For gadolinium phase transitions occur at 1 – 3.5 and 6.5 – 10 GPa, respectively [4, 10-16] (Table 1). For terbium the same phase transitions occur at higher pressures 3 – 5 and 12 – 16 GPa [4, 10-12, 17, 18] (Table 1). And in dysprosium similar transition pressures are shifted to higher magnitudes, 5 – 7.5 and 15 – 19 GPa, respectively [4, 10, 12, 19-21] (Table 1). At room temperature, *Gd* exhibits also a ferromagnetic transition near 3.5 – 5 GPa [12, 22]. Ambient thermopower values were reported to be $S \sim -(0.7 \div 2)$ μV/K,

~ –(0.9 ÷ 1.4) μV/K, and ~ –(0.55 ÷ 2) μV/K for *Gd*, *Tb* and *Dy*, respectively [2, 41] (Table 2). They agree well with our experimental data (Figs. 1, 2). Peculiarities detected on pressure dependence of thermoelectric power were referred to the above mentioned structural transitions. The Seebeck effect in gadolinium, terbium and dysprosium subjected to compression demonstrates similar behavior: monotonic rising from small negative values, –(1 ÷ 2) μV/K to magnitudes of ~ + (8 – 10) μV/K beyond ~ 5 GPa (Figs. 1, 2).

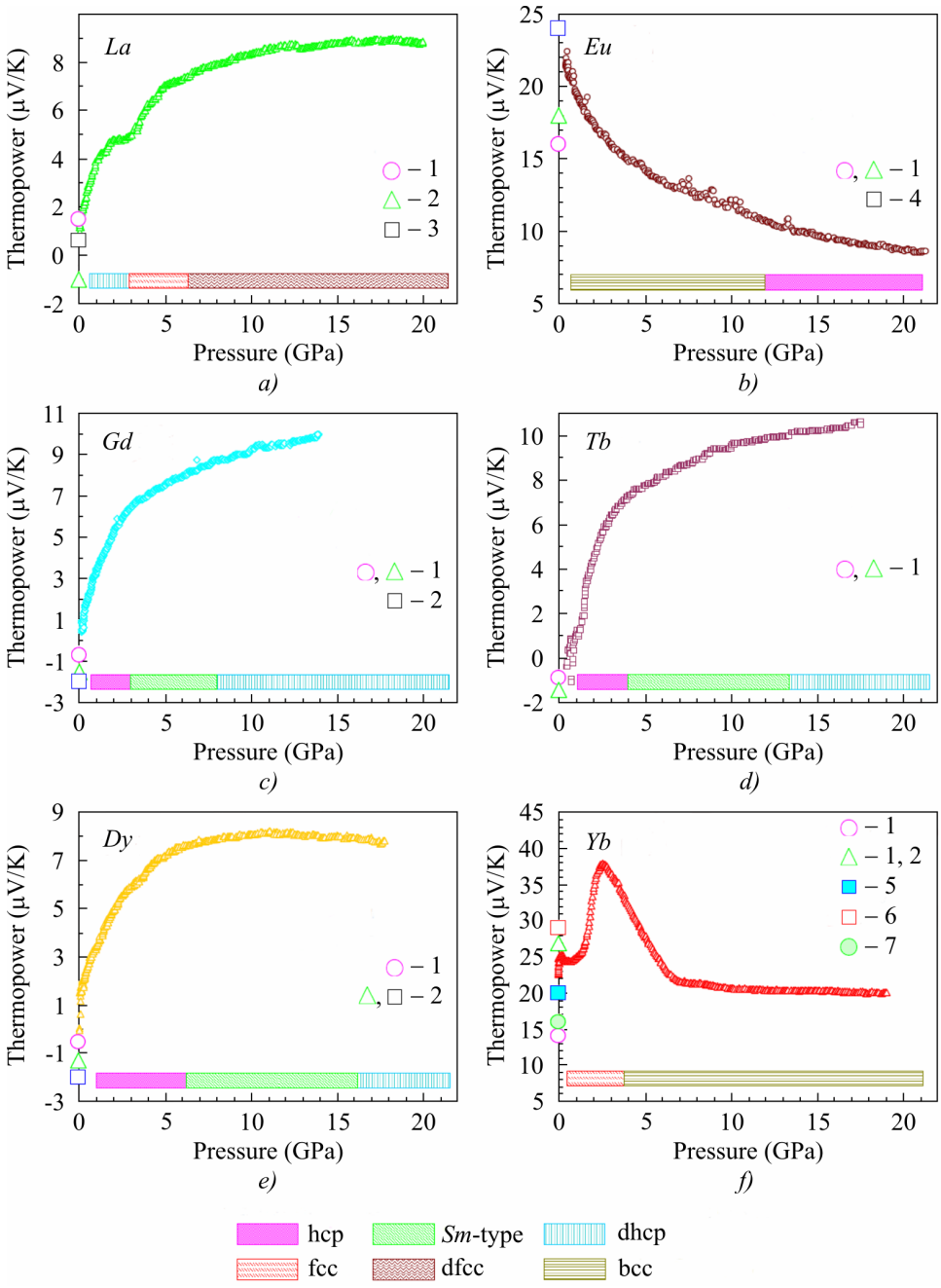

Fig. 1. Pressure dependencies of thermoelectric power of the selected lanthanides: (a) lanthanum, (b) europium, (c) gadolinium, (d) terbium, (e) dysprosium and (f) ytterbium. The dashed rectangles schematically show the stability regions of different phases, summarized in Table 1. The points 1 – 7 at ambient pressure label data taken from the literature: 1 – [2], 2 – [41], 3 – [42], 4 – [43], 5 – [39], 6 – [44], and 7 – [40]. Data for Gd, Tb and Dy have been taken from [7].

Table 2

Thermoelectric properties of the selected rare-earth metals in the range of pressures below 20 GPa

Element	Thermoelectric power (μV/K)	
	Ambient	at 16 – 20 GPa
La	+1.5[a], –1[b], +0.6[c]	+8.9
Eu	+16[a],+18[a], +24[d]	+8.5
Gd	–0.7[a], –1.5[a], –2[b]	+(9.5 ÷ 10)
Tb	–0.9[a], –1.4[a], –1.2[b]	+(10 ÷ 10.5)
Dy	–0.55[a], –1.3[b], –2[b]	+8
Yb	+14[a], +27[a, b], +20[e], +29[f], +16[g]	+20

[a] – [2], [b] – [41], [c] – [42], [d] – [43], [e] – [39], [f] – [44], [g] – [40]

Lanthanum has $4f^0(5d6s)^3$ electronic configuration and at ambient conditions it crystallizes in a dhcp lattice (space group $P6_3/mmc$). It shows a phase transformation path: dhcp → fcc → distorted-fcc at 2 – 3 GPa and 5.3 – 7 GPa, respectively [4, 10, 23-26]. Ambient thermopower values determined in our experiments $S \cong (-1 \div +1.7)$ μV/K (Figs. 1(*a*) and 2) agree well with the literary data [2, 41, 42]. Pressure behavior of thermopower in *La* resembles those of most of the lanthanides [7], *Sc* and *Y* [45]. But on $S(P)$ dependence for *La* one can see a pronounced kink near 3 GPa related probably to the dhcp → fcc transition [4, 10, 23-26]. A smooth bend in the thermopower curve near 5.5 – 6 GPa (Fig. 1 (*a*)) could be due to the structural transition into the distorted-fcc phase [4, 10, 23-26].

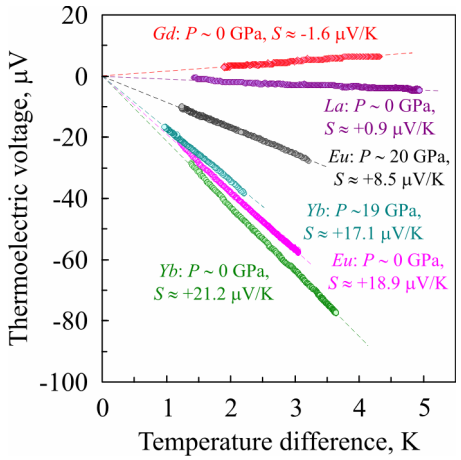

Fig. 2. Examples of dependences of thermoelectric signal U on applied temperature difference ΔT between sample edges. The values of thermopower S correspond to a linear coefficient between thermoelectric voltage (U) and temperature difference (ΔT) as follows: $S = -U/\Delta T$.

Europium is a divalent metal having an electron configuration of $4f^7(5d6s)^2$ and at ambient conditions, it adopts a body-centered cubic (bcc) lattice (space group $Im\bar{3}m$). At pressure of 12 – 14.5 GPa at room temperature, *Eu* transforms to hcp phase [4, 10, 27-32]. Previous studies have reported *Eu* to transform from the hcp structure to a new phase, *Eu*-III, at 18 GPa [4, 10, 30, 32]. However, recent *X*-ray diffraction investigations show a sluggish transition above 18 GPa to a mixture

of hcp and a monoclinic phase with space group *C*2/*c* [29]. In [28, 30] it is illustrated that this *Eu*-III phase consists of hcp-*Eu* plus a rhombohedral phase (perhaps a hydride EuH_x), the atomic volume of which suggests that it is an impurity [28, 30]. At ambient pressure the thermopower values of *Eu* were found to be within a range of $S \sim (+17, +23)$ μV/K (Figs. 1 (*b*) and 2) close to previously reported values [2, 43]. The Seebeck effect decreases with pressure and reaches $S \sim +(8 \div 9)$ μV/K near 22 GPa (Figs. 1 (*b*) and 2). The pressure dependence of thermopower for this element (Fig. 1 *b*) is completely opposite to similar dependences for the majority of lanthanides [7].

Ytterbium is a divalent semimetal having an electron configuration of $4f^{14}(5d6s)^2$. At room and elevated temperatures, *Yb* has a fcc lattice (β-phase) of the $Fm\bar{3}m$ space group [10, 46-47]. With pressure application, it suffers fcc → bcc phase transition at 3.5 – 4.5 GPa [4, 10, 33-40]. Near 2 GPa, *Yb* shows a semimetal-semiconductor electronic transition [39, 48-52]. A huge peak on the thermopower curve near 2.6 GPa (Fig. 1 (*f*)) is probably due to this electronic transition [39, 48-52]. With transition to the bcc lattice, *Yb* is reported to be metallized under pressure [10, 35, 36]. Ambient thermopower values were found to be $S \sim +(20 \div 25)$ μV/K (Figs. 1 (*f*) and 2), that is close to previously reported values [2, 39-41, 44].

Discussion

Similar thermopower behavior under pressure of lanthanides that follows a commonly accepted sequence of structural transformations [4] was observed in previous investigation [7]. For *Sc*, *Y* and *La* as well as for most of the lanthanides [7] the pressure applied tends to rising of the Seebeck effect to relatively high positive values of $S \sim 10$ μV/K beyond ~ 3 – 10 GPa (not shown at Fig. 1). Divalent elements *Eu* and *Yb* do not follow a commonly observed sequence of structural transformations for lanthanides and also demonstrate pressure evolution of thermoelectric properties (Fig. 1) distinguishing from the above mentioned trend. Both metals have much higher initial values of $S \sim +25$ μV/K which are strongly decreased under pressure in the bcc crystal structure (for *Yb* above ~ 3 GPa).

Under high pressure, a population of *s*-electrons in general decreases and that of *d*-electrons increases due to $s \rightarrow d$ electron transfer [4-6]. For a description of the thermopower behavior the expression ought to be used that takes contributions of both *s*- and *d*-bands into consideration [53]

$$S_d^s = -\frac{\pi^2 k^2 T}{3|e|}\left(\frac{3}{2\varepsilon} - \frac{1}{N_d(\varepsilon)}\frac{dN_d(\varepsilon)}{d\varepsilon}\right)_{\varepsilon=\varepsilon_F}, \quad (1)$$

where S_d^s is the diffusion thermoelectric power, k is the Boltzmann constant, T is the absolute temperature, e is the electron charge, ε is the electron energy, N_d is the density of states in the *d*-band and ε_F is the Fermi energy. Due to high concentrations of charge carriers in metals, the first term in Eq. 1 usually gives contributions to thermopower values of about ~ 1 μV/K. Thus, the higher thermopower values can not be explained by the first term and therefore they could come out from the second one. Similar behavior of thermoelectric properties of *Gd*, *Tb*, *Dy* and *La* under compression indeed can originate from pressure-enhanced scattering of the *s*-electrons by the carriers of *d*-band (the second term in Eq. 1). Most of lanthanides (except for *Ce*, *Eu* and *Yb*) demonstrate behavior of thermopower under pressure similar to *La* [7]. The contribution of the *f*-band to the values of *S* in view of similarity of *S*(*P*) dependences for these rare-earth metals row seems to be not very essential [53].

The second term in Eq. 1 gives a positive contribution to *S* for almost empty *d*-band [53] that agrees well with our experiments (Figs. 1, 2)

The anomalous behavior of *Eu* and *Yb* thermopower under pressure may be due to several reasons. First, it may be partial delocalization of *f*-electrons and the corresponding increase of valence from 2 to 3. The second reason may be the variation of occupancy of *s*-, *p*-, *d*-electronic bands, and in particular the filling of almost empty *d*-bands. Peculiar electronic properties of *Yb* under pressure are believed to be determined by partial delocalization of the *f*-electrons [4-6, 14]. At higher pressures the narrow *f*-bands overlap and their interatomic interactions increase, finally leading to *f*-delocalization [14]. The fcc to bcc transition at *Yb* was proposed to occur when the 4*f* electrons start to delocalize varying the valence of *Yb* from 2+ to 3+ [39].

Experimental investigation of *X*-ray absorption near-edge spectroscopy (XANES) at Eu's L_3 edge to pressures as high as 34 GPa [54], the ^{151}Eu Mössbauer spectroscopy studies to 14 GPa at 44 K [55] and synchrotron Mössbauer experiment at ambient temperature [56] have shown that the valence of *Eu* increases sharply under pressure, reaching the valence of ~ 2.5 at 10 – 12 GPa. A more recent XANES, *X*-ray magnetic circular dichroism, and synchrotron Mössbauer spectroscopy experiments have shown *Eu* metal to remain nearly divalent to the highest pressures reached (87 GPa) with magnetic order persisting to at least 50 GPa [57]. An analysis based on ab initio calculations indicates that the pressure-induced changes in XANES spectra in the 10 – 20 GPa range, which were previously interpreted as indicative of a marked change in *Eu* valence, result from significant changes in the electronic and crystal structure at the bcc → hcp structural phase transition. However, this increase may originate from pressure-induced changes in the properties of the *s*-, *p*-, and *d*-electrons, and so is not related to a significant change in 4*f*-electron occupation. Thus, *Eu* metal probably remains divalent or nearly divalent to 87 GPa [57]. Using the second approach of change in the occupancy of electronic *s*-, *p*-, *d*-states, the strong decrease of *S* in *Eu* with a rise in pressure is attributable to considerable increase of *s*-electron states density (and hence the electron concentration) or to filling of empty *d*-band; with certain occupancy of *d*-band the second term in Eq.1 is reduced indeed [53].

Conclusions

The measurements of thermoelectric power of rare-earth metals over a wide range of pressures have revealed the similarity of *S*(*P*) behavior for most members of the row (except for *Ce*, *Eu* and *Yb*) corresponding to similarity of the sequence of structural transformations under pressure of these metals. For divalent *Yb* and *Eu* the inverse pressure dependence of *S* (decrease) in bcc phase as compared to the rest of rare-earth metals can be attributed to several possible reasons: the partial delocalization of *f*-states (most probably it occurs at *Yb*) [4-6, 14, 39] and the variation of occupancy of *s*-, *p*-, *d*-electron bands [57]. The second term in Eq. 1 indeed has a sharp maximum at certain position of the Fermi level [53] that may tend to decrease in *S* with a rise in pressure. The second approach also allows explaining the high values of $S \sim +25$ μV/K for *Yb* and *Eu* as compared to the rest of rare-earth metals.

The work was done within RAS Program (Project no. 01.2.006 13394), by UD RAS as part of Program ''Matter at high energy densities'' of the Presidium of RAS (project 12-P-2-1004), by the Ministry of Education and Science of the Russian Federation (Contract 14.518.11.7020), and by the Oriented Basic Research Project of the Ural Branch of the Russian Academy of Sciences.

References

1. M.V. Vedernikov, The Thermoelectric Powers of Transition Metals at High Temperature, *Advances in Physics* **18** (74), 337 – 370 (1969).
2. I.V. Vedernikov, A.T. Burkov, V.G. Dvinitkin, and N.I. Moreva, The Thermoelectric Power, Electrical Resistivity and Hall Constant of Rare Earth Temperature Range 80-1000 K, *Journal of the Less-Common Metals* **52**, 221 – 245 (1977).
3. V.V. Shchennikov, S.V. Ovsyannikov, and A.Y. Manakov, Measurement of Seebeck Effect (Thermoelectric Power) at High Pressure up to 40 GPa, *J. Phys. Chem. Solids* **71** (8), 1168 – 1174 (2010).
4. W.B. Holzapel, Physics of Solids under Strong Compression, *Rep. Prog. Phys*. **59**, 29 – 90 (1996).
5. B. Johansson, A. Rosengren, Generalized Phase Diagram for the Rare-Earth Elements: Calculations and Correlations of Bulk Properties, *Phys. Rev. B* **11** (3), 2836 – 2857 (1975).
6. J.C. Duthie, D.G. Pettifor, Correlation between *d*-Band Occupancy and Crystal Structure in the Rare Earths *Phys. Rev. Lett*. **38** (10), 564 – 567 (1977).
7. V.V. Shchennikov, N.V. Morozova, and S.V. Ovsyannikov, Similar Behavior of Thermoelectric Properties of Lanthanides under Strong Compression up to 20 GPa, *J. Appl. Phys*. **111**, 112624 (2012).
8. S.V. Ovsyannikov, V.V. Shchennikov, A. Misiuk, and I.A. Komarovsky, Electronic Properties and Phase Transitions in *Si*, *ZnSe*, and *GaAs* under Pressure Cycling up to 20 – 30 GPa in a High-Pressure Cell, *Physica Status Solidi B* **246** (3), 604 – 611 (2009).
9. S.V. Ovsyannikov, V.V. Shchennikov, High-Pressure Routes in the Thermoelectricity or How One Can Improve a Performance of Thermoelectrics, *Chem. Mater*. **22**, 635 – 647 (2010).
10. E.Yu. Tonkov, E.G. Ponyatovsky, *Phase Transformations of Elements under High Pressure* (Washington, CRC Press, 2004), 377 p.
11. M. Mito, K. Matsumoto, Y. Komorida, H. Deguchi, S. Takagi, T. Tajiri, T. Iwamoto, T. Kawae, M. Tokita, and K. Takeda, Volume Shrinkage Dependence of Ferromagnetic Moment in Lanthanide Ferromagnets Gadolinium, Terbium, Dysprosium, and Holmium, *J. Phys. Chem. Solids* **70**, 1290 – 1296 (2009).
12. D.B. McWhan, A.L. Stevens, Effect of Pressure on the Magnetic Properties and Crystal Structure of *Gd*, *Tb*, *Dy*, and Ho, *Phys. Rev.* **139**, A682 – A689 (1965).
13. A. Nakaue, Studies in the Pressure-Temperature Phase Diagram of *Nd*, *Sm*, *Gd* and *Dy*, *J. Less-Common Met*. **60**, 47 – 58 (1978).
14. H. Olijnyk, Lattice Vibrations and Electronic Transitions in the Rare-Earth Metals: Yttrium, Gadolinium and Lutetium, *J. Phys.: Condens. Matter* **17**, 43 – 52 (2005).
15. J. Akella, G.S. Smith, and A.P. Jephcoat, High-Pressure Phase Transition Studies in Gadolinium to 106 GPa, *J. Phys. Chem. Solids* **49**, 573 – 576 (1988).
16. W.A. Grosshans, W.B. Holzapfel, Atomic Volumes of Rare-Earth Metals under Pressures to 40 GPa and above, *Phys. Rev. B* **45** (10), 5171 – 5178 (1992).
17. N.C. Cunningham, W. Qiu, K.M. Hope, H.-P. Liermann, and Y.K. Vohra, Symmetry Lowering under High Pressure: Structural Evidence for *f*-Shell Delocalization in Heavy Rare Earth Metal Terbium, *Phys. Rev. B* **76**, 212101 (2007).
18. J.S. Olsen, S. Steenstrup, and L. Gerward, High Pressure Phases of Terbium: Possibility of a thcp Phase, *Phys. Lett. A* **109,** 235 – 237 (1985).
19. J.C. Jamieson, *X*-ray Diffraction Studies on Dysprosium at High Pressures, *Science* **145**, 572 – 574 (1964).

20. Y.R. Shen, R.S. Kumar, A.L. Cornelius, and M.F. Nicol, High-Pressure Structural Studies of Dysprosium using Angle-Dispersive *X*-ray Diffraction, *Phys. Rev. B* **75**, 064109 (2007).
21. J.R. Patterson, C.K. Saw, and J. Akella, Static High-Pressure Structural Studies on *Dy* to 119 GPa, *J. Appl. Phys.* **95**, 5443 – 5446 (2004).
22. N. Tateiwa, A. Nakagawa, T. Iwamoto, T. Kawae, M. Hidaka, K. Takeda, and M. Mito, Electrical Resistance Measurement on a Ferromagnetic Element Gadolinium under High Pressure, *J. Magn. Magn. Mater.* 272-276, 34 – 35 (2004).
23. F. Porsch, W.B. Holzapfel, Novel Reentrant High Pressure Phase Transition in Lanthanum, *Phys. Rev. Lett*. **70** (26), 4087 – 4089 (1993).
24. H. Bohn, A. Eichler, Specific Heat of d-hcp and fcc Lanthanum under High Pressure, *Z. Phys. B – Condensed Matter* **83**, 105 – 111 (1991).
25. G.Y. Gao, Y.L. Niu, T. Cui, L.J. Zhang, Y. Li, Y. Xie, Z. He, Y.M. Ma, and G.T. Zou, Superconductivity and Lattice Instability in Face-Centered Cubic Lanthanum under High Pressure, *J. Phys.: Condens. Matter* **19**, 425234 (2007).
26. V.A. Goncharova, G.G. Il'ina, Anomalies in the Elastic Properties of Polycrystalline Lanthanum at Phase Transitions under Pressure, *Zh. Eksp. Teor. Fiz*. **86**, 1708 – 1714 (1984).
27. R.J. Husband, I. Loa, G.W. Stinton, S.R. Evans, G.J. Ackland, and M.I. McMahon, Europium-IV: An Incommensurately Modulated Crystal Structure in the Lanthanides, *Phys. Rev. Lett*. **109**, 095503 (2012).
28. R.J. Husband, I. Loa, G.W. Stinton, S.R. Evans, G.J. Ackland, and M.I. McMahon, The Structure of *Eu*-III, *J. Phys.: Conf. Ser*. **377**, 012030 (2012).
29. W. Bi, Y. Meng, R.S. Kumar, A.L. Cornelius, W.W. Tipton, R.G. Hennig, Y. Zhang, C. Chen, and J.S. Schilling, Pressure-Induced Structural Transitions in Europium to 92 GPa, *Phys. Rev. B* **83**, 104 – 106 (2011).
30. R.J. Husband, I. Loa, G.W. Stinton, G.J. Ackland, and M.I. McMahon, Phase Transitions in Europium at High Pressures, *High Pressure Research* **33**(1), 158 – 164 (2013).
31. W.A. Grosshans, W.B. Holzapfel, *X*-ray Studies on Europium and Ytterbium up to 40 GPa, *J. Magn. Magn .Mater.* 47&48, 295 – 296 (1985).
32. K. Takemura, K. Syassen, Pressure-Volume Relations and Polymorphism of Europium and Ytterbium to 30 GPa, *J. Phys. F: Met. Phys*. **15**, 543 – 559 (1985).
33. W.H. Gust, E.B. Royce, New Electronic Interactions in Rare-Earth Metals at High Pressure, *Phys. Rev. B* **8** (8), 3595 (1973).
34. B.I. Min, H.J.F. Jansen, T. Oguchi, A.J. Freeman, Electronic and Structural Properties of Rare Earth Metals at Normal and High Pressures: *Eu* and *Yb*, *J. Magn. Magn. Mater.* **59**, 277 – 286 (1986).
35. R.H. Mutlu, Calculated High-Pressure-Induced Electronic and Structural Phase Transitions in *Sr* and *Yb* up to 50 kbar, *Phys. Rev. B* **54**, 16321 – 16324 (1996).
36. D.B. McWhan, T.M. Rice, and P.H. Schmidt, Metal-Semiconductor Transition in Ytterbium and Strontium at High Pressure, *Phys. Rev*. **177**, 1063 – 1071 (1969).
37. G.N. Chesnut, Y.K. Vohra, Structural and Electronic Transitions in Ytterbium Metal to 202 GPa, *Phys. Rev. Lett*. **82**, 1712 – 1715 (1999).
38. Y.C. Zhao, F. Porsch, and W.B. Holzapfel, Irregularities of Ytterbium under High Pressure, *Phys. Rev. B* **49**, 815-817 (1994).
39. N.V.C. Shekar, J.F. Meng, D.A. Polvani, and J.V. Badding, Thermoelectric Power of Nickel and Ytterbium at High Pressure: a Comparative Study, *Solid State Communications* **116,** 443 – 445 (2000).

40. A.O. Saburov, N.N. Stepanov, A.P. Shvetsov, Thermoelectric Power of *Yb* under Hydrostatic Pressures up to 11 GPa, *Solid State Physics* **32** (8), 2497 – 2500 (1990).
41. H.J. Born, S. Legvold, F.H. Spedding, Low-Temperature Thermoelectric Power of the Rare-Earth Metals, *J. Appl. Phys*. **32**, 2543 – 2549 (1961).
42. V. Vijakumar, Investigation of Pressure Induced Electronic Transitions in Lanthanam, Uranium and Thorium, *Journal of Physics and Chemistry of Solids* **46** (1), 17 – 20 (1985).
43. G.T. Meaden, N.H. Sze, Thermoelectric Power of Annealed and Strained Europium Metal Between 10 and 300°K, *Journal of Low Temperature Physic*s **1** (6), 568 – 576 (1969).
44. M.A. Angadi, P.V. Ashrit, Thermoelectric Effect in Ytterbium and Samarium Films, *J. Phys. D: Appl. Phys*. **14**, L125-8 (1981).
45. V.V. Shchennikov, N.V. Morozova, and S.V. Ovsyannikov, Thermoelectric Properties of Rare-Earth Elements at High Pressures, *Program and Book of Abstracts of of 50th European High Pressure Research Group Meeting* (Thessaloniki, Greece, 2012), p. 157.
46. E. Bucher, P.H. Schmidt, A. Jayaraman, K. Andres, J.P. Maita, K. Nassau, and P.D. Dernier, New First-Order Phase Transition in High-Purity Ytterbium Metal, *Phys. Rev. B* **2**(10), 3911 – 3917 (1970).
47. H.T. Hall, J.D. Barnett, L. Merril, Ytterbium: Transition at High Pressure from Face-Centered Cubic to Body-Centered Cubic Structure, Reprinted from *Science* **139** (3550), 111 – 112 (1963).
48. L. Spendeler, D. Jaccard, and J. Sierro, High Pressure Transport Properties of Pure Ytterbium in the Metallic bcc Phase, *Physics Letters A* **177**, 375 – 378 (1993).
49. T.G. Ramesh, V. Shubha, S. Ramaseshan, Phase Transitions in Ytterbium under Pressure, *J. Phys. F: Metal Phys.* **7** (6), 981 – 990 (1977).
50. H. Katzman, J.A. Mydosh, High-Pressure Resistance-Temperature Behavior of bcc-Ytterbium, *Z. Physik* **256**, 380 – 386 (1972).
51. C.M. Hurd, J.E.A. Alderson, Another Indicated Phase Transformation in Ytterbium, *Solid State Communications* **12**, 375 – 377 (1973).
52. B.J. Beaudry, K.A. Gschneidner Jr., Concerning another Indicated Phase Transition in Ytterbium, *Solid State Communications* **15**, 791 – 793 (1974).
53. F.J. Blatt, P.A. Schroeder, C.L. Foiles, and D. Greig, *Thermoelectric Power of Metals* (New York Plenum, 1979), 264 p.
54. J. Röhler, The Valence of *Eu* under High Pressure, *Physica* **144B**, 27 – 31 (1986).
55. R.D. Taylor, J.N. Farrell, Mössbauer Effect of Europium Metal under Pressure, *J. Appl. Phys*. **61**, 3669 (1987).
56. G. Wortmanna, U. Ponkratza, B. Bielemeiera, and K. Rupprecht, Phonon Density-of-States in bcc and hcp *Eu* Metal under High Pressure Measured by 151 *Eu* Nuclear Inelastic Scattering of Synchrotron Radiation, *High Pressure Research* **28** (4), 545 – 551 (2008).
57. W. Bi, N.M. Souza-Neto, D. Haske, G. Fabbris, E.E. Alp, J. Zhao, R.G. Hennig, M.M. Abd-Elmeguid, Y. Meng, R.W. McCallum, K. Dennis, J.S. Schilling, Synchrotron *X*-ray Spectroscopy Studies of Valence and Magnetic State in Europium Metal to Extreme Pressures, *Physical Review B* **85**, 205134 (2012).

Submitted 16.05.2013.

M. Culebras, C.M. Gomez, A. Cantarero

Materials Science Institute, University of Valencia,
Valencia, 46071, Spain

THERMOELECTRIC MATERIALS BASED ON POLY (3, 4-ETHYLENDIOXYTHIOPHENE)

Poly (3, 4-ethylenedioxythiophene) with several counterions was investigated for thermoelectric applications. Polystyrene sulfonate, tosylate, and perchlorate were used as counterions. Thermal, optical and thermoelectric characterization have been made on poly (3, 4-ethylenedioxythiophene) based polymers. Very high conductive poly (3, 4-ethylenedioxythiophene):ClO_4, was synthesized by electrochemical deposition. Its high conductivity (750 S/cm) indicates that this polymer can be the starting point for new high performance thermoelectric materials.
Key words: conducting polymers, energy, organic semiconductors, thermoelectric.

Introduction

During the last decade many investigations have been focused on the development of energy recovery devices, due to high energy demand in today's society. Therefore, it is important to use the energy losses, such as heat, and produce energy. Thermoelectric materials have recently attracted attention for its potential as power generation [1], cooling [2] and thermal detection [3], so thermoelectric materials can convert waste energy into electricity. Efficient thermoelectric materials are of great interest in industrial, automotive and aerospace applications. The efficiency of a thermoelectric material is measured by a factor known as figure of merit, *ZT*:

$$ZT = \frac{S^2 T \sigma}{\kappa} \tag{1}$$

where σ is the electrical conductivity, *S* the Seebeck coefficient and κ the thermal conductivity. According to equation (1), the maximum efficiency will be attained when the material has high electrical conductivity and low thermal conductivity. If the thermal conductivity is similar in different samples, the power factor *PF* ($PF = \sigma S^2$) is often used to compare the relative efficiency. The maximum efficiency of a thermoelectric material is achieved for a given temperature range, so that a thermoelectric material could be very efficient for low temperatures, however, if the material is subjected to high temperatures, the efficiency can decrease significantly, and vice versa. Traditionally, inorganic materials, such as *PbTe* [4, 5] and Bi_2Te_3 [6, 7, 8], have been used for thermoelectric applications. These inorganic compounds have several drawbacks, such as high cost of production, toxicity and scarcity of materials. For this reason, many efforts have been devoted to the search for new efficient thermoelectric materials during the last years.

Organic conducting polymers, such as polyaniline (PANI) [9], polythiophene (PTH) [10], poly (3, 4-ethylenedioxythiophene): poly (styrenesulfonate) (PEDOT:PSS) [11] and polycarbazoles (PC) [12] have a great potential for thermoelectric applications. These organic materials offer more advantages than inorganic compounds when used for thermoelectric applications, such as chemical

modification easier manipulation, abundance, low cost of raw materials, low thermal conductivity (0.2 W/mK for PEDOT:PSS) and good mechanical properties. But, on the contrary, the global thermoelectric efficiency is reduced. The polyanion, PSS, can be replaced by small anions, such as tosylate or perchlorate to increase the conductivity by preventing the excess of insulating phase.

In this work, we use as base polymer PEDOT with several counter ions, that is, polystyrene sulfonate (PSS), tosylate (Tos), and perchlorate (ClO_4). Chemical and physical properties, as solubility and electrical conductivity, are strongly dependent on the counterion employed. The objective of this work is to compare thermoelectric properties of the three polymers, PEDOT:PSS, PEDOT: Tos and PEDOT: ClO_4, as a function of the counterion used.

1. Experimental

1.1. Materials

PEDOT:PSS solution (1.3 wt.% in water) with a ratio of PEDOT to PSS of 38.5 to 61.5 %, ethylenedioxythiophene 97 % (EDOT), iron (III) *P*-toluensulfonate hexahydrate, lithium perchlorate 99 %, nitric acid (HNO_3) and hydrochloric acid (HCl) were purchased from Sigma-Aldrich Co. acetonitrile, butanoland tetrahydrofurane were obtained from Fisher Scientific.

1.2. Preparation of PEDOT:PSS

The commercial solution of PEDOT:PSS was precipitated in tetrahydrofurane. The suspension was filtered and dried at 100 °C in vacuum for 5 h. Finally, the powder obtained was used to make a thin pellet (100 μm thickness).

1.3. Preparation of PEDOT:Tos

Iron tosylate, FeTos, was added to the EDOT (1 wt.%) solution in butanol (molar ratio 1:1.5). The solution was deposited on a glass substrate at 100 °C. The polymer obtained was washed several times with water and ethanol, then it was filtered and dried at 100 °C in vacuum for 5 h. Finally, the powder obtained was used to make a thin pellet (100 μm thickness).

1.4. Preparation of PEDOT:ClO_4

The preparation of PEDOT:ClO_4 films was performed in a three electrode cell [13, 14] from a solution formed by 0.1 M of $LiClO_4$ in acetonitrile (ACN) with EDOT monomer (10^{-2} M). Gold coated glass as a working electrode, platinum grid as a counter electrode and an $Ag/AgCl$ as reference electrode were used into the cell. A Keithley 2400 was used as a potentiostat. After the necessary connections were made, a current of –3 mA was applied to the electrolytic cell and the desired amounts of PEDOT were coated onto the working electrode. PEDOT coated gold glass was washed with ACN to remove the monomer and oligomeric species from the surface. Then the gold layer was removed using acid solution (HNO_3:HCl ratio 1:3) and finally the film (110 – 120 nm) was washed several times with water.

1.5. Characterization

The van der Pauw method has been used to determine the electrical conductivity [15] of the samples. The electrical conductivity is obtained from two four-point resistance measurements. For the first resistance measurement a current I_{AC} is driven from two contacts, named A and C, and the potential difference V_{BD} between the other two contacts, B and D, is measured, giving $R_1 = V_{BD}/I_{AC}$.

The second resistance, $R_2 = V_{AB}/I_{CD}$, is obtained by driving a current from C to D and measuring the voltage between A and B. A Keithley 2400 current source was used as driving source and voltmeter. The conductivity of the sample can be obtained by solving the van der Pauw equation:

$$e^{-\pi d R_1 \sigma} + e^{-\pi d R_2 \sigma} = 1 \tag{2}$$

where d is the sample thickness.

A home-made setup has been used to measure the Seebeck coefficient. Temperature differences are generated between two points of the sample and the associated potential difference has been measured. A Lakeshore 336 temperature controller has been employed to control the temperature and a Keithley 2750 Multimeter/Switch System to record the potential difference. The Seebeck coefficient is determined as the ratio between the electrical potential, ΔV, and the temperature difference, ΔT:

$$S = \frac{\Delta V}{\Delta T} \tag{3}$$

The linearity of the $\Delta V/\Delta T$ ratio has been checked.

The Raman spectroscopy analysis was carried out in a Jobin Yvon T64000 spectrophotometer with macro and micro input. The excitation source was a laser Spectrum 70 capable of producing several lasers lines through the visible range. The excitation wavelength was 514.16 nm, the signal was recorded in a range of 1200 cm^{-1} to 1800 cm^{-1} with acquisition time of 100 seconds. Two scans were performed in order to eliminate peaks originated from cosmic rays.

Differential scanning calorimetry (DSC) was performed on a TA instruments DSC Q-20 calibrated with indium and sapphire. The samples were subjected to two scans in the range of –90 to 220 °C at a heating rate of 20 °C/min.

2. Results and discussion

Typical polyanion such as polystyrene sulphonic acid, PSS, of PEDOT has been replaced by small anions such as tosylate and perchlorate to study changes on thermoelectric properties. PSS is a polymeric anion, Tos is an organic anion and perchlorate is an inorganic anion. Figure 1 shows the molecular structures of PEDOT, PSS, Tos and perchlorate.

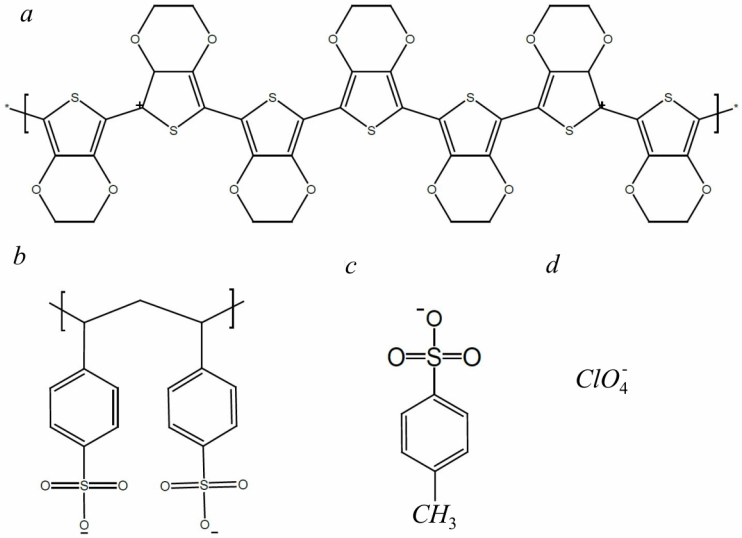

Fig. 1. Molecular structures of: a) PEDOT, b) PSS, c) Tos and d) perchlorate.

In order to characterize the thermal properties, DSC was used. It is important to know how these materials behave under a certain range of temperatures since the physical state is important for thermoelectric applications. Figure 2 shows the DSC curves of PEDOT:PSS, PEDOT:Tos and PEDOT:ClO_4 with no indication of a well-defined glass transition temperature. In the first DSC scan an endothermic peak around 100 – 110 °C is observed in all cases related to the melting of the PEDOT crystals [16]. No presence of free water in the samples is revealed by the absence of a peak near 0 °C. No peaks were observed during a second temperature scan indicating that the sample did not have enough time to re-crystallize during the quick cooling. The PEDOT chains tend to form crystals during the synthesis or during slow cooling if there is enough time to reorganize themselves.

Similar curves are observed for PEDOT:Tos and PEDOT:PSS but in the case of PEDOT:ClO_4 the heat flow increases from 140 °C possibly due to a degradation process.

In order to detect the characteristic vibration modes of PEDOT, the Raman analysis has been made in all the samples. Figure 3 shows the Raman spectra of the three samples. Different bands have been detected: around 1360 cm^{-1} the $C_\beta - C_\beta$ stretching, around 1440 cm^{-1} the symmetric stretching $C_\alpha = C_\beta(-O)$ and the asymmetric tension band $C = C$ splitted into two bands with peaks at 1506 cm^{-1} and 1568 cm^{-1}. Table 1 summarizes the vibration modes observed in all spectra [17, 18].

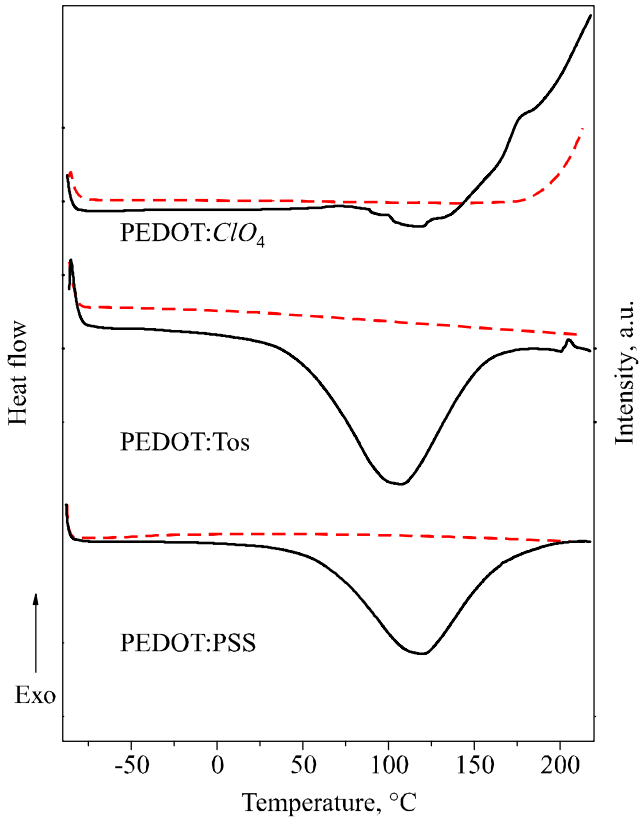

Fig. 2. DSC of PEDOT:PSS, PEDOT:Tos and PEDOT:ClO_4 (black line is the first scan and dash red line is the second scan).

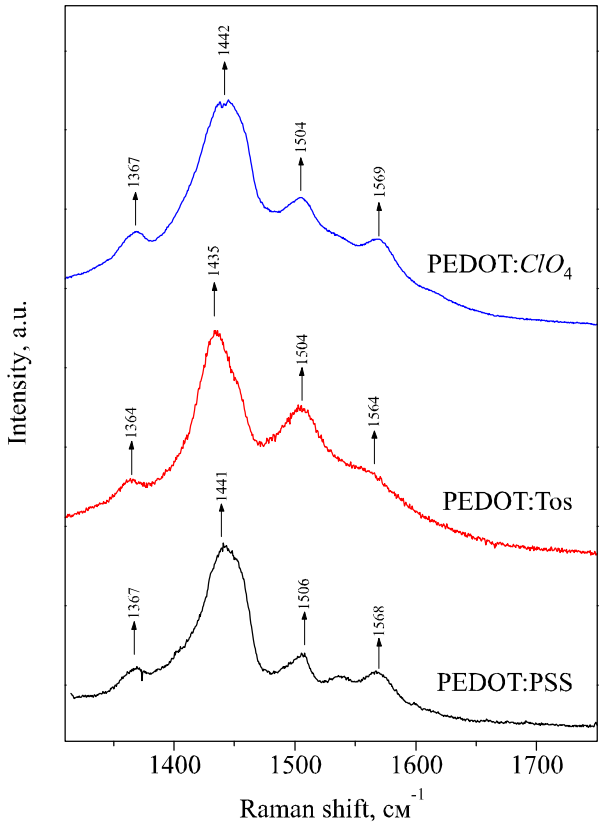

Fig. 3. Raman spectra of PEDOT:PSS, PEDOT:Tos and PEDOT:ClO_4.

No significant differences have been detected among the different samples; the vibrations correspond to the polymer backbone that in the three types of samples is the same, PEDOT.

Table 1

Vibration modes of PEDOT:PSS, PEDOT:Tos and PEDOT:ClO_4

PEDOT:PSS		PEDOT:Tos		PEDOT:ClO_4	
Raman shift (cm^{-1})	Assignation	Raman shift (cm^{-1})	Assignation	Raman shift (cm^{-1})	Assignation
1367	$C_\beta - C_\beta$ – str	1364	$C_\beta - C_\beta$ – str	1367	$C_\beta - C_\beta$ – str
1441	sym $C_\alpha = C_\beta(-O)$ str	1435	sym $C_\alpha = C_\beta(-O)$ str	1442	sym $C_\alpha = C_\beta(-O)$ str
1506/1568	asym $C = C$ str	1504/1564	asym $C = C$ str	1504/1569	asym $C = C$ str

Electrical conductivity was measured at 298 K, because it is the representative temperature for room temperature applications. Table 2 compiles the values of electric conductivity, the Seebeck coefficient, power factor (PF) and figure of merit (*ZT*) for PEDOT:PSS, PEDOT:Tos and PEDOT:ClO_4 systems. The electric conductivity data obtained by the van der Pauw method are: 0.16, 1.53 and 753 S/cm for PEDOT:PSS, PEDOT:Tos and PEDOT:ClO_4, respectively.The very high conductivity of PEDOT:ClO_4 is possibly due to the electrochemical synthesis that induces structural order and polymer chains longer than the oxidative synthesis. The Seebeck coefficient values obtained as a function of the type of counterion are: 8.7, 13.2 and 9.31 μV/K for PEDOT:PSS, PEDOT:Tos and PEDOT:ClO_4, respectively. The Seebeck coefficient is relatively constant with the type of counterion. The power factor, $PF = S^2T\sigma$ has been calculated in order to compare the relative efficiency of these materials, with values of 1.2×10^{-3}, 2.6×10^{-2} and 6.52 μW/mK^2 for PEDOT:PSS, PEDOT:Tos and PEDOT:ClO_4, respectively. The best value has been obtained for PEDOT:ClO_4 due to its high electrical conductivity. To compare with other inorganic materials studied in the bibliography, the *ZT* value has been calculated by assuming a coherent value of the thermal conductivity. In this work, we assume a value of 0.2 W/mK for the thermal conductivity, that is the value reported for PEDOT:PSS by several authors [19, 20]. A good value of $ZT = 0.01$ was obtained for PEDOT:ClO_4 in this paper. The comparison with other conductive polymers gives values of *ZT* of 7.9×10^{-5} for polyaniline doped with *HCl* [21] or of $0.01 - 2.3 \times 10^{-3}$ in the case of polythieno [3, 2-*b*] thiophene [22] indicating that improved *ZT* values have been obtained in this paper. However, when comparing with similar systems, we find in the literature values of *ZT* of 0.04 for PEDOT:PSS [23] and 0.25 for PEDOT:Tos [24]. Probably, the discrepancy between actual values and the ones obtained by Bubnova et al [23, 24] relies on the fact that different ways of sample processing are utilized, that is, pressed pellets against thin films.

Table 2

Electrical conductivity, Seebeck coefficient, Power Factor and ZT assuming 0.2 W/mK for thermal conductivity, of PEDOT:PSS, PEDOT:Tos and PEDOT:ClO_4 at 298 K

Sample	σ (S/cm)	*S* (μv/K)	PF (μW/mK^2)	*ZT*
PEDOT:PSS	0.16	8.70	1.2×10^{-3}	2×10^{-6}
PEDOT:Tos	1.53	13.20	2.6×10^{-2}	4×10^{-5}
PEDOT:ClO_4	753.00	9.31	6.52	1×10^{-2}

Conclusion

PEDOT with several counterions have been prepared by oxidative and electrochemical synthesis. DSC analysis indicates the presence of endothermic peaks due to a partial crystalline structure. Electrical conductivity strongly depends on the counterion, while the Seebeck coefficient does not significantly. Thermoelectric power of these systems is dominated by the electrical conductivity. Although the best *ZT* value obtained in this work was 100 times lower than the best inorganic materials, PEDOT:ClO_4 can be the starting point for new high performance thermoelectric composites.

Acknowledgements. The authors are grateful to the Ministry of Finances and Competitiveness (MINECO) of Spain for financial support through Grants CSD2010-00044 of the Programme ‘‘Consolider Ingenio 2010’’, MAT2012-33483 and the FPU programme of MINECO.

References

1. G.W. Crabtree, N.S. Lewis, Solar Energy Conversion, *Phys. Today* **60**, 37 (2007).
2. J.C. Lin, Y. Huang, K.D. She, M.C. Li, J.H. Chen, and S. Kuo, Development of Low-Cost Micro-thermoelectric Coolers Utilizing MEMS Technology, *Sensors and Actuators A:Physical* **148**, 176 (2008).
3. M. Rahmoun, K. Hachami, A. Touil, B. Bellach, M. Bailich, and A. Merdani, *Active and Passive Electronic Components* (2011). doi:10.1155/2011/708361
4. J. Liu, X.G. Wang, and L.M. Peng, Solvothermal Synthesis and Growth Mechanism of *Ag* and *Sb Co*-doped *PbTe* Heterogeneous Thermoelectric Nanorods and Nanocubes, *Mat. Chem. Phys*.**133**, 33 (2012).
5. Q. Shen, J. Li, and L. Zhang, A Study on *Sn* Ion Implantation into Lead Telluride Thermoelectric Material, *Sol. Energy Mater.Sol. Cells* **62**, 167 (2000).
6. K.T. Kim, H.M. Lee, H.M. Kim, D.W. Kim, K.J. Ha, G.H. Lee, and G. Geun, Bismuth-Telluride Thermoelectric Nanoparticles Synthesized by Using a Polyol Process, *J. Korean Phys. Soc*. **57**, 1037 (2010).
7. N. Peranio, M. Winkler, D. Bessas, Z. Aabdin, J. Koenig, H. Boettner, R.P. Hermann, and O. Eibl, Room-Temperature MBE Deposition, Thermoelectric Properties, and Advanced Structural Characterization of Binary Bi_2Te_3 and Sb_2Te_3 Thin Films, *J. Alloys Compd*. **521**, 163 (2012).
8. Y. Wang, K.F. Cai, J.L. Yin, B.J. An, Y. Du, and X. Yao, In situ Fabrication and Thermoelectric Properties of *PbTe*-polyaniline Composite Nanostructures, *J. Nanopart. Res* **13**, 533 (2011).
9. N. Toshima, Conductive Polymers as a New Type of Thermoelectric Material, *Macromol. Symp*.**186**, 81 (2002).
10. B.Y. Lu, C.C. Liu, S. Lu, J.K. Xu, F.X. Jiang, Y.Z. Li, and Z. Zhang, Thermoelectric Performances of Free-Standing Polythiophene and Poly (3-methylthiophene) Nanofilms, *Chin. Phys. Lett*. **27**, 57201 (2010).
11. B. Zhang, J. Sun, H.E. Katz, F. Fang, and R.L. Opila, Promising Thermoelectric Properties of Commercial PEDOT:PSS Materials and Their Bi_2Te_3 Powder Composites, *ACS Appl. Mater. Interfaces* **2**, 3170 (2010).
12. N. Dubey and M. Leclerc, Conducting Polymers: Efficient Thermoelectric Materials, *J. Polym. Sci., Part B: Polym. Phys*.**49**, 467 (2011).
13. J. Joo, K.T. Park, B.H. Kim, M.S. Kim, S.Y. Lee, C.K. Jeong, J.K. Lee, D.H. Park, W.K. Yi, S.H. Lee, K.S. Ryu, Conducting Polymer Nanotube and Nanowire Synthesized by Using

Nanoporous Template: Synthesis, Characteristics and Applications*, Synth. Met*. 135 – 136, **7** (2003).
14. Y. Cao, A.E. Kovalev, R. Xiao, J. Kim, T.S. Mayer, and T.E. Mallouk, Electrical Transport and Chemical Sensing Properties of Individual Conducting Polymer Nanowires, *Nano. Lett*. **8**, 4653 (2008).
15. L.J. Van Der Pauw, A method of Measuring the Resistivity and Hall Coefficient on Lamellae of Arbitrary Shape *Philips Techinical Review* **20**, 220 (1958).
16. X. Zhang, C. Li and Y. Luo, Aligned/Unaligned Conducting Polymer Cryogels with Three-Dimensional Macroporous Architectures from Ice-Segregation-Induced Self-Assembly of PEDOT-PSS, *Langmuir* **27** (5), 1915 – 1923 (2011).
17. B. Stavytska, M. Kelley and A. Myers, Surface-Enhanced Raman Study of the Interaction of PEDOT:PSS with Plasmonically Active Nanoparticles, *J. Phys. Chem. C* **114**, 6822 (2010).
18. S. Garreau, G. Louarn, J.P. Buisson, G. Froyer, S. Lefrant. In Situ Spectroelectrochemical Raman Sudies of Poly (3,4-ethylenedioxythiophene) (PEDT), *Macromolecules* **32**, 6807 (1999).
19. F.X. Jiang, J.K. Xu, B.Y. Lu, Y. Xie, R.J. Huang and L.F. Li, Thermoelectric Performance of Poly (3, 4-ethylenedioxythiophene): Poly(styrenesulfonate), *Chin. Phys. Lett*. **25**, 2202 (2008)
20. K.C. See, J.P. Feser, C.E. Chen, A. Majumdar, J.J. Urban and R.A. Segalman. Water-Processable Polymer-Nanocrystal Hybrids for Thermoelectrics, *Nano. Lett*. **10**, 4664 (2010).
21. F. Yakuphanoglu, B.F. Senkal, and A. Sarac, Electrical Conductivity, Thermoelectric Power, and Optical Properties of Organo-Soluble Polyaniline Organic Semiconductor, *J. Electron. Mat*. **37**, 930 (2008).
22. R. Yue, S. Chen, B. Lu, C. Liu, J. Xu, Facile Electrosynthesis and Thermoelectric Performance of Electroactive Free-Standing Polythieno [3, 2-*b*] thiophene Films, *J. Solid State Electrochem.* **15**, 539 (2011).
23. O. Bubnova, M. Berggren, and X. Crispin, Tuning the Thermoelectric Properties of Conducting Polymers in an Electrochemical Transistor, *J. Am. Chem. Soc*. **134**, 16456 (2012).
24. O. Bubnova, Z.U. Khan, A. Malti, S. Braun, M. Fahlman, M. Berggren, X. Crispin, Optimization of the Thermoelectric Figure of Merit in the Conducting Polymer Poly (3, 4-ethylenedioxythiophene), *Nat. Mater*. **10**, 429 (2012).

Submitted 30.05.2013.

L.D. Ivanova[1], V.V. Molokanov[1], A.V. Krutilin[1], P.P. Umnov[1], N.V. Umnova[1], O.N. Uryupin[2], A.A. Shabaldin[2]

[1]Federal State Budget Institution of Science A.A. Baikov Institute for Metallurgy and Materials Science of the RAS, 49, Leninsky prosp., Moscow, 119991, Russia;
[2]Federal State Budget Institution of Science A.F. Ioffe Physical-Technical Institute of the RAS, 26, Politechnicheskaya Str., Saint-Petersburg, Russia

USE OF THE TAYLOR-ULITOVSKY METHOD TO PREPARE THERMOELECTRIC MATERIALS OF BISMUTH AND ANTIMONY TELLURIDE SOLID SOLUTION

Conditions for producing glass-coated wires of bismuth and antimony telluride solid solution using the Taylor-Ulitovsky method have been investigated. The influence of coating materials (the type of glass) and drawing rate on the process of formation of wires of different diameter has been studied. The optimal conditions for producing extended wires (up to 1 m) with the core diameter from 100 to 250 μm and stable in length geometrical parameters have been established. The structure of wire breaks has been investigated though use of scanning electron microscopy. The Seebeck coefficient has been measured in the range of temperatures 70 to 420 K as a function of wire diameter. The outlook for using the Taylor-Ulitovsky method to produce rather thin legs of microcoolers that cannot be cut of currently employed materials has been shown.

Key words: Taylor-Ulitovsky method, microwires, solid solution of bismuth and antimony tellurides, Seebeck coefficient.

Introduction

Thermoelectric power converters have gained wide application nowadays in a variety of science and technology fields. Particularly topical is the problem of thermoelectric device efficiency improvement. At the present time, attention has been focused on studying the possibility of considerable increase of thermoelectric figure of merit of materials due to their nanostructuring. Thermoelectric materials based on nanopowders are in research and development stage in our country, as well as abroad. Theory predicts increase in ZT of nano-sized thermoelectric material to 3.5 only in the case when grain size will be less than 10 nm [1]. Until the present time, the bulk thermoelectric materials with grain size on the level of nanometer units have not been obtained yet. There are experimental works presenting the data on materials with highly dispersed structure for which ZT reaches the values of 1.2 to 1.5 [2, 3]. Fabrication of glass-coated microwires by Taylor-Ulitovsky method based on Bi и Bi_2Te_3 is reported in the literature [4-7]. The possibility of considerable increase of thermoelectric figure of merit of material in this structure is indicated. In a number of cases, microcoolers with the leg size less than hundreds of microns are required. Therefore, in the development of new types of microcoolers, of interest can be microwires based on solid solutions of p- and n-type bismuth and antimony chalcogenides with sufficiently high thermoelectric figure of merit.

The purpose of this work is to develop conditions for preparation of $Bi_{0.5}Sb_{1.5}Te_3$ solid solution in the form of glass-coated wires using the Taylor-Ulitovsky method.

Preparation of $Bi_{0.5}Sb_{1.5}Te_3$ solid solution by the Taylor-Ulitovsky method

According to this method, material placed in a glass tube is melted and, together with a coating which is softened, is drawn at a certain rate. The schematic of microwires fabrication is shown in Fig. 1.

As an original material use was made of a single crystal of Czochralski grown solid solution $Bi_{0.5}Sb_{1.5}Te_3$ [8]. The melting point of this material was 610 °C. The single crystal had a well-expressed layered crystalline structure typical of materials with tetradymite structure. A chip of this single crystal is represented in Fig. 2. Cleavage planes are clearly seen that are arranged perpendicular to the main crystallographic axis *c*.

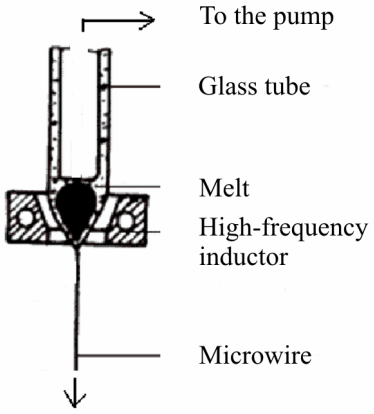

Fig. 1. Schematic of glass-coated thin wires fabrication from the melt by the Taylor-Ulitovsky method.

The experiments in this work were performed with the use of glass tubes made of various types of glass: silicate, molybdenum, borate (pyrex) with different softening temperatures from 500 to 750 °C. Typical appearance of the resulting wires of thermoelectric material with a coating of these glasses is shown in Fig. 3 *a*, *c*. It was established that with the use of tubes of low-melt silicate glass with softening temperature 500 − 580 °C possessing low thermal stability, cracking of glass coating takes place on the wire samples (Fig. 3 *a*). Molybdenum and pyrex glasses are more temperature-resistant (Fig. 3 *b*). However, to fabricate wires in tubes of these glasses, the melt must be overheated to temperatures 950 – 1100 °C. In this work, melt temperature ~ 950 °C was maintained. As was established later, such overheat resulted in tellurium evaporation and a change in wire material composition, as compared to the original material, since the process was not carried out from closed volume.

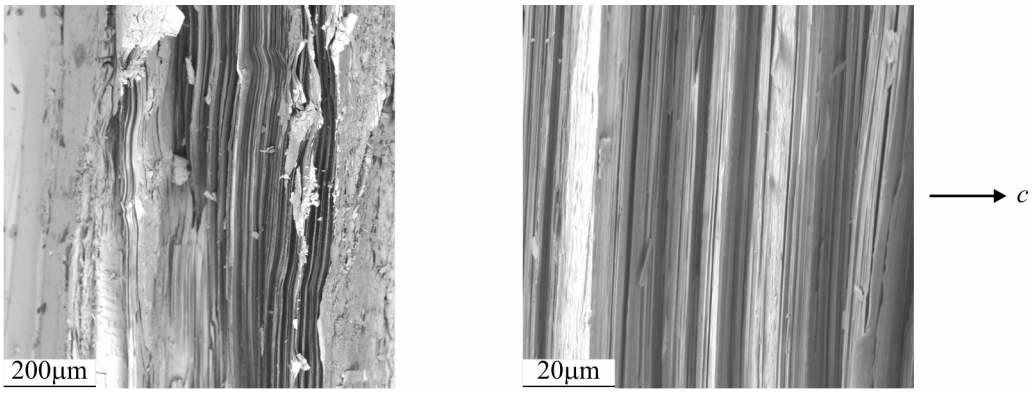

Fig. 2. SEM image of a chip of the original single crystal $Bi_{0.5}Sb_{1.5}Te_3$ obtained with different magnification.

The effect of drawing rate on the process of formation of wires of different diameter was investigated. The wires of material in pyrex and molybdenum glass coating with core diameter from 2 mm to 0.1 mm of 1 m in length were obtained. Investigations performed on scanning electron microscope have shown that the surface of material adjacent to the glass is smooth, glossy, without visible defects (Fig. 2 *b*). It has been established that samples of wires with the core diameter from 100 to 250 μm retain their cylinder shape (Fig. 3 *a*, *c*) with drawing rates from 1 m/s to 0.05 m/s. Core

breaks have a directed crystalline layered structure with well-expressed cleavage planes typical of these materials (Fig. 3 *d*, *e*). Further reduction of drawing rate (less than 0.05 m/sec) results in the distortion of core section, namely the diameter assumes the shape of an ellipse (Fig. 3 *f*).

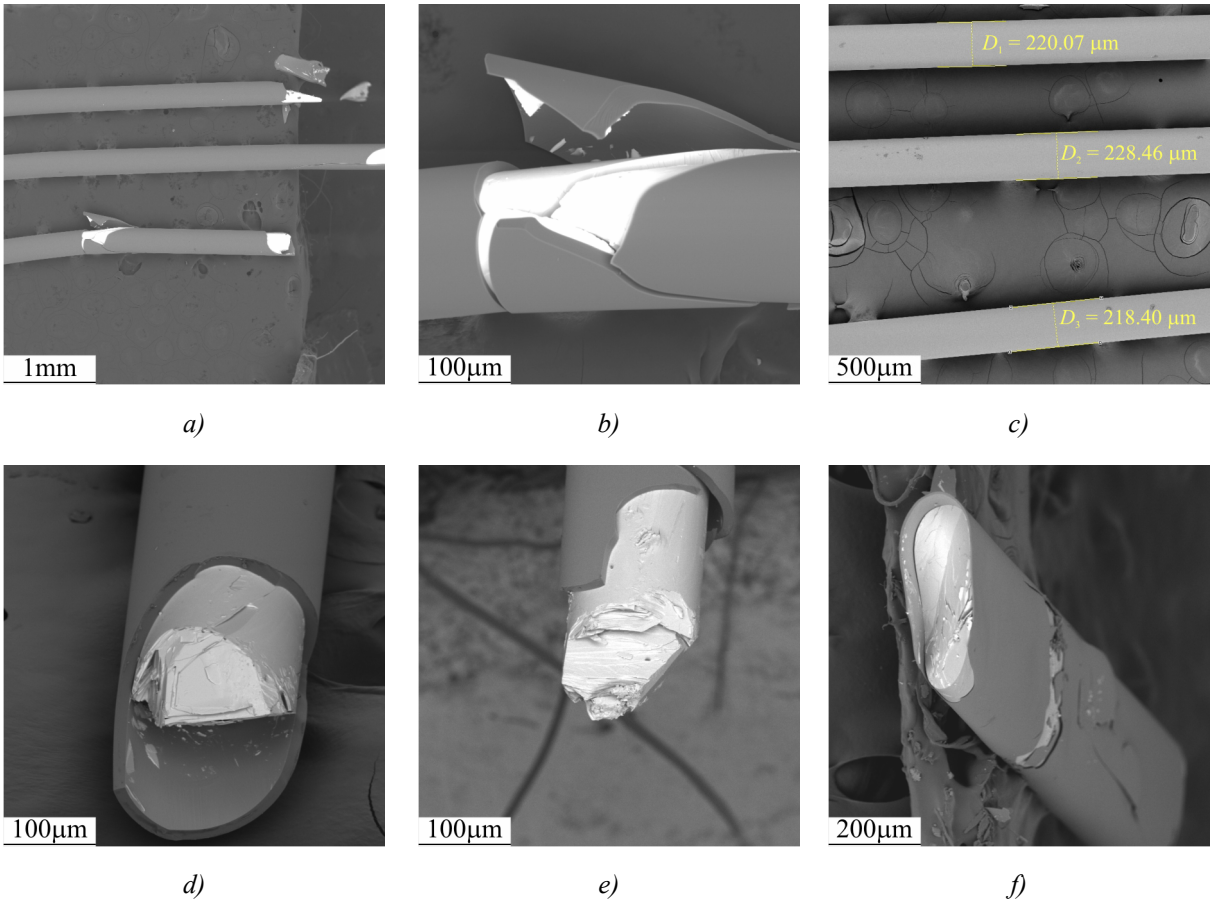

Fig. 3. Wires (a, c) and breaks (b, d, e, f, g) in glass-coated $Bi_{0.5}Sb_{1.5}Te_3$: molybdenum glass (a, b), pyrex (c, d, e, f, g). Drawing rates 0.1 m/s (a, b, c, d, e), 0.03 m/s (f).

The Seebeck coefficient of the wires

The Seebeck coefficient is known to be one of the most informative characteristics of thermoelectric materials. This parameter does not depend on sample geometry and, by its value, one can judge of current carrier concentration in the measured material. In Saint-Petersburg, an experimental setup was developed for measuring the Seebeck coefficient of quantum-size nanowires in the range of temperatures 80 to 400 K by the relative method [9]. Measurements are performed in a vacuum chamber. Calibrated constantan is used as a reference. Temperature difference is created by heat flux from the source of light incident on thermal radiation detector. The temperature dependence of the Seebeck coefficient of object under study is measured simultaneously with the Seebeck coefficient of the reference. The accuracy of measurement over the entire range of temperatures is estimated as 12 %.

Fig. 4 represents the temperature dependences of the Seebeck coefficient for wires of different diameter (represented together with glass coating) and a single crystal used as the original ingot. The results obtained are compared to the Seebeck coefficient of this single crystal measured by the absolute method in given temperature range (Fig. 4, curve 4).

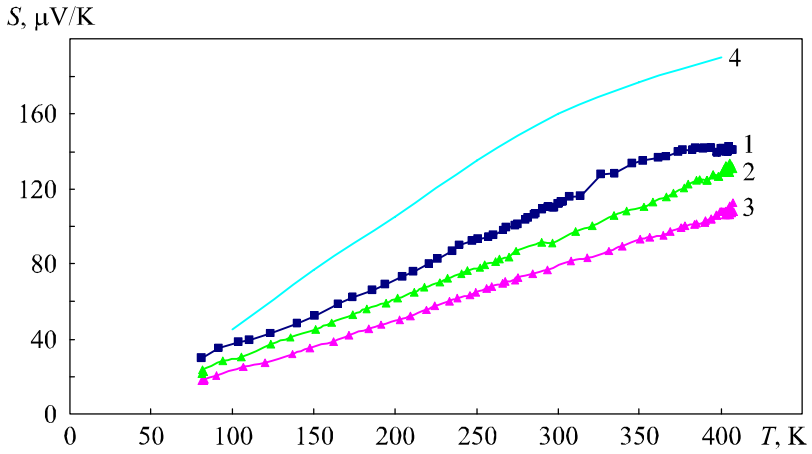

Fig. 4. Temperature dependences of the Seebeck coefficient for glass-coated $Bi_{0.5}Sb_{1.5}Te_3$ wires; outside diameter 0.2 mm (1), 0.3 mm (2), 0.4 mm (3) and the original ingot (4).

It was established that the wires have lower Seebeck coefficient values than the original single crystal over the entire range of temperatures. In so doing, a thinner wire (outside diameter 200 μm, curve 1) is matched by higher Seebeck coefficient values. The above effect can be due to strong stresses created by glass coating [6, 10]. On the other hand, it is known that the Seebeck coefficient value depends on the degree of material composition deviation from stoichiometric composition towards tellurium deficit. Thus, the composition of solid solution generally used in the products can be represented as $Bi_{0.5}Sb_{1.5}Te_{3-x}$ ($0.005 \le x \le 0.08$), and in the region of tellurium solubility (~ 0.2 at. %) charge carrier concentration can vary several times and, accordingly, the Seebeck coefficient at room temperature can change from 80 to 220 μV/K [11]. Therefore, with increase in the degree of deviation of solid solution composition toward tellurium decrease, there is increase in carrier concentration and, accordingly, decrease in the Seebeck coefficient. Experiments on formation of the wires were conducted with open melt surface, from which volatile components were evaporated. For glass softening the melt was overheated to temperature ~ 950 °C, whereas ingot melting temperature was ~ 610 °C. Exactly for this reason, thermoelectric materials in the form of glass-coated wires had a higher current carrier concentration and, accordingly, a lower Seebeck coefficient than the original single crystal.

To produce materials with a lower carrier concentration, corrections must be introduced into process technology, to assure correspondence to given composition and take into account the effect of stresses created by glass coating.

Conclusions

The task of producing the legs for microcoolers has been solved with the aid of the Taylor-Ulitovsky method, using the variant of forced melt drawing similar to known method of fiber glass fabrication. The effect of coating materials and drawing rates on core formation processes in $Bi_{0.5}Sb_{1.5}Te_3$ solid solution has been investigated. Optimal conditions for producing sufficiently extended wires (to 1 m) of stable form with the core diameter from 100 to 250 μm have been established. Wires with the Seebeck coefficient from 100 to 140 μV/K at 400 K have been produced.

For conformity between core composition and the original ingot composition it is required to ensure formation of wires with closed melt volume.

The work has been performed with the financial support of Russian Foundation for Basic Research Project № 13-08-00041 a.

References

1. L.D. Hicks, T.C. Harman, and M.S. Dresselhaus, Use of Quantum-Well Superlattices to Obtain a High Figure of Merit from Nonconventional Thermoelectric Materials, *Appl. Phys. Lett*. **63** (23), 3230 − 3232 (1993).
2. B. Poudel, Q. Hao, Yi Ma, Y.C. Lan, A. Minnich, Bo Yu, X. Yan, D. Wang, A. Muto, D. Vashaee, X.Y. Chen, Y.M. Lui, M.S. Dresselhaus, G.G. Chen, and Z. Ren, High-Thermoelectric Performance of Nanostructured Bismuth Antimony Telluride Bulk Alloys, *Science* **320** (5876), 634 – 638 (2008).
3. W. Xie, X. Tang, Y. Yan, and T. Tritt, Unique Nanostructures and Enhanced Thermoelectric Performance of Melt-spun *BiSbTe* Alloys, *J. Appl. Phys*. **94**, 102111/1-3 (2009).
4. A.A. Nikolaeva, L.A. Konopko, A.K. Tsurkan, and O.V. Botnar, Anisotropy of Thermoelectric Properties of *Bi* and *Bi-Sn* Nanowires for Thermoelectric Applications, *Metallofizika i Noveishie Technologii* **33** (1), 77 – 85 (2011).
5. D. Meglei, M. Dantu, S. Donu, and A. Russu, Microthermocouple of Bifilar Microwires Based on Bi_2Te_3 Thermoelectric Materials, *J. Thermoelectricity* **2**, 61 – 65 (2009).
6. I.A. Popov, P.P. Budyul, E.F. Moloshnik, and O.V. Botnar, Increase of Thermoelectric Figure of Merit of $Bi_{1-x}Sb_x$ Thin Wires under Elastic Tension in a Magnetic Field, *J. Thermoelectricity* **2**, 37 – 46 (2008).
7. I. Shiota, H. Kohri, M. Kato, and I.J. Ohsugi, Fine Bi_2Te_3 Wires Fabricated by Glass Sealed Melt Spinning, *Proc. 25th International Conference on Thermoelectrics* (2006), pp. 247 – 251.
8. L.D. Ivanova, Yu.V. Granatkina, Single Crystals of Solid Solutions of *p*-type Bismuth and Antimony Chalcogenides Intended for Cooling to $T < 150$ K, *Inorganic Materials* **37**(2), 199 − 202 (2001).
9. O.N. Uryupin, A.A. Shabaldin, Procedure for Measurement of the Seebeck Coefficient in Quantum Semiconductor Wires, *Thermoelectrics and their Application* (Saint-Petersburg, 2006), pp. 346 − 350.
10. P.P. Umnov, N.V. Kurakova, Yu.S. Shalimov, M.I. Pertzhik et al., Effect of Stresses Created by Glass Encapsulation on Melt Solidification Process when Manufacturing a Microwire of Magnetically Soft Alloy $Co_{69}Fe_4Cr_4Si_{12}B_{11}$, *J. Advanced Materials* **1**, 79 – 85 (2009).
11. N. Kh.Abrikosov, V.F. Bankina, L.A. Kolomoyets, and N.V. Dzhamashvili, Deviation of Solid Solution from Bi_2Te_3-Sb_2Te_3 Stoichiometric Cut in the Field of $Bi_{0.5}Si_{1.5}Te_3$ Composition, *Izvestia AN SSSR: Inorganic Materials* 13 (5), 827 − 829(1977).

Submitted 22.07.2013.

D.M. Freik[1], B.S. Dzundza[1], Ya.S. Yavorsky[1], O.B. Kostyuk[1], T.S. Lyuba[2]

[1]Vasyl Stefanyk Precarpathian National University,
57, Shevchenko Str., Ivano-Frankivsk, 76018, Ukraine;
[2]Ivan Ohienko Kamyanets-Podilsky National University,
61, Ohienko Str., Kamyanets-Podilsky, 32300, Ukraine

THERMOELECTRIC PROPERTIES OF *PbTe-Bi$_2$Te$_3$* SOLID SOLUTION THIN FILMS

Thermoelectric properties of films based on PbTe-Bi$_2$Te$_3$ solid solutions of different composition prepared by vapour condensation in open vacuum on glass-ceramic and mica substrates have been investigated. Based on the two-layer Petritz model, thermoelectric parameters of near-surface layers have been determined. It is shown that thin films on (0001) fresh cleavages of muscovite mica containing ~ 1 mol. % Bi$_2$Te$_3$ are characterized by maximum values of thermoelectric power ~ 95 μW/K^{2}cm.

Key words: thin films, lead telluride, solid solutions, thermoelectric properties.

Introduction

Lead telluride is an efficient thermoelectric material for medium-temperature region (500 – 750) K [1-4]. Thin-film material expands considerably the limits of its practical application. Owing to the size and surface effects, the thermoelectric parameters of a condensate are significantly different from those of bulk analog. Despite the large number of publications [5-7], the problem of surface effect on the entire set of thermoelectric parameters of thin films based on lead chalcogenides remains unsolved. Moreover, on their exposure to the air, due to acceptor oxygen effect, a layer rich in *p*-type carriers is formed on the surface [7]. So, attempts to obtain *n*-type thin-film material based on pure lead telluride with stable thermoelectric parameters often fail. Earlier it had been revealed that doping of *PbTe* with V group elements, in particular, *Bi*, yields a condensate with high values of thermoelectric power [8].

This paper studies the regularities of change in thermoelectric parameters of films based on *PbTe*-*Bi$_2$Te$_3$* solid solutions of different composition, obtained from vapour phase on glass-ceramic and mica substrates, as a function of their thickness.

Experimental procedure

Films for investigation were obtained by vacuum deposition of synthesized material vapour onto (0001) fresh cleavages of muscovite mica and glass-ceramic substrates. The elaborated construction of vacuum sectional heaters yielded vapour-phase structures both of different thickness (d) at given deposition temperature T_s, and of equal thickness at different deposition temperatures in a single technological cycle without vacuum system depressurization [9]. The evaporator temperature during deposition was T_e= 970 K, and substrate temperature T_s = 470 K. Film thickness was assigned by deposition time within 15 – 75 s and measured by means of MII-4 microinterferometer. For evaporation, use was made of a pre-synthesized material, namely *PbTe-Bi$_2$Te$_3$* solid solutions with 1, 3 and 5 mol.% *Bi$_2$Te$_3$*.

The electric parameters of films were measured in the air at room temperatures in constant magnetic fields on the elaborated automated plant providing the processes of electric parameter measurement, as well as recording and primary processing of data with the possibility of constructing the plots of time and temperature dependences. The measured sample had four Hall and two current contacts. Silver films were used as ohmic contacts. Current through the samples was ≈ 1 mA. Magnetic field was applied perpendicular to the surface of films at induction of 1.5 T.

The obtained samples were investigated using a Digital Instruments Dimension 300 Atomic Force Microscope (AFM) and Nanoscope 3a controller in periodic contact mode. The measurements were performed in the centre of the samples using serial silicone probes NSG-11 with a nominal radius of edge rounding to 10 nm (NT-MDT, Russia). According to the results of AFM investigations of vapour-phase condensates, the surface morphology and its profilograms were determined.

The results of AFM investigations and the thickness dependences of electric conductivity (σ), the Seebeck coefficient (S) and thermoelectric power ($S^2\sigma$) for $PbTe$-Bi_2Te_3 films are shown in Figs. 1 – 4.

Research results and their analysis

Introduction of Bi_2Te_3 causes active donor effect in lead telluride which is manifested in considerable growth of electron concentration up to ~10^{10} cm^{-3}. The latter is due to the fact that in n-$PbTe$-Bi_2Te_3 solid solution bismuth with configuration of valence electrons $6s^26p^3$ substitutes lead with configuration of valence electrons $6s^26p^2$, in the cation sublattice lead telluride is an active donor ($Bi^{3+} \rightarrow Bi^{1+}_{Pb}$). Films prepared on mica substrates are characterized by high values of electric conductivity (σ) which with Bi_2Te_3 content 3 mol.% reaches the values over 1.3 10^3 Ω^{-1}cm^{-1}, and the Seebeck coefficient (S) and thermoelectric power ($S^2\sigma$) in this case are 120 μV/K and 17 μW/K^{2}cm, respectively. Films of one percent composition (~1 mol.% Bi_2Te_3), despite their considerably lower electric conductivity ($\sigma \approx 300$ Ω^{-1}cm^{-1}), are characterized by considerable thermoelectric power that reaches $S^2\sigma \approx 95$ μW/K^{2}cm owing to high values of the Seebeck coefficient ($S > 600$ μV/K). Films prepared on glass-ceramic substrates have lower values of electric conductivity $\sigma = (150 – 300)$ Ω^{-1}cm^{-1} and the Seebeck coefficient $S = (100 – 400)$ μV/K, providing thermoelectric power $S^2\sigma \approx 23$ μW/K^{2}cm.

It is seen from Fig. 1 that with increase in condensate thickness d, both on mica cleavages and on glass ceramics, irrespective of composition, conductivity (σ) increases with saturation at $d \approx 1$ μm. In this case of considerable importance are surface effects which become marginal with increasing thickness.

It is known that on exposure of films to the air, a layer rich in p-type carriers is formed on the surface due to acceptor oxygen effect [5]. To estimate the effect of near-surface layer on the electric properties of the films, the two-layer Petritz model has been used [10]. A thin film in this model consists of two layers: near-surface (I) (surface charge region) of thickness d_s, with charge carrier concentration n_s, and their mobility μ_s, and bulk (II), which is characterized by similar values: d_b, n_b, μ_b connected in parallel. The film thickness is $d = d_s + d_b$. In this case according to [10]:

$$\sigma = \frac{\sigma_s d_s + \sigma_b d_b}{d}; \tag{1}$$

$$R = \frac{R_s \sigma_s^2 d_s + R_b \sigma_b^2 d_b}{\left(\sigma_s d_s + \sigma_b d_b\right)^2} d; \tag{2}$$

$$\mu = \sigma R = \frac{\sigma_s{}^2 d_s R_s + \sigma_b{}^2 d_b R_b}{\sigma_s d_s + \sigma_b d_b}. \tag{3}$$

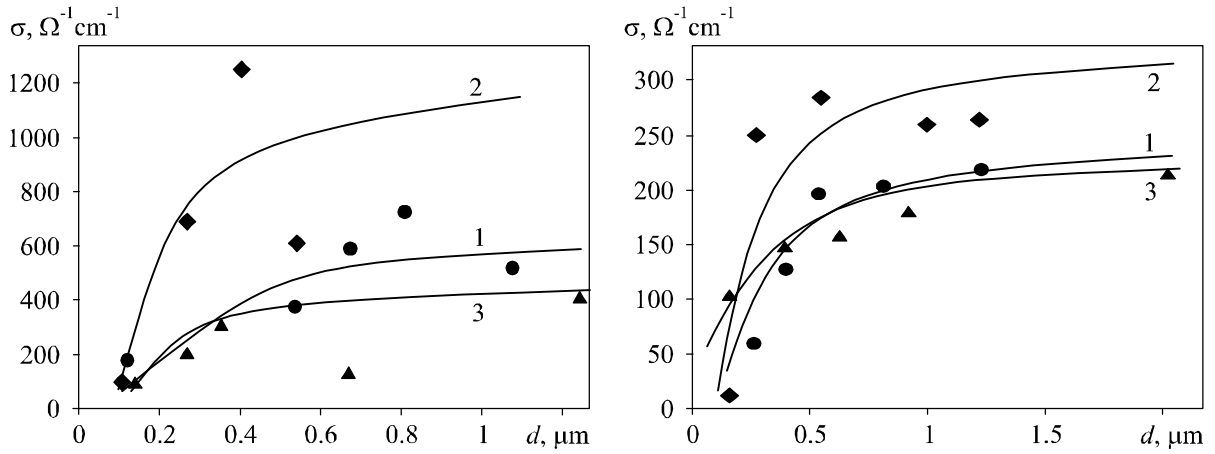

Fig. 1. Dependences of electric conductivity (σ) on thickness (d) of $PbTe$-Bi_2Te_3 films with Bi_2Te_3 content mol.%: (●, 1) – 5; (■, 2) – 3; (▲, 3) – 1, on mica (a) and glass-ceramic (b) substrates. Dots – experiment, solid lines – calculations according to the Petritz model.

Under the condition of known experimental values σ, R, μ and bulk σ_b, R_b, μ_b and d values, from the relations (1) – (3) one can estimate the near-surface layer parameters σ_s, R_s, μ_s, respectively.

The calculated thermoelectric parameters of near-surface layers estimated according to the Petritz model are given in the Table. The theoretical curves describe adequately the experimental results (Fig. 1 – 3) with certain values of near-surface thermoelectric parameters d_s, σ_s, S_s, $S^2\sigma_s$ (Table).

The near-surface layer thickness (d_s) (Table) is practically independent of composition, and is somewhat higher for films prepared on glass-ceramic substrates, which is attributable to their lower structural perfection as compared to samples on mica (Fig. 4).

Table

Thermoelectric parameter values of the near-surface layer (s) and volume (b) for $PbTe$-Bi_2Te_3 films of different composition, calculated according to the two-layer Petritz model

Substrate type	Mica			Glass ceramics		
Bi_2Te_3 content Parameters	5 mol.%.	3 mol.%.	1 mol.%.	5 mol.%.	3 mol.%.	1 mol.%.
d_s, μm	0.14	0.11	0.12	0.18	0.15	0.18
σ_s, $\Omega^{-1}cm^{-1}$	170	70	20	30	12	110
σ_b, $\Omega^{-1}cm^{-1}$	650	1200	500	250	350	230
S_s, μV/K	–70	–330	–959	–170	–600	–470
S_b, μV/K	–54	–90	–454	–145	–90	–304
$S^2\sigma_s$, $\mu W/K^2cm$	0.8	7.6	18.4	0.9	4.3	22.3
$S^2\sigma_b$, $\mu W/K^2cm$	1.9	9.7	103.1	5.1	2.8	21.3

The Seebeck coeffcient increases considerably to the values of 450 – 800 μV/K with reduction in film thickness (Fig. 2) which can caused by decreasing concentration of major carriers due to oxygen effect. For thick films (d > 700 nm), it is virtually independent of thickness (Fig. 2).

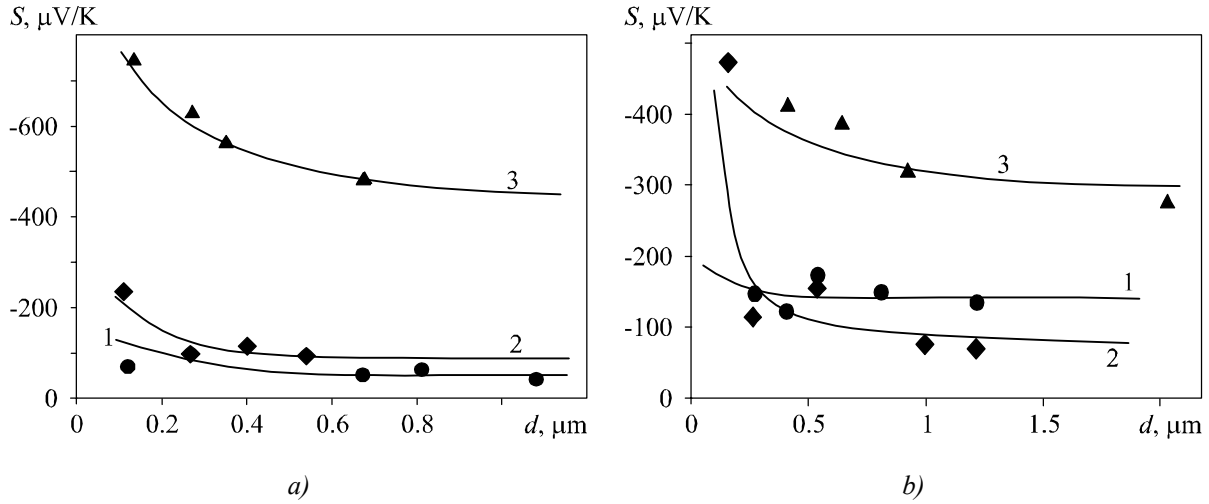

a) *b)*

Fig. 2. Dependences of the Seebeck coefficient (S) on thickness (d) of $PbTe$-Bi_2Te_3 films with Bi_2Te_3 content mol.%: (●, 1) – 5; (■, 2) – 3; (▲, 3) – 1, on mica (a) and glass-ceramic (b) substrates. Dots – experiment, solid lines – calculations according to the Petritz model.

Despite the high values of the Seebeck coefficient (S_s) in the near-surface layer, the thermoelectric power ($S_s^2\sigma_s$) near the surface of the majority of samples is considerably lower than in the bulk due to a drastic decrease in electric conductivity (σ_s) (Table). Electric conductivity of the near-surface layers (σ_s) is much lower than in the bulk (σ_b) (Table, Fig. 1) due to the influence of two factors: reduced concentration of major carriers caused by oxygen effect and their diffused scattering by the film surface (Fig. 4).

Thus, high values of electric conductivity (σ) combined with considerable value of the Seebeck coefficient (S_s) and thermoelctric power ($S^2\sigma$) of films based on $PbTe$-Bi_2Te_3 solid solutions with Bi_2Te_3 content 1 mol.% (Figs. 1 – 3 – curves 3) yielded stable in time *n*-type thermoelectric material, which is promising for use in thin-film micromodules for thermoelectric power conversion.

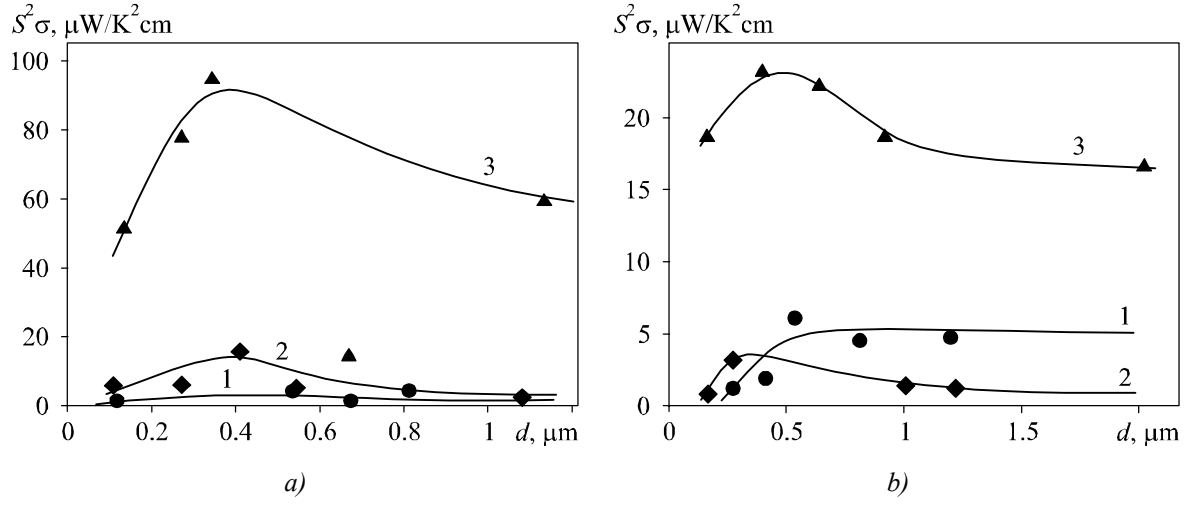

a) *b)*

Fig. 3. Dependences of thermoelectric power ($S^2\sigma$) on the thickness (d) of $PbTe$-Bi_2Te_3 films with Bi_2Te_3 content mol.%: (●, 1) – 5; (■, 2) – 3; (▲, 3) – 1, on mica (a) and glass-ceramic (b) substrates.

Fourfold thermoelectric power values of condensate on mica (~ 100 μW/K^{2}cm) compared to glass ceramics (~ 23 μW/K^{2}cm) for $PbTe$-Bi_2Te_3 solid solutions with ~ 1 mol.% Bi_2Te_3 are due to their structural

state (Fig. 4). Better developed and ordered intergrain architecture of condensate nanocrystallites on mica cleavages (Fig. 4 – I) compared to glass ceramics (Fig. 4 – II) is the reason for efficient throttling of charge carriers on potential barriers, which accounts for considerable growth of the Seebeck coefficient (Table).

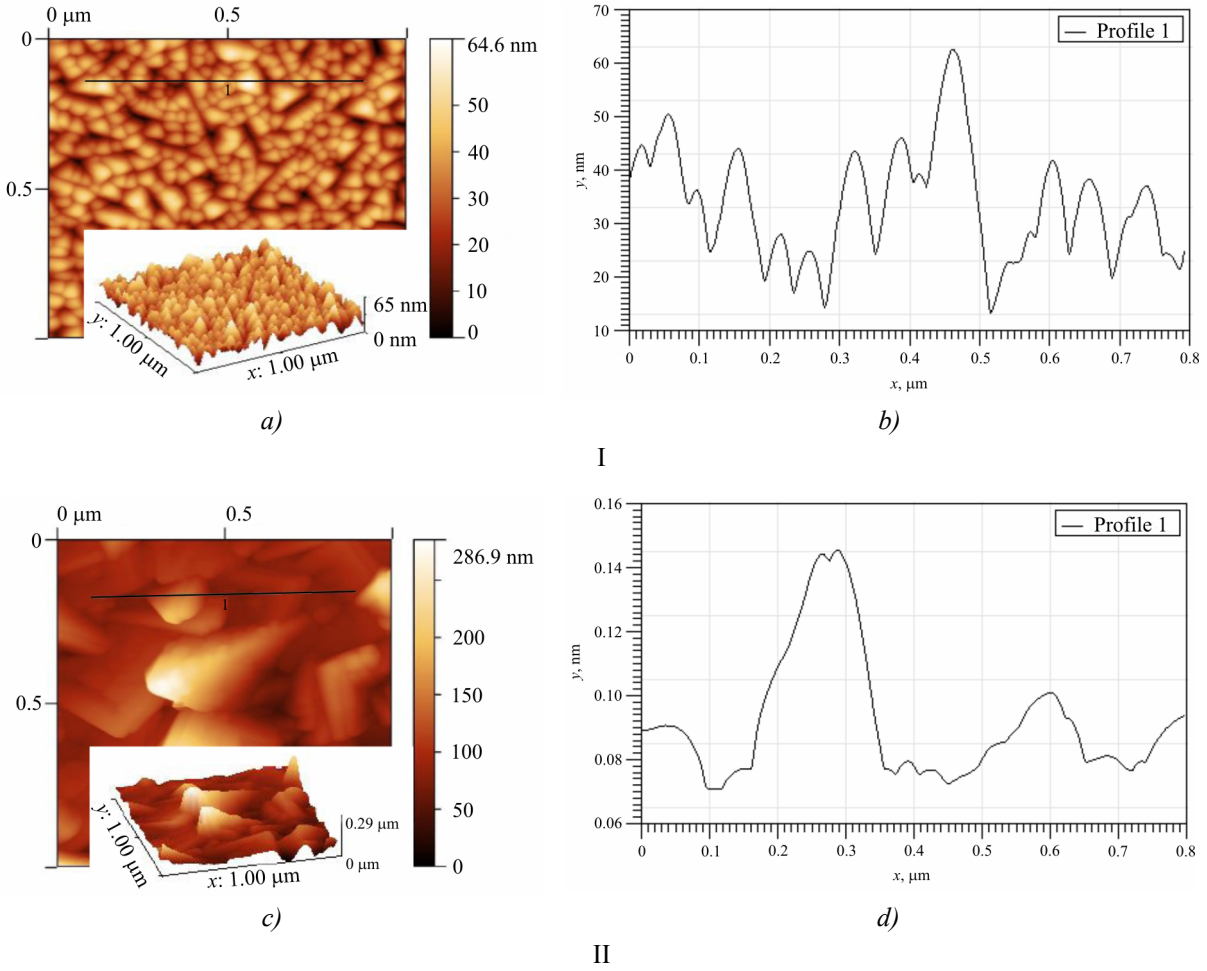

Fig. 4. 2D and 3D – ASM images (a) and profilographs (b) of the surface of vapour-phase condensates of PbTe-(1 mol.%)Bi_2Te_3 solid solutions deposited on fresh (0001) cleavage of muscovite mica (I) and glass ceramics (II): evaporation temperature T_e = 700 K, deposition temperature T_s = 470 K, deposition time 75 s.

It should be also noted that with increase in Bi_2Te_3 content in $PbTe$-Bi_2Te_3 solid solution condensates both on (0001) cleavages of muscovite mica and glass ceramics, the thermoelectric power of near-surface layers is reduced.

Conclusions

1. Thermoelectric properties of vapour phase thin films based on $PbTe$-Bi_2Te_3 solid solutions of different composition, deposited on glass-ceramic substrates and (0001) cleavages of muscovite mica have been investigated.
2. Using the two-layer Petritz model, the thermoelectric parameters of near-surface layer have been determined whose values are affected by atmospheric oxygen.
3. It has been shown that thin-film material based on $PbTe$-Bi_2Te_3 solid solutions with 1 mol.% Bi_2Te_3 has improved thermoelectric parameters on (0001) cleavages of muscovite mica.

The work was performed under support of integrated research project of Ministry of Education and Science of Ukraine (state registration number 0113U000185) and State Foundation for Basic Research of Ukraine (state registration number 0113U003689).

References

1. L.I. Anatychuk, *Thermoelements and Thermoelectric Devices. Reference Book* (Kyiv: Naukova Dumka, 1979), 769 p.
2. L.I. Anatychuk, *Thermoelectricity, Vol. 2, Thermoelectric Power Converters* (Kyiv, Chernivtsi: Institute of Thermoelectricity, 2003), 376 p.
3. V.M. Shperun, D.M. Freik, and R.I. Zapukhlyak, *Thermoelectricity of Lead Telluride and its Analogues* (Ivano-Frankivsk: Plai, 2000), 250 p.
4. D.M. Freik, M.A. Haluschak, and L.I. Mezhylovska, *Physics and Technology of Thin Films* (Lviv: Vyscha Shkola, 1988), 182p.
5. Yu.A. Boikov, V.A. Kutasov, Changes in the Charge Carrier Concentration and Mobility in *PbTe* Films on Completion of Condensation Process, *Physics of the Solid State* **23**(8), 2527 – 2529 (1981).
6. Yu.A. Boikov, V.A. Kutasov, Effect of Near-Boundary Layers on the Properties of Lead Telluride Thin Films, *Physics of the Solid State* **25** (10), 2984 – 2987 (1983).
7. Yu.V. Klanichka, B.S. Dzundza, L.I. Mezhylovska, Ya.S. Yavorsky, Processes of Interaction with Oxygen of Thin Films of IV-V Compounds, *Physics and Chemistry of Solid State* **12**, 346 (2011).
8. D.M. Freik, B.S. Dzundza, M.A. Lopyanko, Ya.S. Yavorsky, A.I. Tkachuk, and R.B. Letsyn, Structure and Electric Properties of Pure and Bismuth-Doped Lead Telluride Thin Films, *J. Nano-Electron.Phys*. **4** (2), 02012-1–02012-5 (2012).
9. D.M. Freik, Ya.S. Yavorsky, V.Yu. Potyak, and R.S. Yavorsky, Sectional Vacuum Heaters for Producing Vapour Phase Condensates, *Physics and Chemistry of Solid State* **13** (2), 509 – 511 (2012).
10. R.L. Petritz, Theory of an Experiment for Measuring the Mobility and Density of Carriers in the Space-Charge Region of a Semiconductor Surface, *Phys. Rev*. **110**, 1254 (1958).

Submitted 26.07.2013.

K.Sh. Kakhramanov, F.K. Aleskerov, S.Sh. Kakhramanov, S.A. Nasibova

Scientific and Production Association "Selen", National Academy of Sciences of Azerbaijan,
29 A, G. Dzavida Ave., Baku, AZ 1118, Azerbaijan

SELF-ORGANIZATION OF LOW-DIMENSIONAL NANOSTRUCTURES IN LAYERED CRYSTALS OF $A_2^{V}B_3^{VI}$ TYPE

Materials with nanoisland arrays, corrugated and stepped structures-nanowires of different size and density have been obtained. A mechanism of formation of the above nanostructures has been described, which is due to migration, coalescence and clustering of nanoislands in the interlayer space of undissolved impurity and superstoichiometric excess, as well as due to plastic deformation effect under a pressure of thermal wave forming corrugated structures. Single-dimensional charge flow channels have been discovered, the percolation character of charge carrier transport in the network with respective quantum dot distribution density has been determined. The thermoelectric performance of nanostructured crystals has been improved.

Key words: nanowires, clustering, nanoislands, deformation, corrugated structures, single-dimensional channels, percolation.

Introduction

Figure of merit improvement of thermoelectric materials by reducing the phonon component of thermal conductivity, as well as by increasing the Seebeck coefficient through density of states increase near the Fermi level is the subject of much investigation today. One of the ways to accomplish this purpose is reducing dimensions of thermoelectric component parts, namely using quantum dots and wires for efficient phonon scattering on the edges of these nanostructures, and using specific distribution in the density of states. The size and shape, and well as the composition of nanostructures markedly affect the electrophysical characteristics of material, and one must select optimal for thermoelectricity parameters which is associated with process design of materials with given properties. For instance, quantum dots, self-organizing in the interlayer space, efficiently scatter and restrict the propagation of phonon modes, but, at the same time, transport which is partially transformed to hopping type reduces charge carrier mobility. Therefore, it is necessary to select a mode with restricted phonon propagation and simultaneous efficient charge transport. In order to solve these problems, we employed nanostructured material technology using self-organization effects of low-dimensional nanostructures by growing crystals under different rate, annealing and thermal fluctuation conditions, as well as thermal diffusion intercalation.

To increase as much as possible the thermoelectric figure of merit of materials, the electron conductivity should be possible higher with the lowest thermal conductivity. The thermoelectric properties can be improved by using space inhomogeneous materials whose inhomogeneities are comparable in size to characteristic wavelengths of electrons (10 – 50 nm) or phonons (1 nm), i.e. lie in nanometer region. Thermal conductivity can be reduced considerably by thermal flux scattering on interfaces, and conditions should be selected so that interface could scatter phonons, rather than electrons. Description and calculation of the model of such quantum tunnelling transport is given in [1, 2].

Crystals were prepared by vertical directional crystallization method at a temperature gradient

$\Delta T = 100$ degrees/cm and crystallization rate 1; 2 and 2.5 cm/hour. AFM (atomic force microscope) images were obtained using Solver Next scanning probe microscope. *X*-ray diffractometer investigations of (0001) surface were performed on Philips Panalytical X'Pert Pro XRD diffractometer.

Nanoislands, nanowires, nanosteps and corrugated structures, dislocation centres play a decisive quantum-mechanical role in the localization and transfer of charge and heat. The choice of such high-performance substances should be based on the knowledge of structure-property interaction for $A_2^{V}B_3^{VI}$ compounds and their solid solutions with interlayer strictly oriented nanoparticles. Formation of these structures is due to mass transfer and plastic deformation whose nature and regularities are inherent in organization of similar structures in other solid-state materials.

As is known, in many layered crystals there is the effect of stoichiometric excess and impurity ejection from the layers that form crystal blocks to the interlayer van der Waals space. Such self-purification is called self-intercalation effect [3]. With certain impurities, this process can be accompanied by a change in electrical activity. Self-organization of nanostructures on the surface of interlayer space leads to formation of elements depending in their form on the composition and amount of impurity and the temperature conditions of diffusion and annealing. In this context, of interest are layered systems whose van der Waals spaces can serve as nanoreactors [4, 5, 6] for the formation of various nanofragments. Alignment of impurity clusters into quantum dot array on (0001) surface of crystal is interesting in terms of material properties control.

Discussion of the results

Supposed diffusion paths and their aggregation are related to the process of filling with impurities of places around the dislocation networks and vacant sites, such as telluride (selenium) vacancies on the van der Waals (0001) surface (Fig. 1). Due to active interaction in annealing, impurities are formed around these dislocation networks to form nanoobjects (Fig. 2), including interlayer nanostructured elements (INSE). Diffusion processes in the line of basal (0001) surface not only form individual nanostructured elements, but also connect them by a continuous chain, forming charge percolation channels along the direction of crystal growth.

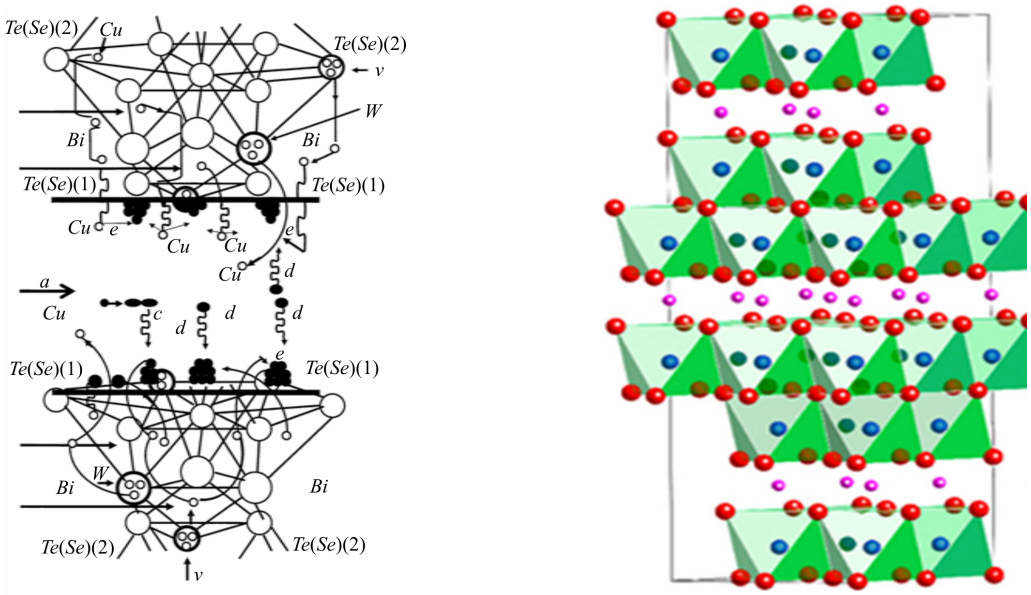

a) *b)*

Fig. 1. Schematic of INSE aggregation paths in Bi_2Te_3 doped (a) and intercalated (b) with copper.

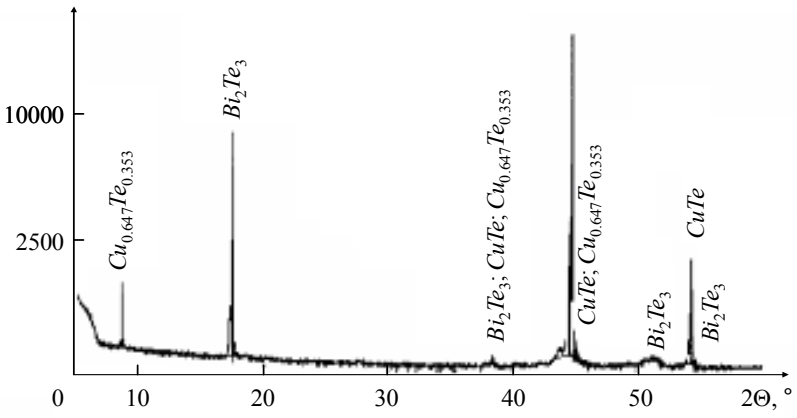
10000
2500
0
10
20
30
40
50
2Θ, °
$Cu_{0.647}Te_{0.353}$
Bi_2Te_3
Bi_2Te_3; CuTe; $Cu_{0.647}Te_{0.353}$
CuTe; $Cu_{0.647}Te_{0.353}$
Bi_2Te_3
CuTe
Bi_2Te_3

a)

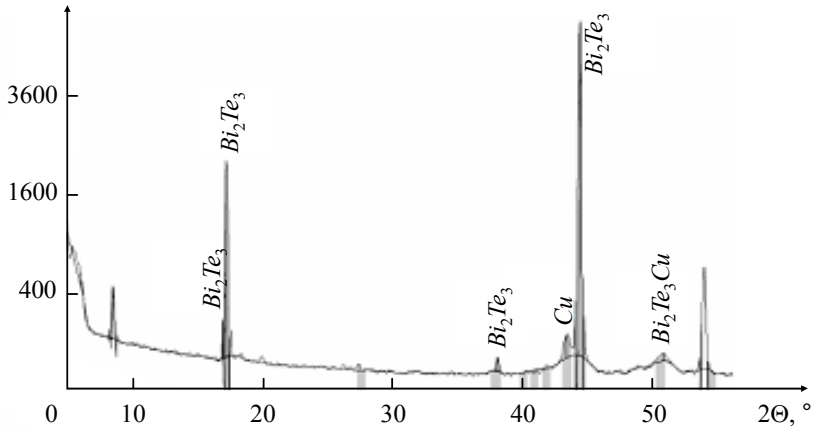
3600
1600
400
0
10
20
30
40
50
2Θ, °
Bi_2Te_3
Bi_2Te_3
Bi_2Te_3
Bi_2Te_3
Cu
Bi_2Te_3Cu

b)

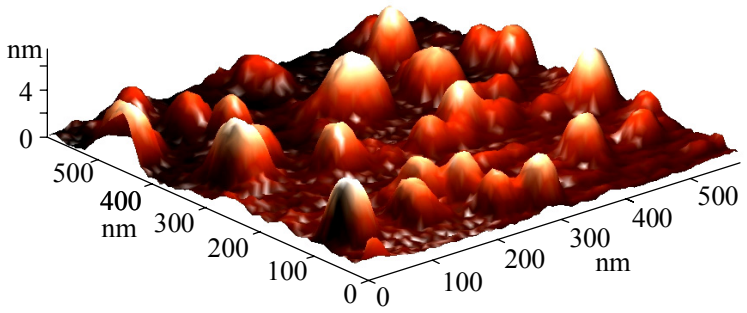
nm
4
0
500
400
nm
300
200
100
0
0
100
200
300
nm
400
500

c)

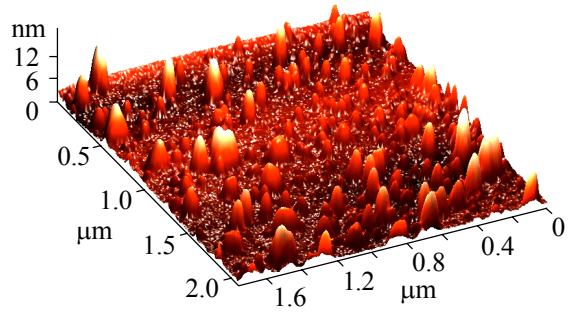
nm
12
6
0
0.5
1.0
μm
1.5
2.0
1.6
1.2
0.8
μm
0.4
0

d)

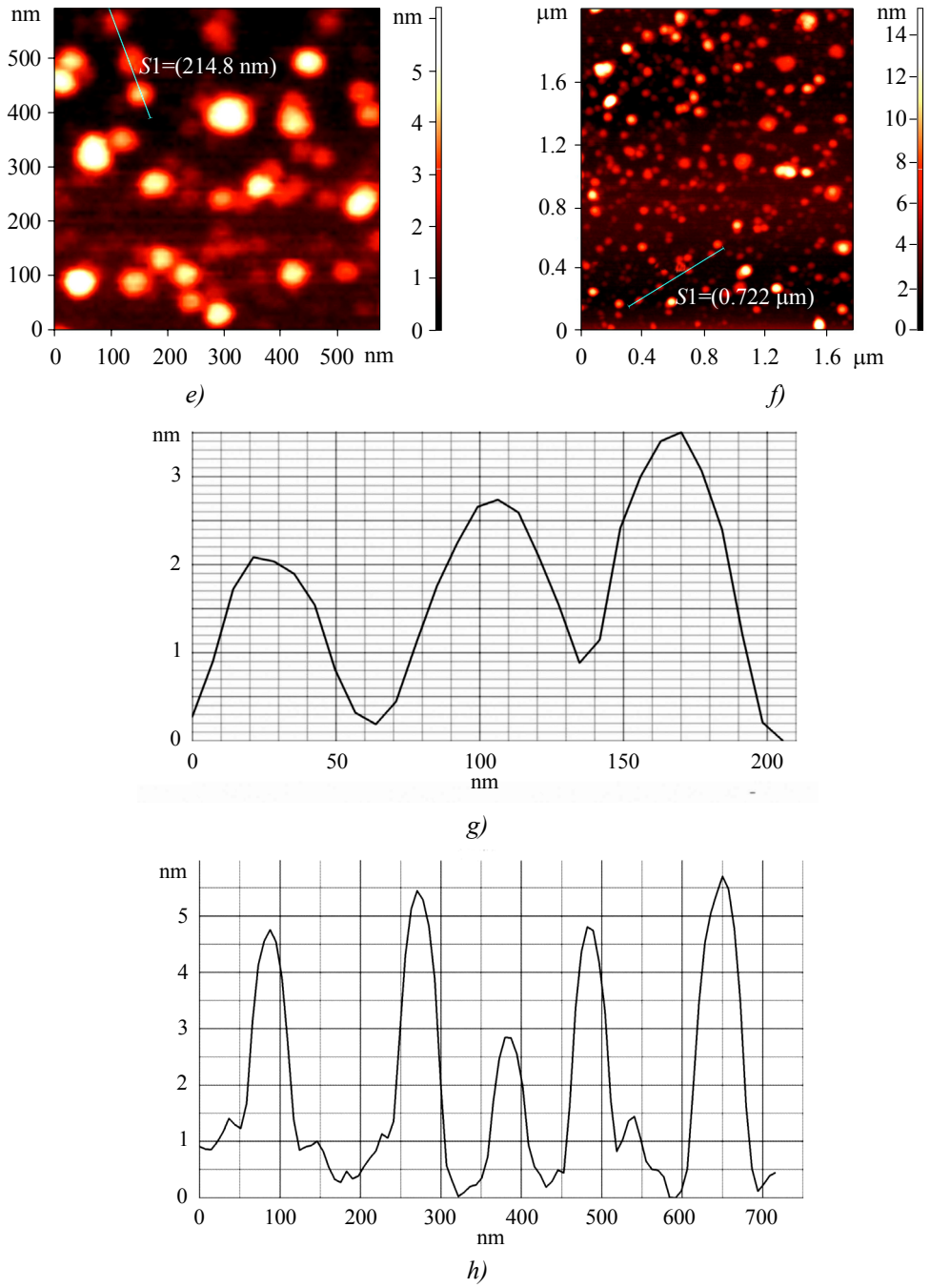

Fig. 2. X-ray diffractogram of copper doped Bi_2Te_3 – a); X-ray diffractogram of copper intercalated Bi_2Te_3 – b); 3D AFM image of Bi_2Te_3<Cu> – c); 3D AFM image of copper intercalated Bi_2Te_3 – d); 2D AFM image of Bi_2Te_3<Cu> – e); profilogram of doped Bi_2Te_3<Cu> – f); 2D AFM image of copper intercalated Bi_2Te_3 – g); profilogram of copper intercalated Bi_2Te_3 – h).

These structures by definition are quantum dot superlattices.

Quantum dots (nanoislands) and their distribution density should be considered as one of the factors determining percolation threshold on the lattice in (0001) $A_2^VB_3^{VI}$ <impurity> plane [7, 8]. In $Te^{(1)}$-$Te^{(1)}$ layer on the van der Waals surface having the greatest "gap" there are nanoisland arrays – some analogy of quantum dots. In this way infinitely connected structures are formed consisting of separate INSE and interconnected by a continuous chain; thus tunnelling current can flow along the conducting channels (bonds) through bonded INSE. With formation of superstructure in Bi_2Te_3 the

temperature dependences of kinetic properties can be of extreme kind [6]. Along the layers between the opposite lattice sides in $Te^{(1)}$-$Te^{(1)}$ space, charges can be transferred through nanoisland array affecting the general density of electric current. Percolation effect on (0001) Bi_2Te_3 surface which is either of the two sides of $Te^{(1)}$-$Te^{(1)}$ layers, influence of surface relief on percolation threshold leading to magnetoresistance oscillation and changes in kinetic parameters (Fig. 3) are of certain interest.

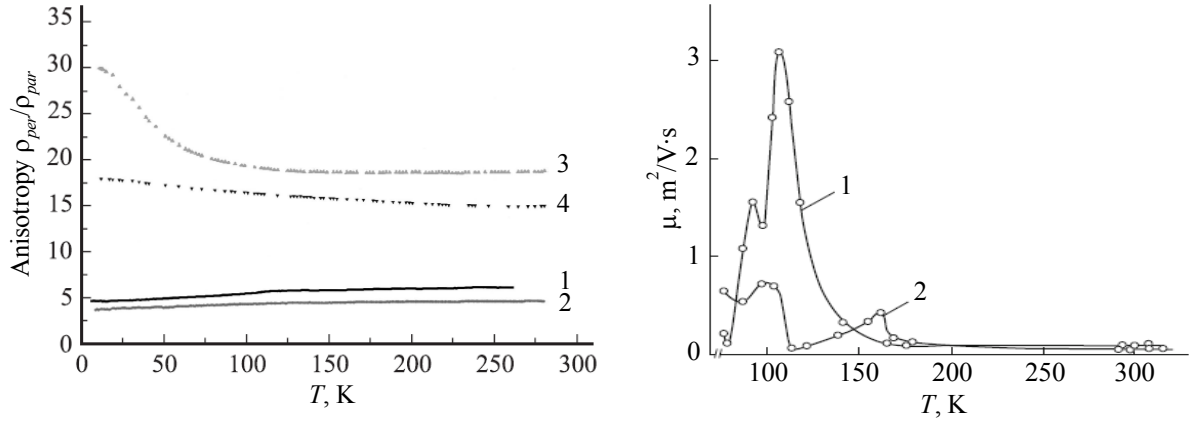

Fig. 3. Temperature dependences of resistivity anisotropy of Bi_2Te_3 single crystals in the temperature range of $5 < T < 300$ K: 1 – undoped Bi_2Te_3, 2 – Bi_2Te_3 (Cu), 3 – Bi_2Te_3 (Cu, In), 4 – Bi_2Te_3(B) – a); Temperature dependences of charge carrier mobility of Bi_2Te_3<Ni, 0.5 mas.%> at $H \perp c \perp I$ (1) and $H \parallel c \perp I$ (2) – b).

Percolation threshold is determined by the density of nanoislands distribution. The process of INSE aggregation and percolation in $Te^{(1)}$-$Te^{(1)}$ space is similar to the model of description of percolation cluster assembly on a free lattice (Fig. 4). This model assumes that a particle moving in space and touching a cluster will adhere to it with certain probability. In the simplest arrangement in a two-dimensional $Te^{(1)}$-$Te^{(1)}$ space it turns out that (0001) surface is considered as a square lattice (cell). Thus, each particle moves to the neighboring square randomly. If a particle reaches the boundary of $Te^{(1)}$, it is either reflected from it, or deposited in telluride vacancies and on dislocation walls. Being aggregated, the particle stops and is fixed in this lattice. Diffusion process, when continued, forms a two-dimensional surface cluster of percolation type, extending along (0001) basal plane. During certain stages INSE grow normal to (0001) plane, which is clearly seen from 3D AFM images (Figs. 5, 7). The process of coagulation in $Te^{(1)}$-$Te^{(1)}$ space reaches a maximum whereby contacting INSE are united into a single fractal surface above the percolation threshold.

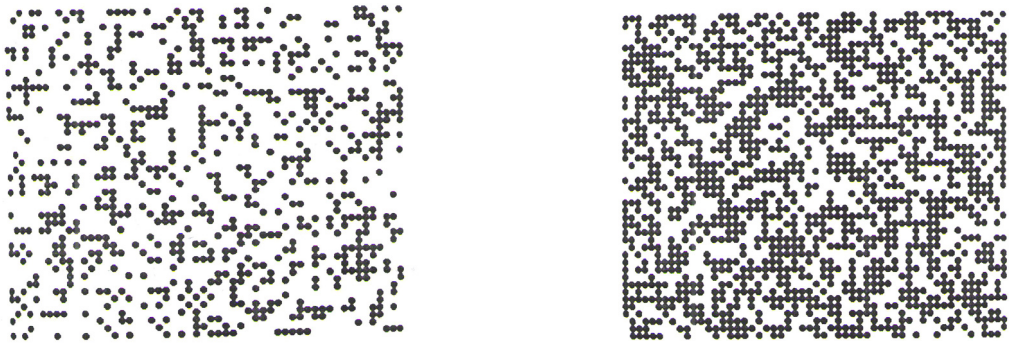

Fig. 4. Simulated square lattices with random sites for comparison to AFM images of the (0001) surface of crystals: a) Square lattice with randomly occupied sites below the percolation threshold; b) Square lattice with site occupancy probability equal to percolation threshold.

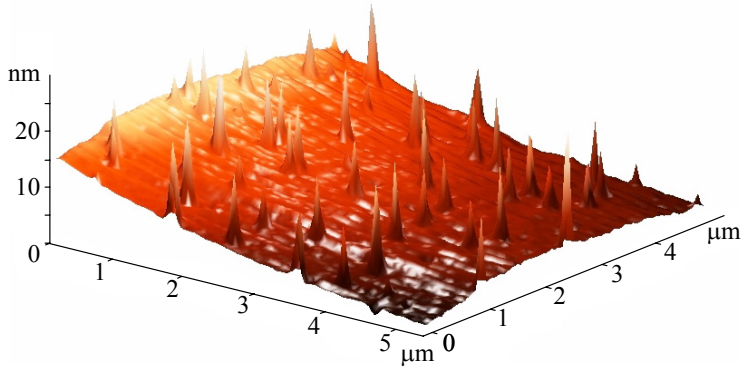

a)

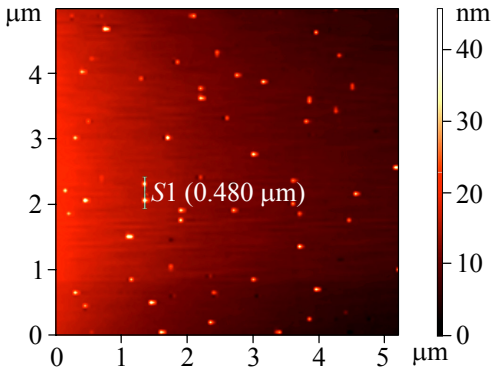

b)

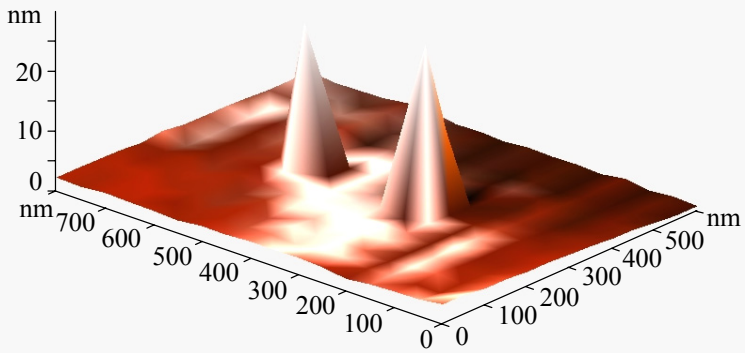

c)

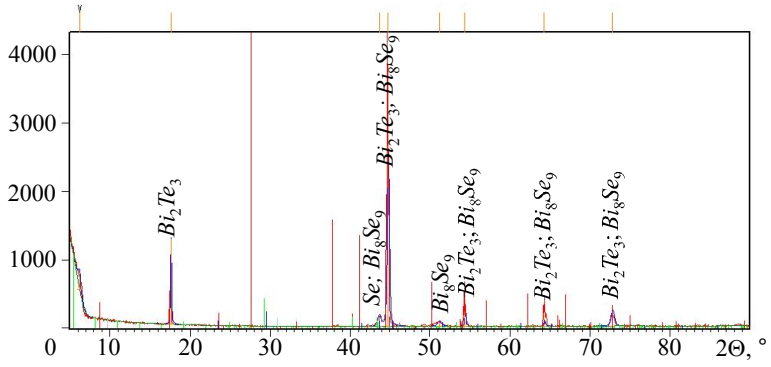

d)

Fig. 5. 3D AFM image of doped Bi_2Te_3<Se> – a); 2D AFM image of Bi_2Te_3<Se> – b); 3D AFM image of a fragment of two nanoislands of Bi_2Te_3-Se – c); X-ray diffractogram of Bi_2Te_3<Se> with Se traces at 2θ = 44° – d).

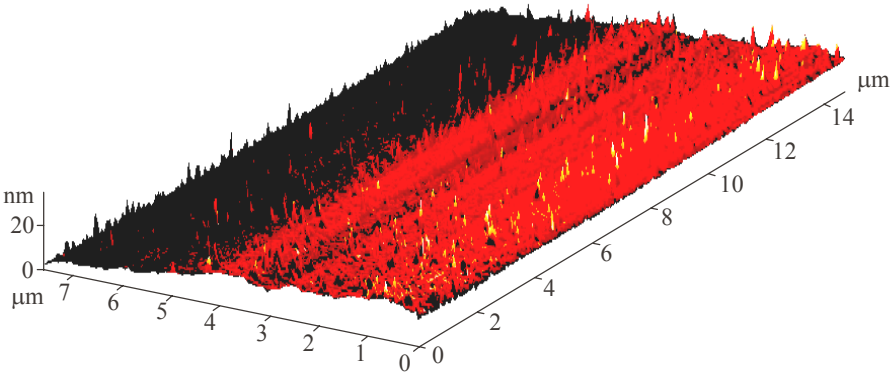
nm
20
0
μm
7
6
5
4
3
2
1
0
0
2
4
6
8
10
12
14
μm

a)

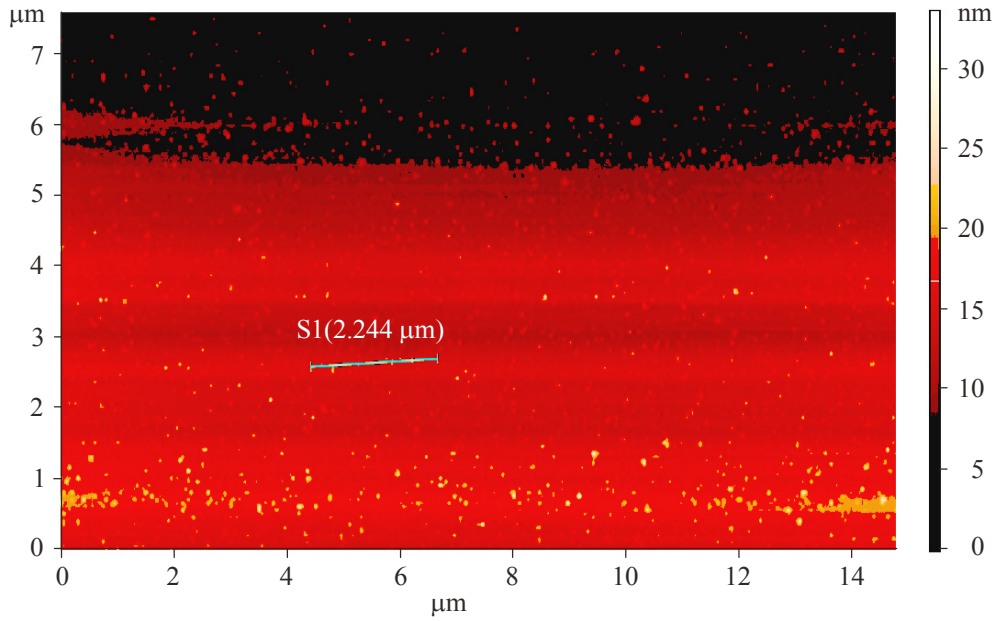
μm
7
6
5
4
3
2
1
0
S1(2.244 μm)
0
2
4
6
8
10
12
14
μm
nm
30
25
20
15
10
5
0

b)

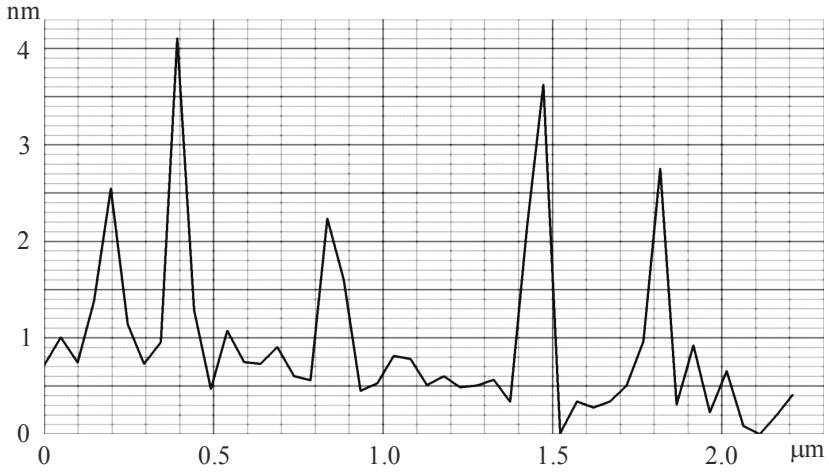
nm
4
3
2
1
0
0
0.5
1.0
1.5
2.0
μm

c)

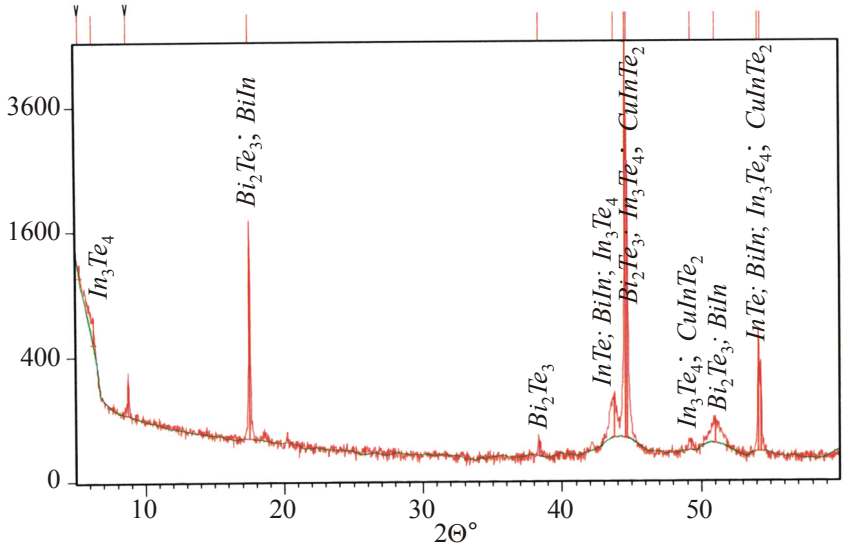

d)

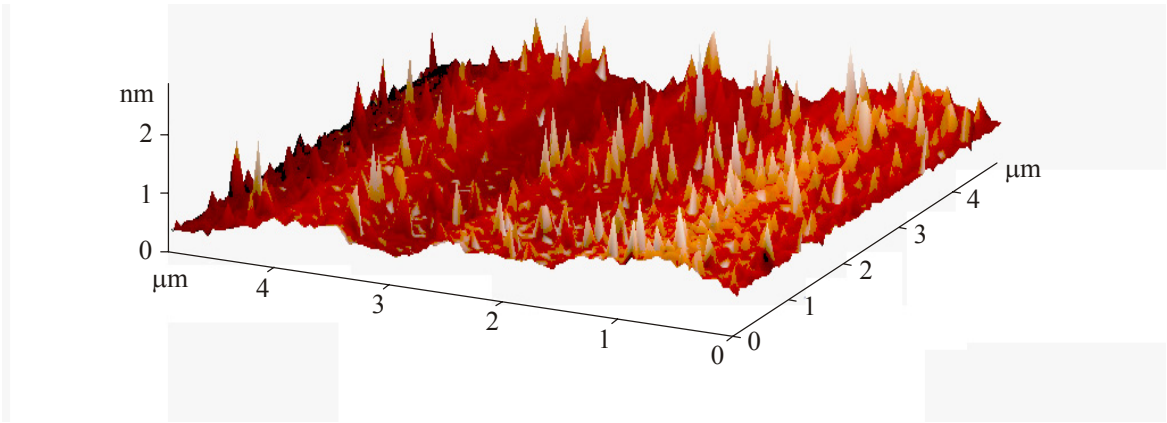

e)

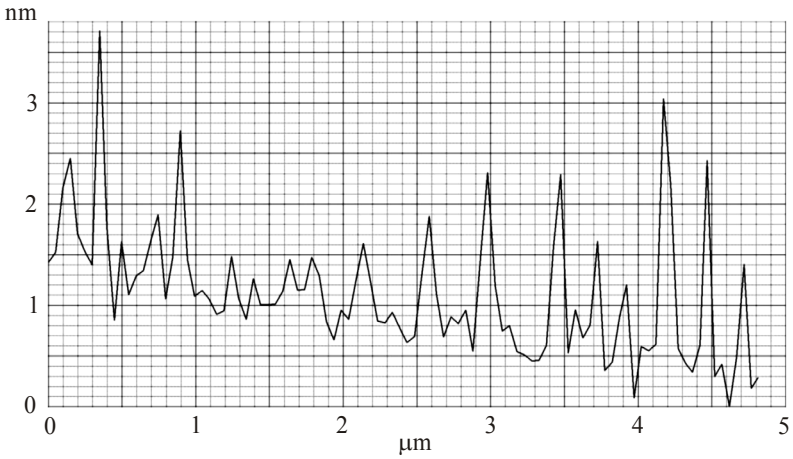

f)

Fig. 6. 3D AFM image in Bi_2Te_3<In+Cu> system – a); 2D AFM image in Bi_2Te_3<In+Cu> system – b); profilogram along the section given in Figs. b), c); X-ray diffractogram of Bi_2Te_3<In+Cu> – d); fragment of 3D AFM image of Bi_2Te_3<In+Cu> – e); profilogram of Bi_2Te_3<In+Cu>fragment – f).

Materials with interlayer nanostructures are quantum dot (QD) superlattices consisting of impurity clusters several nanometers in size. If QD density is above the respective percolation threshold, conductivity in them takes place in single-dimensional channels by diffuisonal mechanism. Below the percolation threshold nanostructures possess hopping conductivity due to tunnelling of electrons through the barriers dividing QD. Transition from hopping to diffusion transport is observed with a change in QD density and the degree of their filling with charge carriers.

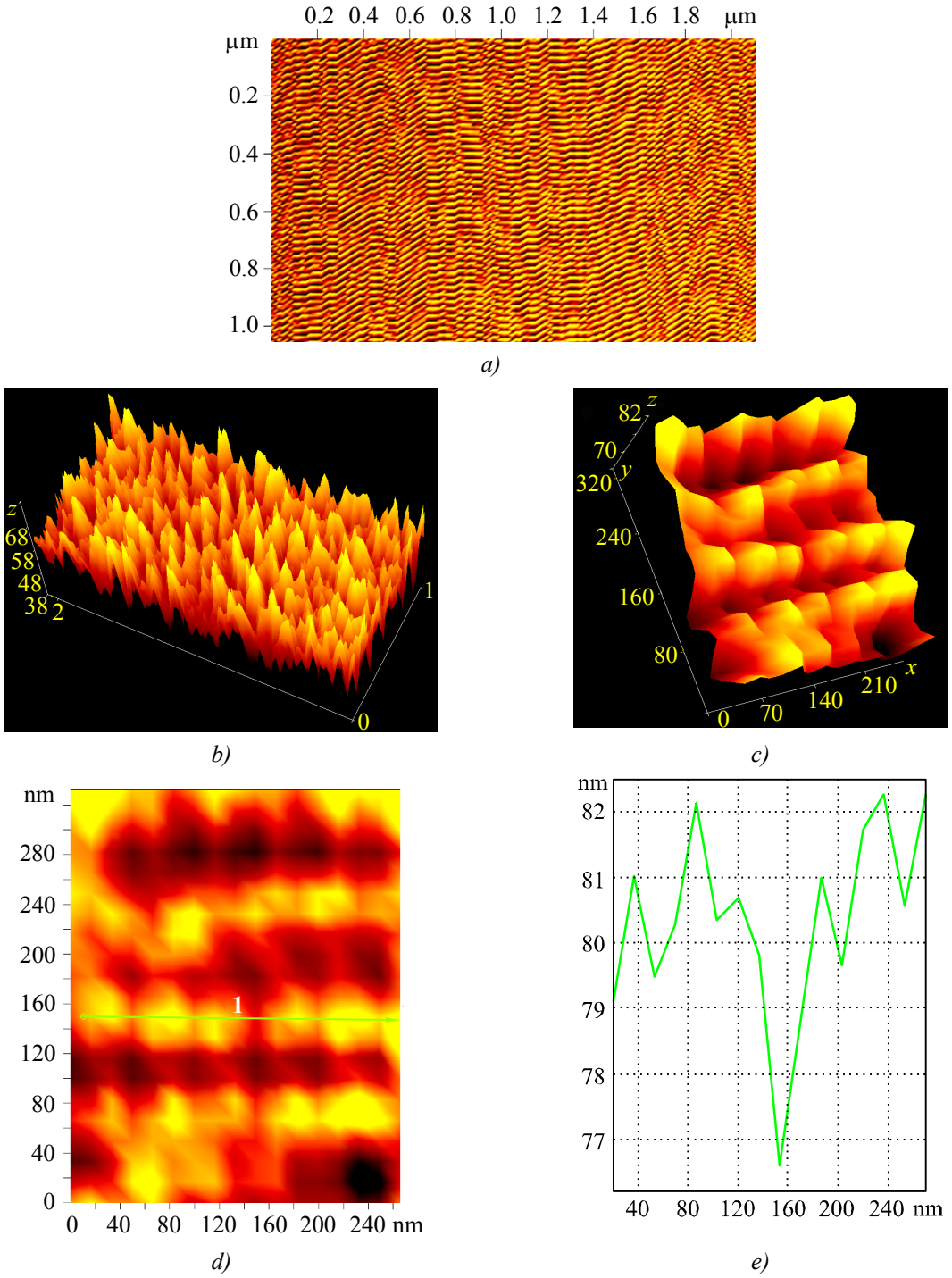

Fig. 7. 2D AFM image of Bi_2Te_3<Ag> – a); 3D AFM image of Bi_2Te_3<Ag> – b); 3D AFM image of Bi_2Te_3<Ag> – c); fragment of 2D image of Bi_2Te_3<Ag> – d); profilogram along the (1)line (see Fig. d) – e).

The main reason for stressed islands formation on the surface is relaxation of elastic stresses on the edges of layers and interaction of islands through stresses they create in the crystal. The shape of QD can vary considerably in the course of healing or postgrowth annealing. Fig. 8 demonstrates the final result of the dynamics of large islands formation from small ones and linear formations formed of QD that can be called quantum wires. The aggregated structures interconnected by a continuous chain of clusters assure charge tunnelling in conducting channels.

Electron microscopic images have shown that nanoobjects are formed of nanoislands in diffusion at temperatures above 500 K. Penetrating mainly into the interlayer space, impurities create bulk periodic superstructures consisting of nanoisland arrays between quintet layers which move apart as a result and increase crystal anisotropy. This, in turn, increases the role of "bending" vibrations for crystal thermal properties. The role of this specific branch of acoustic vibrations and its behaviour in layered crystals according to Lifshits theory [9] was reported in [10]. The "bending" branch corresponds to vibrations propagating in layers plane with shifting of atoms in the direction normal to layers and makes the main contribution to heat transfer with the temperature behaviour of three different types. The higher is crystal anisotropy, the more significant is its role in "membrane" effect (growth of "bending" vibration frequency under tension of layers), leading to negative dilatation in layers plane. The anomalies of kinetic parameters that we observed took place in the area of linear temperature growth of heat capacity, with the dominant contribution of "bending" branch. Scattering of this phonon branch at the base of QD that are chemically related to quintets, results in thermalization of QD levels with subsequent tunnelling. This area, where heat capacity $C \sim T^2$, and temperature growth of thermal conductivity coefficient $\chi \sim T^{2+X}$ (where x can be determined by tunnelling processes, i.e. by QD size and density) is observed as the area of thermal anomaly. Note that a drop in lattice thermal conductivity in this area can be somewhat compensated by increased thermal conductivity of tunnelling current. Thermoelectric figure of merit of these samples is 15 % higher than that of undoped ones, probably due to a reduction of total thermal conductivity of "quintet layers-INSE" composite with increased role of phonon scattering on the boundaries of moved apart layers and INSE. These processes are dominated by phonons corresponding to bending vibrations that have a square type of dispersion.

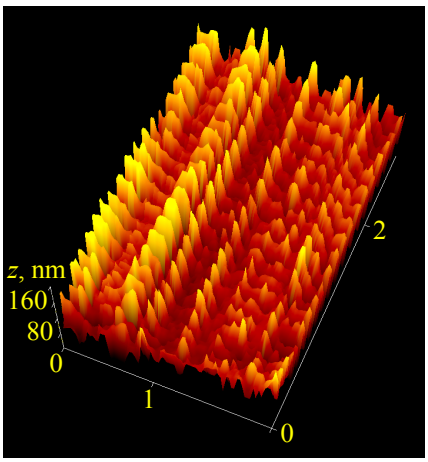

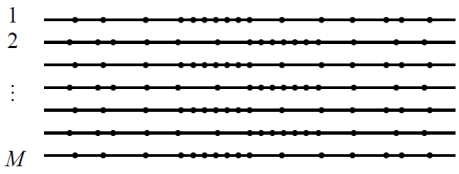

Plurality of parallel channels with fluctuations of impurity amount. The admittance of 1D channels can be determined by several high conducting of them.

Fig. 8. Ni-doped Bi_2Te_3: 3D AFM image of Bi_2Te_3<In + Cu> with parallel conductivity channels.

Anharmonic vibrations of structure-forming atoms of layers are one of the factors yielding a relatively uniform linear crystal growth. With increase in elastic stress pressure created by thermal

wave, the linear order of alignment is violated and quintet layers are deformed with a periodic distribution of wrinkles (Fig. 9, 10).

The value of thermal pulse forms an elastic deformation, and when some critical compressive stress is over the limits, quintet layers are aligned in corrugated wavy structures, which attenuates compressive stress. This occurs with increase in the rate of crystal growth by a factor of 2 and 2.5. The wavelength of wrinkles is determined by elastic characteristics and the thickness of quintet layers. The method of calculation of deformed layer thickness versus the wave period [11] can help to determine the number of quintet layers in a corrugated structure. A change in the average "wavelength" λ corresponding to the wrinkles was described by a simple power dependence $\lambda(x) \sim x^m$. The investigated materials differed in the value m. In order to describe their properties correctly, physicists introduced a concept of wrinklon, i.e. structural element whose recurrence characterizes the entire ensemble of wrinkles. A single wrinklon is responsible for a transition area where two wrinkles with the "wavelength" λ are combined to form a larger one. Each wrinklon in this case is matched by certain size L determined by material characteristics and the value of λ.

In this case one can use the expression of the form $\lambda(x)/h \sim (E \cdot h/T)^{0.25} \cdot (x/h)^{0.5}$, where h is layer thickness, E is Young's modulus, and T value characterizes the tensile force.

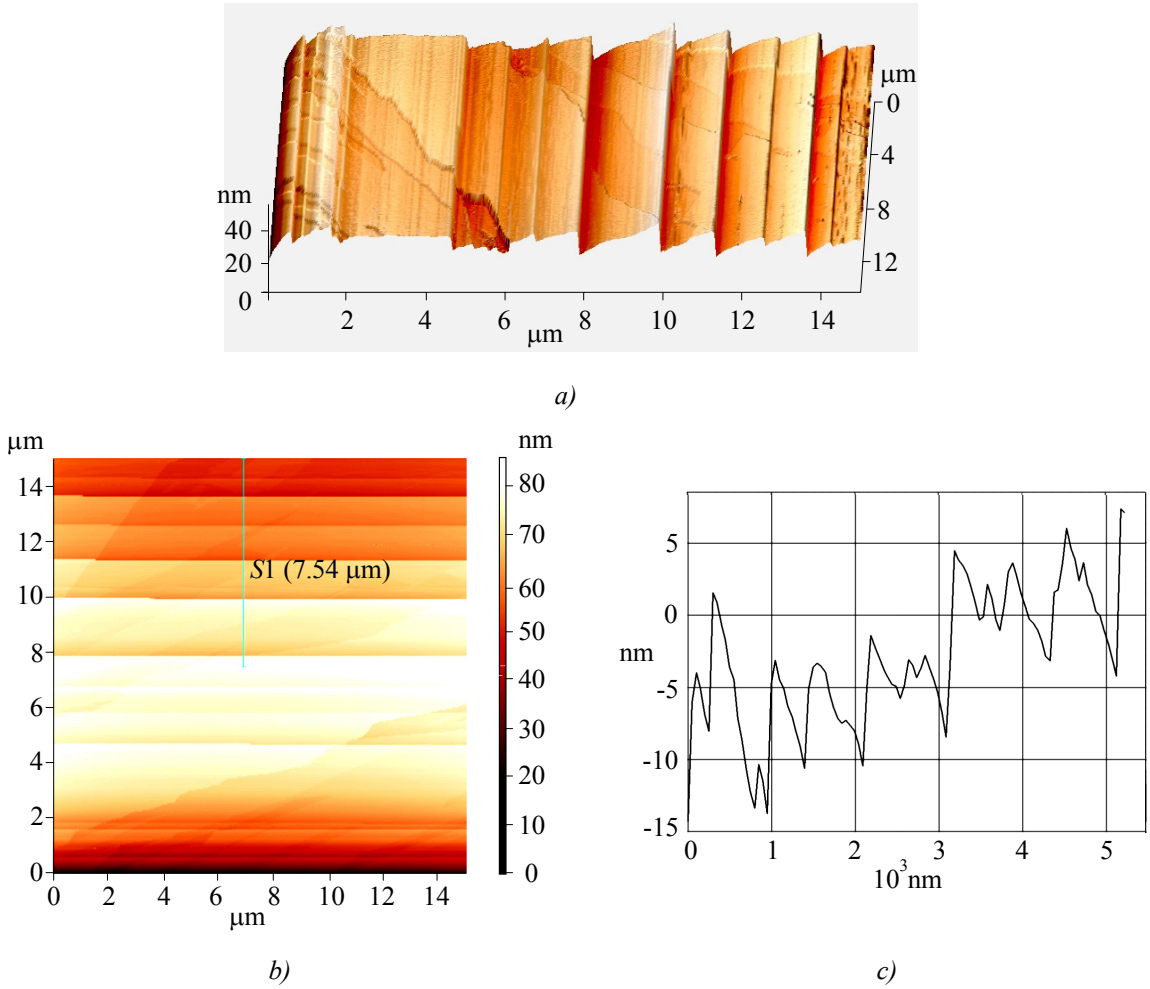

Fig. 9. Corrugated structures Bi_2Te_3<Ni>: 3D AFM image of surface – a); 2D surface – b); cut profilogram in Fig. b) – c).

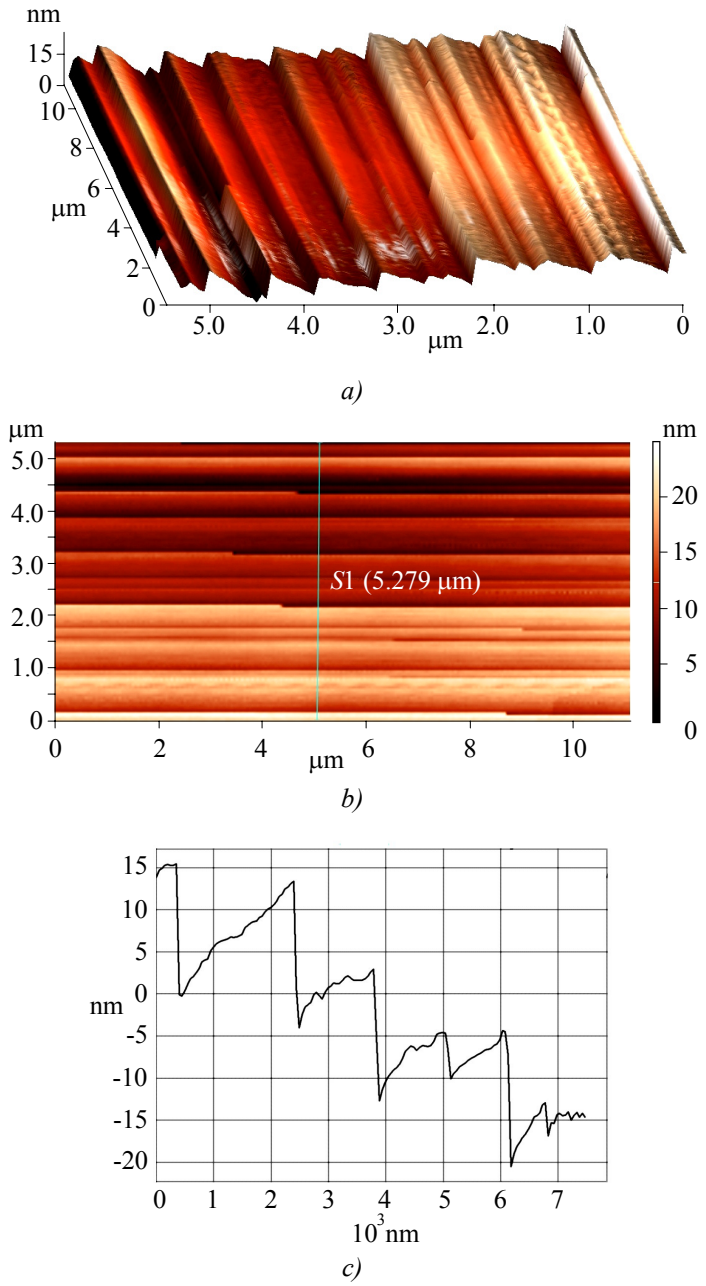

Fig. 10. Corrugated structures Bi_2Te_3<Se>: 3D AFM image of surface – a); 2D surface – b); cut profilogram in Fig. b – c).

Obtaining the right size wrinkles is directly related to crystallization front temperature. Its rise leads to increased viscosity of crystallized area and reduced ability of elastic energy accumulation, owing to which the height of the structure is reduced. Thus, the wavelength of wrinkle and its height correlate in a very small range with crystallization front temperature.

It should be noted that the results obtained are in agreement with the authors' theoretical research [12-14].

Conclusions

Materials with nanoisland arrays, corrugated and stepped structures-nanowires of different size and density have been obtained. A mechanism of formation of the above nanostructures has been

described, which is due to migration, coalescence and clustering of nanoislands in the interlayer space of undissolved impurity and superstoichiometric excess, as well as due to plastic deformation effect under a pressure of thermal wave forming corrugated structures. Single-dimensional charge flow channels have been discovered, the percolation character of charge carrier transport in the network with respective quantum dot distribution density has been determined.

References

1. A.A. Snarskii, A.K. Sarychev, I.V. Bezsudnov, and A.N. Lagarkov, Thermoelectric Figure of Merit of the Bulk Nanostructured Composites with Distributed Parameters, *Semiconductors* **46** (5), 677 – 683 (2012).
2. L.P. Bulat, D.A. Pshenai-Severin, Effect of Tunneling on the Thermoelectric Figure of Merit of Bulk Nanostructured Materials, *Physics of the Solid State* **52** (3), 452 – 458 (2010).
3. S.Sh. Kakhramanov, Selfintercalation in Bi_2Te_3<*Cu*>, *Inorganic Materials* **44** (1), 17 – 25 (2008).
4. F.K. Aleskerov, S.Sh. Kakhramanov, Effect of Interlayer Metal Nanofragments on the Kinetic Properties of Bi_2Te_3<*Cu, Ni*>, *Metallofizika i Noveishie Tekhnologii* **30** (11), 1465 – 1477 (2008).
5. F.K. Aleskerov, S.B. Bagirov, S.Sh. Kakhramanov, and G. Kavei, Thermoelements for Electric Generators Based on Bismiuth and Antimony Chalcogenides with Interlayer Nanostructures, *Transactions of Azerbaijan National Academy of Sciences: Series of Physical-Mathematical and Technical Sciences, Physics and Astronomy* **5**, 52 – 55(2010)
6. B.M. Goltsman, V.A. Kudinov, and I.A. Smirnov, *Semiconductor Thermoelectric Materials Based on Bi_2Te_3* (M: Nauka, 1972), 319 p.
7. F.K. Aleskerov, K.Sh. Kakhramanov, and S.Sh. Kakhramanov, Percolation Effect in Bi_2Te_3 Crystals Doped with Copper or Nickel, *Inorganic Materials* **48** (5), 41 – 45 (2012).
8. F.K. Aleskerov, K.Sh. Kakhramanov, and S.Sh. Kakhramanov, Percolation Process in Bi_2Te_3-In_2Se_3 System, Transactions of Azerbaijan National Academy of Sciences: Series of Physical-Mathematical and Technical Sciences, *Physics and Astronomy* **2**, 25 – 33 (2010).
9. I.M. Lifshits, On the Thermal Properties of Chain and Layered Structures at Low Temperatures, *JETP* **22** (4),475 – 486 (1952)
10. N.A. Abdullayev, R.A. Suleymanov, M.A. Aldzhanov, and L.N. Alieva, On the Role of Bending Vibrations in Heat Transfer Processes in Layered Crystals, *Physics of the Solid State* **48** (4), 1775 – 1779 (2002).
11. H. Vandeparre, M. Pineirua, F. Brau, B. Roman, J. Bico, C. Gay, W. Bao, C.N. Lau, P.M. Reis, and P. Damman, Wrinkling Hierarchy in Constrained Thin Sheets from Suspended Graphene to Curtains, *Phys. Rev. Lett*. **106**, 224301 (2011), issue 22 / (arXiv:1012.4325v2 (2010).
12. K.Sh. Kakhramanov, A.M. Pashayev, B.G. Tagiyev, F.K. Aleskerov, and A.A. Safarzade, Nano-structured Hybrid Structured Based on $A_2^VB_3^{VI}$<impurity>, *J. Thermoelectricity* **2**, 32 – 41 (2011).
13. E.I. Rogacheva, Percolation Effects and Thermoelectric Material Science, *J. Thermoelectricity* **2**, 61 – 72 (2007).
14. L.P. Bulat, V.T. Bublik, I.A. Drabkin, V.L. Karatayev, V.B. Osvensky, G.I. Pivovarov, and D.A. Pshenai-Severin, Bulk Nanostructured Thermoelectrics Based on Bismuth Telluride, *J. Thermoelectricity* **3**,67 – 72 (2009).

Submitted 20.02.2013.

L.I. Anatychuk, Yu.N. Mochenyuk, A.V. Prybyla

Institute of Thermoelectricity NAS and MES of Ukraine,
1, Nauky Str., Chernivtsi, 58029, Ukraine

SOLAR THERMOELECTRIC ENERGY CONVERTERS

Results of computer design of a solar thermoelectric generator with a solar energy concentrator whose walls serve for rejection of heat from the hot junctions of a thermoelectric energy converter have been presented. With the aid of object-oriented computer simulation the distributions of electric potential and temperature in a thermoelectric generator with regard to temperature dependences of the kinetic coefficients of materials, as well as contact resistances have been obtained. Design calculation of a thermoelectric converter has been made assuring optimal mode of solar into electric energy conversion which yielded the generator efficiency of 4.67 %. The cost of electric energy power generated by such a converter is 0.5 $/W, which makes it competitive in the market of solar energy converters.

Key words: solar energy, thermoelectric generator, computer simulation.

Introduction

General characterization of the problem. Creation of alternative renewable power sources is one of the most relevant issues today, since it contributes to solving the ecological problems of thermal contamination of the Earth leading to change of its climate.

The Sun is the largest source of renewable energy on the Earth. Its radiated power is $4 \cdot 10^{23}$ kW of energy, of which about 10^{14} kW of power falls on the Earth. In so doing, 1 m^2 of the area perpendicular to solar rays receives as little as about 1 kW of energy [1]. Such solar radiation density is insufficient to provide the necessary temperature differences in thermoelectric power converters. In this case it is reasonable to use special solar concentrators in the form of paraboloids, Fresnel reflectors or a combination of plane mirrors [1]. Thermoelectric converters are characterized by long service life and high reliability which makes promising their use in combination with solar concentrators [2, 3].

Analysis of the literature. The first solar thermoelectric generators (STEG) were made by the close of the XIX century. Among them, a generator developed by Russian astronomer V.K. Tserasky that activated the electric bell [1].

In the 1950s, due to the advent of novel material for thermocouples (*p-Zn-Sb*, *n-Bi-Sb*), interest in the possibility of direct solar radiation into electric energy conversion was rekindled [1, 4, 5]. Using a flat-plate collector in the form of a blackened copper plate as a concentrator of thermal energy yielded the generator efficiency about 1.05 % [4]. The generator with an optical concentrator that focused solar radiation on thermocouple hot junctions achieved the efficiency of 3.35 % [4]. Modern developments of solar thermoelectric generators [6-11] have been made both with and without optical concentrators of solar energy. Thus, paper [6] describes theoretical and experimental investigations of STEG with a plane concentrator of thermal energy. The authors assert that they have succeeded to achieve the generator efficiency of 4.6 %.

The purpose of this work is computer design of a solar thermoelectric generator with a solar

energy concentrator whose walls simultaneously serve to reject heat from the hot junctions of thermoelectric energy converter, to achieve maximum efficiency and minimum cost of thermoelectric energy conversion which will make STEG competitive in the market of solar energy converters.

Physical, mathematical and computer models of STEG

The operating efficiency of a thermoelectric generator is determined as the efficiency of thermoelectric modules, as well as the efficiency of solar radiation into thermal energy conversion. Design optimization of STEG in this case consisted in maximum decrease of thermal losses and creation of temperature conditions for the realization of maximum efficiency of a thermoelectric converter [1].

Solar thermoelectric generator has three main components which are a solar radiation to thermal energy converter, a thermoelectric converter and a heat rejection device [1].

A paraboloid with a specular surface was used as a radiation concentrator. The receiving surface of the generator is a cut ball-shaped connecting conductor of the thermoelectric converter hot junctions (Fig. 1). The thermocouple cold junctions are in thermal contact with a paraboloid which is simultaneously the cold heat exchanger. For protection from atmospheric influence the paraboloid internal part is insulated with protective glass [12].

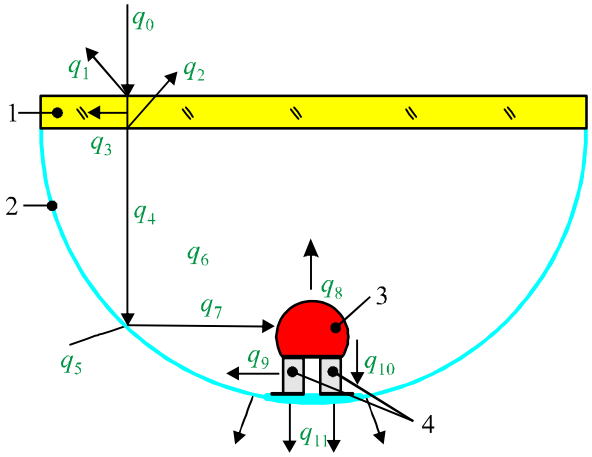

Fig. 1. Physical model of STEG. 1 – protective glass, 2 – solar parabolic concentrator, 3 – thermoelectric converter interconnects, 4 – thermoelectric energy converter.

The operating principle of STEG is as follows. Solar radiation passes through the glass protective surface 1, gets to the specular surface of parabolic concentrator 2, is reflected and focused on the interconnects 3, where it is converted into thermal energy. Part of the heat that passes through thermoelectric converter 4 is converted into electric energy. Heat from the cold thermocouple junctions is dissipated on parabolic concentrator 2 which also serves as the cold heat exchanger.

In Fig. 1 q_0 is the solar radiation flux that gets onto the protective glass, q_1 is the radiation reflected from the external glass surface, q_2 is radiation reflected from the internal glass surface, q_3 is radiation absorbed by the glass, q_4 is radiation that passed through the glass, q_5 is heat absorbed by the concentrator, q_6 is the heat lost on the concentrator internal side due to free convection and radiation, q_7 is the radiation focused on the interconnects of the hot junctions, q_8 is the heat losses on the receiving surface, q_9 is the heat losses due to convection and radiation on the lateral surface of thermocouple, q_{10} is the heat flowing through the thermocouple, q_{11} is the heat flux rejected from the concentrator surface due to free convection and radiation.

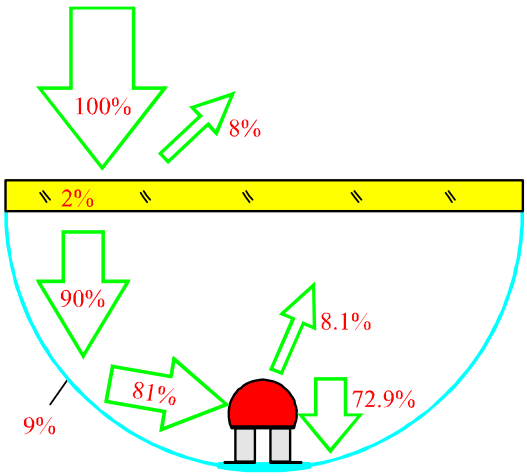

Fig. 2. Energy losses on the structural elements of STEG.

Theoretical calculations have shown that solar energy losses on STEG structural elements are as follows:

- 8 % of energy is reflected from the glass surface;
- 2 % is absorbed by the glass;
- 9 % is absorbed by the aluminum concentrator;
- 8.1 % is reflected from the thermocouple element receiving surface;
- 72.9 % of energy passes through the thermocouple legs.

For simplification of the problem the fluxes $q_1 - q_3$ were not taken into account. For the calculations we employed known transmission characteristics of the glass without account of absorbed heat q_3 spent for its heating up. It was also assumed that the volume restricting the protective glass and the mirror was filled with air.

To find temperature distribution in STEG, one should solve the thermal conductivity equation

$$q = \nabla(-\kappa \cdot \nabla T), \tag{1}$$

where κ is the thermal conductivity, ∇T is the temperature gradient and q is the heat flux.

The boundary conditions:

– on the concentrator specular surface :

$$q = \varepsilon_1 \cdot q_4 - \alpha \cdot \Delta T_1 + \varepsilon_1 \cdot \left(G_1 - \sigma \cdot T_1^4\right), \tag{2}$$

where ε_1 is the emissivity factor of the concentrator internal side, α is the heat exchange coefficient, ΔT_1 is the temperature difference between the concentrator internal side and the environment, σ is the Boltzmann constant, T_1 is the temperature of the concentrator internal side.

– on the receiving surface:

$$q = q_7 \cdot \left(2 \cdot \varepsilon_2 - 1\right) - \alpha \cdot \Delta T_2 + \varepsilon_2 \cdot \left(G_2 - \sigma \cdot T_2^4\right), \tag{3}$$

where ΔT_2 is the temperature difference between the receiving surface and the environment, T_2 is the receiving surface temperature, ε_2 is the emissivity factor of the receiving surface.

– on the boundaries of thermal contact between the interconnects and thermocouple legs

$$q = \kappa \cdot \frac{\Delta T_4}{l}, \tag{4}$$

where κ, l is the thermal conductivity and height of thermocouple legs, ΔT_4 is the temperature difference between the hot and cold thermocouple junctions.

– on the boundaries of lateral surfaces of thermocouple legs and the environment

$$q = \alpha \cdot \Delta T_3 + \varepsilon_3 \cdot \sigma \cdot \left(G_3 - \sigma \cdot T_3^4 \right), \tag{5}$$

where ΔT_3 is the temperature difference between the lateral surface of thermocouple and the environment, T_3 is the temperature of thermocouple lateral surface, ε_3 is the emissivity factor of thermocouple lateral surface.

– on the concentrator external surface

$$q = \alpha \cdot \Delta T_5 + \varepsilon_4 \cdot \sigma \cdot \left(T_5^4 - T_0^4 \right) \tag{6}$$

where Δ_{T5} is the temperature difference between the concentrator external side and the environment, ε_4 is the concentrator emissivity factor, T_5 is the concentrator temperature, T_0 is the ambient temperature, G is the incoming radiation heat flux for each separate boundary

$$G = G_m + F_{amb} \sigma T_{amb}^4, \tag{7}$$

where G_m is the radiation value from other boundaries of structural elements, F_{amb} is the field of vision factor equal to field of vision part which is not subject to other surfaces, T_{amb} is the temperature at a distant point in the directions included to F_{amb}.

Finding a solution for Eq. (1) with the boundary conditions (2 – 6) is a complicated problem whose analytical solutions are too awkward and not subject to analysis [13].

This problem was solved with the use of Comsol Multiphysics computer program of object-oriented simulation [14]. Computer model of solar thermoelectric generator created with its help permitted calculation of its physical fields, determination of major energy characteristics and optimization of STEG design.

Computer model of STEG (Fig. 1) consists of an aluminum parabolic concentrator (mirror) 2, a blackened copper receiving pad 3 shaped as a cut ball, and a thermocouple 4. The thermocouple cold junctions are in thermal contact to the parabolic concentrator which forms the cold heat exchanger.

Computer simulation was performed with the following initial conditions: solar radiation density is 1000 W/m^2, ambient temperature is 300 K. Rejection of heat from the cold heat exchanger was done by free convection and radiation to the environment. In conformity with the real physical and optical properties [15, 16] of solar thermoelectric generator structural elements, the following values of absorption and reflection factors were taken, namely: transmission factor of the glass is 0.9, reflection factor of the aluminium mirror is 0.9, emissivity factor of the receiving pad ε_2 and the external side of the parabolic concentrator ε_4 is 0.9, emissivity factor of the lateral surface of thermocouple legs ε_3 and the concentrator internal surface ε_1 is 0.1. Standard Bi_2Te_3 based thermoelectric material was used (Fig. 3) [17, 18]. Design optimization of STEG was made with respect to the parabolic concentrator diameter D, the concentrator thickness d and the thermocouple thermal resistance. The initial value of D was selected as 20 mm, as long as exactly with this diameter the focus remained under the protective glass. The concentrator diameter D was increased so that the paraboloid focus remained unvaried. The initial value of the concentrator thickness d = 0.2 mm.

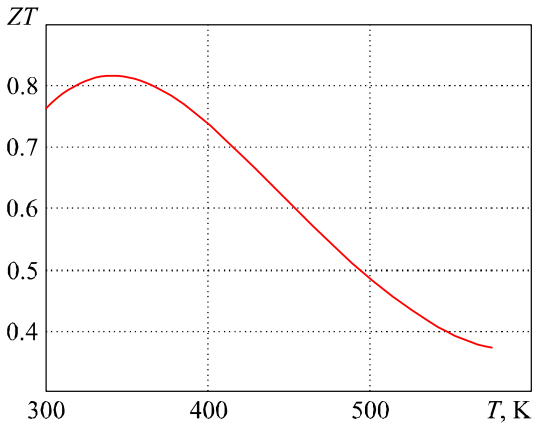

Fig. 3. ZT of Bi_2Te_3 based thermoelectric material.

For each design variant the cross-section area (thermal resistance) of thermocouple legs was optimized so as to assure the hot temperature 300 °C, as long as exactly at this temperature the maximum efficiency for selected thermoelectric material is achieved.

Optimization results

Computer simulation has resulted in the values of temperature on the cold thermocouple junctions of STEG (Fig. 4), the temperature distributions on the cold heat exchanger (Fig. 5), as well as the values of EMF and electric power. The efficiency values of the solar thermoelectric generator have been calculated for different paraboloid diameters and thicknesses (Fig. 6). It has been established that STEG efficiency reaches 4.65 %. Also, the effect of contact electric resistances has been studied that results in reduction of STEG energy characteristics by 8 %.

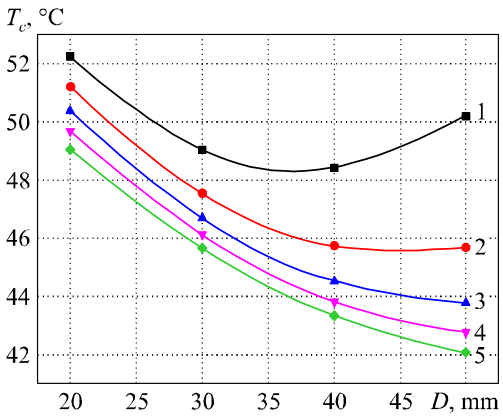

Fig. 4. Plot of thermocouple cold temperature T_c versus the concentrator diameter for its different thicknesses d. 1 – d = 0.2 mm; 2 – d = 0.4 mm; 3 – d = 0.6 mm; 4 – d = 0.8 mm; 5 – d = 1 mm.

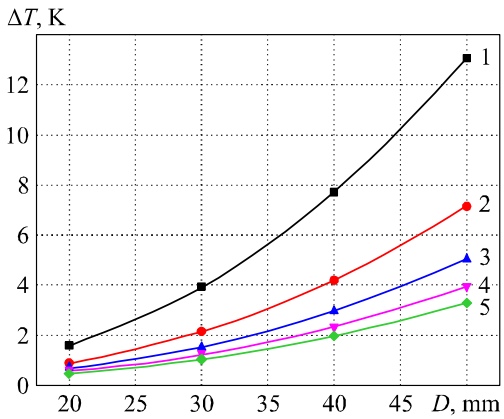

Fig. 5. Plot of ΔT between the centre and edge of the aluminum concentrator versus its diameter for different concentrator thicknesses d. 1 – d = 0.2 mm; 2 – d = 0.4 mm; 3 – d = 0.6 mm; 4 – d = 0.8 mm; 5 – d = 1 mm.

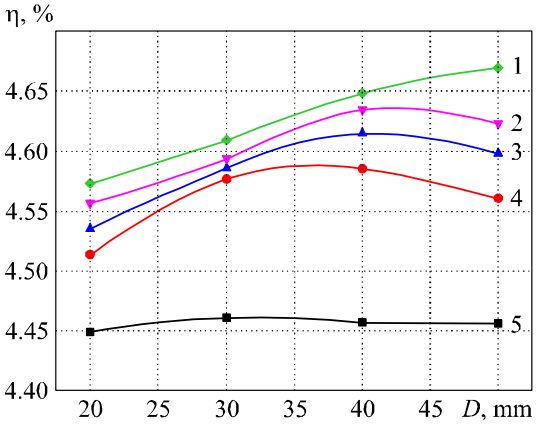

Fig. 6. Plot of STEG efficiency versus the concentrator diameter for its different thicknesses d. 1 – d = 1 mm; 2 – d = 0.8 mm; 3 – d = 0.6 mm; 4 – d = 0.4 mm;5 – d = 0.2 mm.

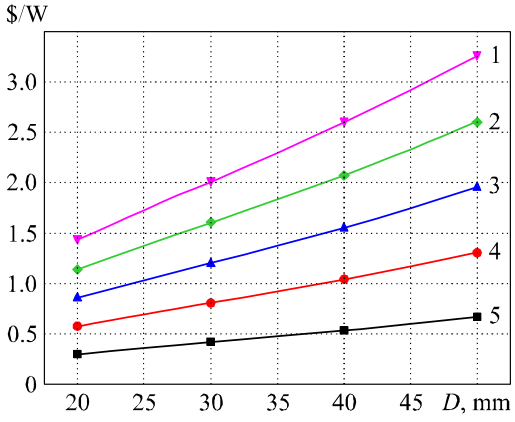

Fig. 7. Plot of the cost of 1 W generated by STEG versus the concentrator diameter for its different thicknesses d. 1 – d = 1 mm; 2 – d = 0.8 mm; 3 – d = 0.6 mm; 4 – d = 0.4 mm; 5 – d = 0.2 mm.

The generator economic parameters have been estimated. Fig. 7 shows the plots of 1 W of electric power generated by STEG versus its geometric dimensions. As can be seen from the plot, for the concentrator thickness 0.2 mm and diameters *D* from 20 to 35 mm, its cost is about 0.5 $/W. Such

parameters make STEG competitive in the market of solar energy converters.

It should be noted that further increase in STEG efficiency is possible due to the use of thermoelectric materials with higher *ZT* value, mirrors with better reflection and protective glass with better transmission, as well as selective coatings for reduction of radiation losses.

Conclusions

1. Object-oriented computer simulation has been used for design optimization of a solar thermoelectric generator which allowed increasing the generator efficiency to the value of 4.67 %.
2. It has been established that account of contact resistances in computer model allows improving the accuracy of calculations of the energy characteristics of a solar TEG by 8 %.
3. The possibility of creating STEG has been established. The cost of 1 W of its generated electric energy power can be about 0.5 $, making it competitive in the market of solar energy converters.

References

1. L.I. Anatychuk, *Thermoelements and Thermoelectric Devices: Handbook* (Kyiv: Naukova Dumka, 1979), 768 p.
2. L.I. Anatychuk, Rational areas of investigation and application of thermoelectricity, *Journal of Thermoelectricity.* **1**, 3 – 14 (2001).
3. L.I. Anatychuk, Current status and some prospects of thermoelectricity, *Journal of Thermoelectricity.* **2**, 7 – 20 (2007).
4. A.S. Bernshtein, *Thermoelectric Generators* (Moscow: Gosenergoizdat, 1956), 47 p.
5. M. Telkes, *J. Appl. Phys*. **25**, 765 (1954).
6. Daniel Kraemer, Bed Poudel, Hsien-Ping Feng, J. Christopher Caylor, Bo Yu, Xiao Yan, Yi Ma, Xiaowei Wang, Dezhi Wang, Andrew Muto, Kenneth McEnaney, Matteo Chiesa, Zhifeng Ren, and Gang Chen, *Nature Materials* **10**, 532 – 538 (2011).
7. Ernesto E. Gomez, *Patent No. US 4251291* (1981).
8. E.P. Gladskikh, V.A. Katenin, V.A. Maksimov, *Patent No. Ru 2382935 C1* (2010).
9. A.N. Timofeev, A.V. Timofeev, D.V. Timofeev, M.A. Timofeev, *Patent No. Ru 86247 U1* (2009).
10. John Gotthold, Anjun Jerry Jin, and Frank M. Larsen, *Patent No. US 2010/0252085 A1* (2010).
11. R. Amatya and R.J. Ram, *J. Electronic Materials* **39** (9), 1735 – 1740 (2010).
12. L.I. Anatychuk, Yu.M. Mochernyuk, Solar Generator of Heat and Electricity, *Patent UA 73624* (2012).
13. L.I. Anatychuk, A.V. Prybyla, The effect of heat exchange system on thermoelectric generator efficiency, *Journal of Thermoelectricity.* **4**, 80 – 85 (2012).
14. *COMSOL Multiphysics User's Guide* (Comsol, Inc., 2006), 708 p.
15. L. Klind, W. Klein, *Glass in Construction: Properties. Applications. Calculations* [transl. from German by P.I. Glazunov, T.F. Guseva, and Z.A. Lipkind] (Moscow: Stroiizdat, 1981), 287 p.
16. Aluminum, Properties and Physical Metal Science: Handbook. Ed. by G.E. Hatch [transl. from English by E.Z. Nepomnyaschaya] (Moscow: Metallurgiya, 1989), 424 p.
17. A.I. Kopyl, I.I. Pavlovich, I.S. Termena, Thermoelectric properties of *p*-$(Bi_2Te_3)_{0.25}(Sb_2Te_3)_{0.72}(Sb_2Se_3)_{0.03}$ *Pb*-doped semiconductor generator material with excess tellurium, *Journal of Thermoelectricity.* **1**, 37 – 42 (2007).
18. L.T. Strutynska, Vibration effect on the homogeneity of Bi_2Te_3 based thermoelectric materials grown by vertical zone melting technique, *Journal of Thermoelectricity.* **4**, 53 – 58 (2012).

Submitted 24.07.2013.

L.I. Anatychuk, V.Ya. Mykhailovsky, A.F. Semizorov,
L.T. Strutynska, A.F. Kashtelyan, N.V. Maksimuk

Institute of Thermoelectricity
NAS and MES of Ukraine, 1, Nauky Str.,
Chernivtsi, 58029, Ukraine

CATALYTIC HEAT SOURCE WITH A THERMOELECTRIC GENERATOR

The results of research and development of a self-contained catalytic heat source with a thermoelectric generator used to achieve improved efficiency and ecological purity of the catalytic combustion of gas organic fuels are presented. An estimate is made and comparative analysis of characteristics of catalytic heat sources is performed and the ways for improving their efficiency are determined. Construction of a diffusion catalytic heat source with a thermal generator is described with the results of experimental research and parameter optimization, as well as the rational application areas of such heat sources are given.
Key words: catalytic heat source, thermoelectric generator.

Introduction

At the present time flame combustion of organic fuel is the main method of thermal energy production for commercial and domestic use. In so doing, the efficiency of using fuel chemical energy is rather low, as long as heat losses with such fuel combustion in a number of cases can reach 30 to 40 %. Moreover, the use of flame combustion deteriorates the ecological parameters. The content of toxic substances (nitrogen and carbon oxides) in fuel combustion products can reach 20 to 50 mg/m^3 and 100 to 500 mg/m^3, respectively [1, 2]. This is several orders higher than the norms of near-earth maximum allowable concentrations of respective substances in the populated area (Table 1) [3].

For gas fuel combustion and heat production use is also made of infrared flameless radiators whose radiation spectrum is 0.5 to 3 μm, the temperature of ceramic nozzle where fuel is burnt reaches 800 to 1200 °C [4]. Such devices retain the disadvantages of flame burners, so they are of limited application.

Table 1

Maximum allowable concentrations and relative hazard figures of substances

Substance	Maximum one-time concentration, mg/m^3	Average daily concentration, mg/m^3	Relative hazard
Carbon oxide	5	3	1
Hydrocarbons	5	1.5	2
Nitrogen oxide	0.4	0.06	50
Nitrogen dioxide	0.09	0.04	75

Long-wave radiators with a lower temperature of heat-releasing surface (200 – 600 °C) are mostly used for heating shops, hangars, gymnasiums, etc. [5]. They also employ flame combustion of gas. Such heaters need electric energy for their operation, which restricts their use for a self-contained

supply of consumers with thermal energy.

In terms of ecological purity and safety the most promising method is catalytic flameless combustion of gas fuel in devices with separate fuel and air delivery to combustion area [6]. Fuel combustion on the catalyst is realized at a temperature of 300 to 600 °C without considerable air excess, which allows reduction of heat losses and considerable reduction of CO and NO_X [5]. In such heat sources gas comes to the catalyst under little pressure, and the air necessary for combustion penetrates porous catalyst bed by natural diffusion. The amount of input air is not controlled, so maximum gas flow rate under natural air diffusion is limited by catalyst value 0.25 g/cm^3. In this connection, diffusion catalytic heat sources have a low calorific power and large dimensions.

Catalytic heat sources with a separate delivery of reagents are used for heating amenity spaces, equipment, devices, and drying paint coatings [7-11]. Space heating is done by natural circulation of air heated by catalyst. In so doing, fuel combustion products H_2O and CO_2 remain in the room which deteriorates the ecological parameters of heated space and calls for its efficient ventilation. The purpose of this work is to increase the efficiency and improve the ecological parameters of flameless catalytic heat sources with a separate delivery of combustible gas and fuel to the catalyst.

Results of development and research on parameters of a catalytic heat source with a thermoelectric generator

Increase in fuel combustion efficiency and calorific power of catalytic heat sources with a separate delivery of reagents can be achieved by intensification of mass exchange processes in catalyst bed [12]. A number of factors that affect gas mixture flow in porous catalyst bed have been determined:

1 – gas pressure due to forced delivery of combustible gas directed from the internal catalyst surface to the external (radiant) surface and the resulting transverse eddy agitation of gases in catalyst bed;

2 – diffusion of gases, in particular combustion oxygen, which is more intensive as compared to other gases, as long as oxygen burns out in catalyst bed and, as a result, high concentration gradient of O_2 is retained (about 21 % near to catalyst radiant surface and close to zero near the internal surface);

3 – temperature convection of hot gases (O_2, CO_2, H_2O, N_2) moving in catalyst bed and along the catalyst vertical radiant surface.

A schematic of gas flow in a catalytic heat source is represented in Fig. 1.

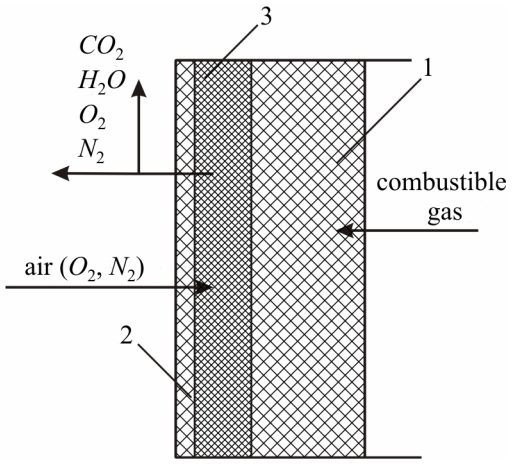

Fig. 1. Schematic of gas flow in a catalytic bed of heat source: 1 – catalyst; 2 – catalyst radiant surface; 3 – combustion area.

It is rather difficult to control oxygen diffusion to catalyst bed, since it depends on O_2 concentration gradient over the thickness of operating catalyst bed. It should be taken into account here that oxygen diffuses to catalyst bed opposite to combustion products, which reduces its concentration in combustion area. Oxygen concentration is also reduced due to the fact that atmospheric nitrogen does not burn out and its concentration in catalyst surface layers is higher than in the air, which further reduces the concentration of O_2 diffusing into catalyst bed.

Special investigations have established that forced air cooling of catalyst radiant surface brings about considerable increase of oxygen concentration over the thickness of catalyst bed (Fig. 2, curves 1, 2). Hydrocarbon concentration in catalyst bed is reduced accordingly (curves 3, 4). It should be noted that a reduction in combustible gas concentration occurs not as a result of its dilution by other gases, but due to increase in the specific amount of combustible gas. For the investigated composition of (Co-Cr-Ni-Pd/SiO_2) catalyst the amount of burnt gas (propane-butane) is increased from 0.25 g/cm^3 to 0.35 g/cm^3 of the catalyst. In so doing, the catalyst temperature in combustion area is increased by 30 to 50 °C, which finally allows increasing the calorific power of catalyst volume unit by a factor of 1.2 to 1.3.

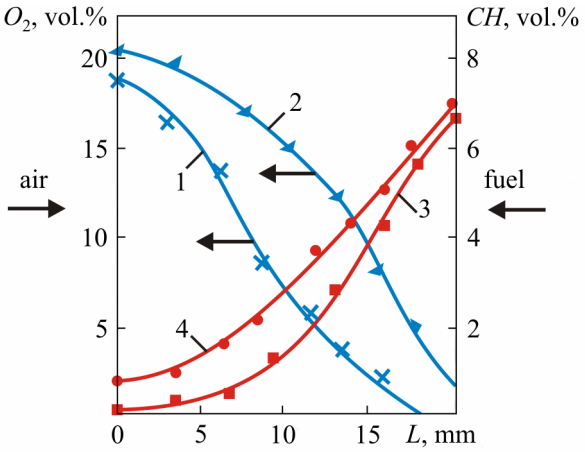

Fig. 2. Concentration profile of oxygen (1, 2) and combustible gas (3, 4) over the thickness of catalyst bed (L) with a natural air diffusion to catalyst bed (1, 4) and forced air cooling (2, 3).

The results of research have been implemented in a concrete construction of a catalytic heat source using separate delivery of reagents to the catalyst and forced air cooling of catalyst radiant surface via electric fan powered from thermoelectric generator. The schematic and outside view of the 1 kW catalytic heat source are given in Fig. 3.

Catalytic heat source consists of a catalyst 1, distribution gas chamber 2 and heat sink 3 that has vertical fins 4 for heat removal from the catalyst and fins 5 for heating the air that heats the space. Arranged in the lower part of heat sink 3 is thermoelectric generator 6 that has the hot 7 and cold 8 heat sinks.

The electric power of thermal generator is 1.5 – 2.5 W. A start-up burner 9 with thermocouple 10 is placed between the fins of the hot heat sink. Forced air delivery for gas combustion and space heating is done by electric fan 11 powered from thermal generator 6. Start-up and control of the catalytic heat source operation is done through gas automation 12. The upper part of the heat source accommodates collector 13 for the removal of gas combustion products to the environment and collector 14 for heated air outlet.

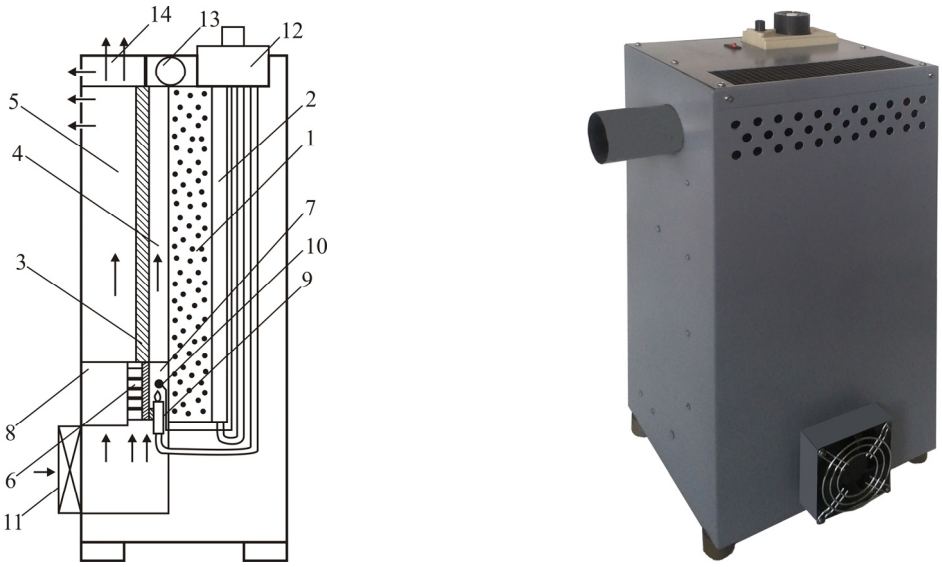

Fig. 3. Schematic and outside view of gas-fueled catalytic heat source with a thermoelectric generator: 1 – catalyst; 2 – distribution chamber; 3, 4, 5 – air heat sink; 6 – thermal generator; 7 – generator hot heat sink; 8 – generator cold heat sink; 9 – start-up burner; 10 – thermocouple; 11 – fan; 12 – gas automation; 13, 14 – collectors.

The specific feature of the elaborated catalytic heat source is that air flow created by the fan is distributed into two flows. Air necessary for gas combustion passes between fins 4 of heat sink 6 to catalyst surface, and then is removed through collector 13 and chimney to the environment together with combustion products. The second air flow moving between fins 5 of heat sink 6 is heated and in its pure form (not contaminated with combustion products) it comes through collector 14 for space heating.

The results of experimental research on parameters of a catalytic heat source with a thermal generator are given in Fig. 4.

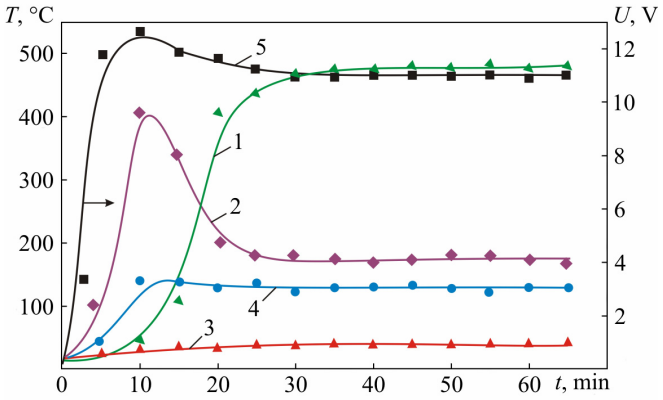

Fig. 4. Time dependence of catalyst temperature (1, 2), thermal generator cold heat sink temperature (3), hot heat sink temperature (4) and thermal generator voltage (5).

It is obvious that the time dependence of catalyst temperature is of complicated nature. In the initial operating period the temperature of lower catalyst part with a start-up burner rises quickly (curve 2) and passes through the maximum within 370 to 400 °C. On achievement of maximum temperature in the lower catalyst part, there is quick temperature rise in the upper catalyst part (curve 1) and is stabilization on the level of 450 – 480 °C. At such catalyst the temperature process of thermal generator hot heat sink is 130 to 140 °C (curve 4), cold heat sink – 30 to 40 °C (curve 3), and

the generator voltage output is 11 to 11.5 V (curve 5)

The electric power of thermal generator with temperature difference between the hot and cold sides 90 to 100 °C is on the level of 2.0 to 2.5 W. This is enough for power supply of electric fan used for forced air cooling of catalyst radiant surface and heated air delivery for space heating. Thus, the optimal rate of air flow in heat sink channels for heat removal from the catalyst is 1 m/s, the hot air temperature for space heating is 70 to 90 °C, and the temperature of combustion products removed by chimney to the environment is 100 to 110 °C.

Conclusions

The use of forced air delivery to the radiant surface of a catalyst of diffusion heat source increases considerably oxygen concentration in catalyst bed, which allows increasing the calorific power of catalyst unit volume by a factor of 1.3 on retention of 100 % completeness of gas fuel combustion. The use of thermoelectric generator assures autonomous delivery of thermal energy to consumers and improves the ecological parameters of heated spaces.

Catalytic heat source with a thermoelectric generator can be used for heating of living spaces and workrooms, greenhouses, garages, trading kiosks, hangars, etc.

References

1. T.B. Janheman, The Development of Atmospheric Burners with Respect to Increasing Emission Rectification, *Proceedings of First European Conference on Small Burner Technology and Heating Equipment,* Vol. 1, P. 23 – 34 (Zurich, September, 25-26, 1996).
2. V.A. Kirillov, N.A. Kuzin, and A.V. Kulikov, The Use of a Catalytic Method for Oxidation of Hydrocarbon Gases for Heat Production in Residential-Grade Thermal Engineering*, Thermal Engineering* **1**, 18 – 22 (2000).
3. V.A. Malyarenko, *Power Plants* (Kharkiv: Saga, 2008), 133 p.
4. Yu.P. Sosnin, U.N. Bukharki, *Household Ovens, Fireplaces and Water Heaters* (Moscow: Stroiizdat, 1984), 368 p.
5. V.Ya. Mykhailovsky, The Prospects of Using Catalytic Sources of Heat and Electricity, *Reports of the National Academy of Sciences of Ukraine (Dopovidi NANU)* **4**, 111 – 115 (2002).
6. V.Ya. Mykhailovsky, Catalytic heat and electricity generators as the way to optimal utilization of hydrocarbon fuel energy, *Journal of Thermoelectricity,* **2**, 3 – 11 (2001).
7. V.Ya. Mykhailovsky, Thermoelectric microgenerators with catalytic propane-butane combustion, *Journal of Thermoelectricity,* **4**, 83 – 86 (2002).
8. L.I. Anatychuk, V.Ya. Mikhailovsky, L.T. Strutinskaya, Catalytic generators of thermal and electric energy on gaseous fuel, *Journal of Thermoelectricity*, **4**, 72 – 80 (1999).
9. L.I. Anatychuk, Rational areas of investigation and application of thermoelectricity, *Journal of Thermoelectricity.* **1**, 3 – 14 (2001).
10. L.I. Anatychuk, Current status and some prospects of thermoelectricity, *Journal of Thermoelectricity.* **2**, 7 – 20 (2007).
11. V.Ya. Mikhailovsky, Heat Sources with Catalytic Combustion of Hydracarbons for Thermoelectric Generators, *Journal of Thermoelectricity*, **1**, 51 – 58 (1993).
12. V.Ya. Mykhailovsky, Organic-Fueled Thermoelectric Generators, *Thesis for a Degree of Doctor in Physics and Mathematics* (Chernivtsi, 2007), 315 p.

Submitted 14.08.2013.

T.A. Ismailov, O.V. Yevdulov, M.A. Khazamova, D.A. Gidurimova

Federal State Budget Educational Institution of Higher Professional Education
"Dagestan State Technical University", 70, Imam Shamil Ave.,
Makhachkala, 367015, Russia

EXPERIMENTAL INVESTIGATIONS OF THERMOELECTRIC DEVICE FOR THE THERAPY OF WHITLOW

The paper is concerned with the results of experimental investigations of prototype thermoelectric device for the therapy of whitlow. The device construction, the test bench, as well as the results of full-scale experiment in the form of plots of time history of temperature at device control points under different operating modes are presented.
Key words: thermoelectric device, whitlow, test bench, full-scale test, thermopile, temperature.

Introduction

In recent years there have been a growing number of suppurative inflammatory hand diseases, namely all kinds of whitlows and phlegmons. Suppurative diseases of fingers and hand rank first in frequency among all suppurative processes. From all newly-admitted patients who apply to surgeon those with whitlows and hand phlegmons make up from 15 % to 31 % [1]. The results of traditional surgical treatment of suppurative open fractures of finger bones and hand cannot be recognized satisfactory because of frequent repeated surgeries (17.1 %), amputations of fingers (7.1 %) and adverse functional and aesthetic outcomes. Repeated surgeries result in patients' invalidity. Hand injuries account for about 1/3 of all traumas of locomotor system, reaching in some industrial fields up to 70 %.

Treatment of suppurative diseases is a complicated therapeutic process aimed at regulating local and general disease manifestations, as well as at suppressing and liquidating pathogenic agents, correcting homeostasis, stimulating immune and reparative processes.

Based on the analysis of the references, the following methods for treatment of suppurative diseases of hand fingers have been revealed.

For the therapy of early forms of whitlow and hand phlegmon, procedures based on using various hot baths with curative solutions are employed [2]. For instance, 5 % propolis water at a temperature of 311 K [3], as well as potassium permanganate solution at a temperature of 310 – 312 K can be used [4]. However, it is known that hot baths, irrespective of the composition of aqueous medium, contribute to oedema of inflammatory tissues of fingers and hand, increase congested effects in the focus of inflammation, affect microcirculation, contribute to forced accumulation of metabolic products in the area of inflammation and in general have a negative impact on the results of therapy.

Similar to the above treatment option is naphthalan therapy, ozokeritotherapy and paraffin therapy, when heated peloid-like substances, namely naphthalan oil, ozokerite and paraffin, are applied to affected areas [1]. In so doing, said treatment options also have the disadvantages considered above.

For conservative therapy of whitlow use is also made of novocaine blocks, infiltration of the focus of damage with 1 % dioxydine solution, *X*-ray therapy, i.e. radioactive cobalt application, ultrasound, laser beams [2, 5]. However, because of ethiopathogenetic invalidity of curative effect of

the above mentioned means, their low therapeutic efficiency, awkwardness and technical complexity of application they have not gained widespread application in treatment practice.

Conservative treatment of the initial forms of whitlow is realized with the use of local prolonged hypothermia [6]. The local prolonged hypothermia in serous-infiltrative phase of whitlow and hand phlegmon possesses powerful ethiopathogenetic curative effect and allows clinical differentiation of serous infiltration phase from suppurative inflammatory changes in tissues. The most common treatment methods in this case are considered to be cold applications, cryogel, ice massage, cold bath (water temperature about 273 K), cold pack, the use of cryoaerosols, etc. [7].

Here it should be noted that technical implementation of these methods is insufficient. The disadvantages of existing modern hypothermia means include the absence of precise temperature control and duration of exposure, impossibility of cold and heat alternation, "non comfort" appreciation of procedures by patients. In this connection it is reasonable to develop new systems and devices for performance of such procedures having high operational performance. According to their mass-dimensional, reliability and energy parameters, thermoelectric power converters that have not been studied yet in terms of using in this technical field are suitable for creation of such systems.

The purpose of this work is to conduct full-scale test of prototype thermoelectric device for the therapy of whitlow developed by the team of laboratory of semiconductor thermoelectric instruments and devices of Federal State Budget Educational Institution of Higher Professional Education "Dagestan State Technical University" [8], as well as to study and analyze the results obtained.

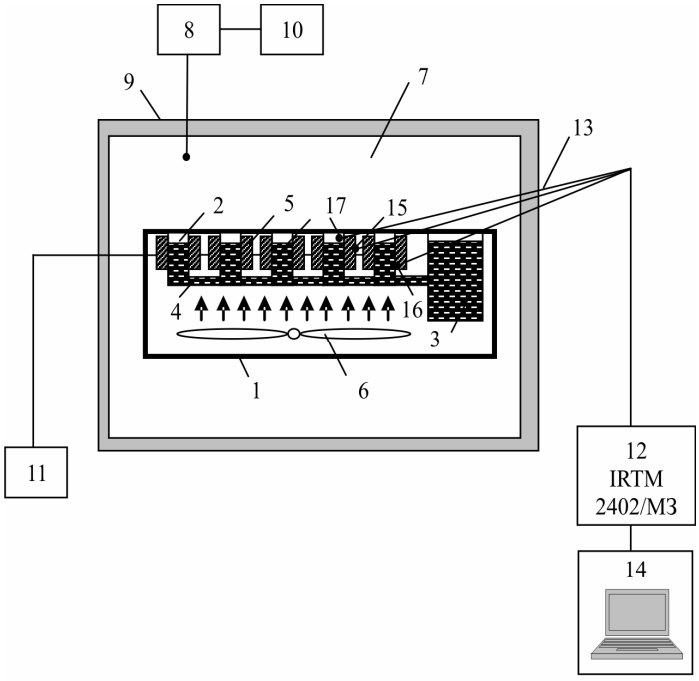

Fig. 1. Schematic circuit of test bench.

The object of experimental research was prototype thermoelectric device (Fig. 1) consisting of a case 1, with openings provided in its upper part, to which metal glasses 2 for human fingers are soldered. The glasses are arranged so as to enable one to sink fingers into them. Case 1 also has a vessel 3 for the curative solution imitator. Vessel 3 via tubes 4 is connected to all glasses 2 similar to communicating vessels. The working junctions of thermopile 5 are connected to the external surface of glasses 2 with provision of thermal contact. The reference junctions of thermopile 5 are blown by air flow forced by unit 6. As a thermopile during full-scale test of device prototype, standard

thermoelectric modules of TB-63-1.0-2.0 thermopile type were used (manufactured by Kryotherm engineering-production firm [9]). The device is shown in Fig. 2. Aqueous solution of potassium permanganate was used as curative solution imitator.

For performance of experimental investigations the prototype thermoelectric device was placed into a thermally insulated climatic chamber 7, the temperature and relative humidity in which is regulated by control unit 8 connected to temperature and humidity sensor 9 whose readings are recorded by digital information display 10. The thermopile was powered by electric supply 11. The measurements were performed with the use of ammeter and voltmeter embedded into electric supply, as well as IRTM 2402/M3 multi-channel meter 12 connected to a personal computer.

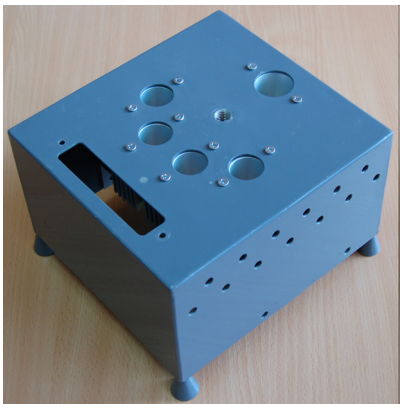

Fig. 2. Prototype thermoelectric device for the therapy of whitlow.

In the course of the experiment there were determined voltage and current on thermopile, ambient temperature, temperatures at control points of the prototype thermoelectric device. Temperature measurement was performed using copper-constantan thermocouples 13 whose reference junctions were arranged in a Dewar vessel, and the signal was picked up by IRTM 2402/M3 meter 12 and output to personal computer 14. Thermocouples 13 were arranged at control points, namely on thermopile reference junctions 15 and working junctions 16, in the curative solution imitator 17.

Prior to the performance of the experiment the reliability of thermal and electric contacts was checked. The experiments were performed in series, 5 experiments each, under identical conditions. The ambient temperature was assigned equal to 296 K, the relative humidity – 55 %.

Figs. 3 and 4 show the plots of time history of temperature at control points of thermoelectric device with thermopile operated in cooling and heating mode for its current supply value equal to $I = 1.8$ A. Considered is time history of the temperature of the thermopile working and reference junctions, as well as the curative solution imitator. According to the represented data, temperature variation, both in the case of cooling and heating of the curative solution imitator is of a monotonous character, decreasing in the former case and increasing in the latter, tending to certain steady-state value. With the stipulated thermopile supply current and the respective operating conditions of thermoelectric device, the temperature at control points takes on given steady-state value in about 7 – 7.5 min, which corresponds to the obtained theoretical results. In so doing, the difference in temperatures between the thermopile working junctions and the curative solution imitator on reaching the steady-state mode by the system is about $2.5 \div 3$ K. This fact enables one to speak about minor thermal losses in the elaborated device and its sufficiently high energy characteristics.

Figs. 5 and 6 show the curves describing time history of the curative solution imitator temperature with the thermopile operated in cooling and heating mode for different supply current values. For heating mode the value of current strength was 2.2 A, 1.8 A, 1.4 A, and for cooling mode – 1.8 A, 1.3 A, 1.1 A, respectively. According to given dependences, increase in the value of thermopile supply current results in reduction of the curative solution imitator temperature with thermoelectric device operated in cooling mode and a rise in its temperature with thermoelectric device operated in heating mode, which corresponds to increase in cooling capacity and calorific power of thermopiles. Thus, increase in thermopile supply current from 1.4 A to 2.2 A on cooling the curative solution imitator, reduces its temperature from 281 K to 276 K, and, on heating, increase in thermopile supply current from 1.1 A to 1.8 A increases the temperature of biological object from 313 K to 317 K.

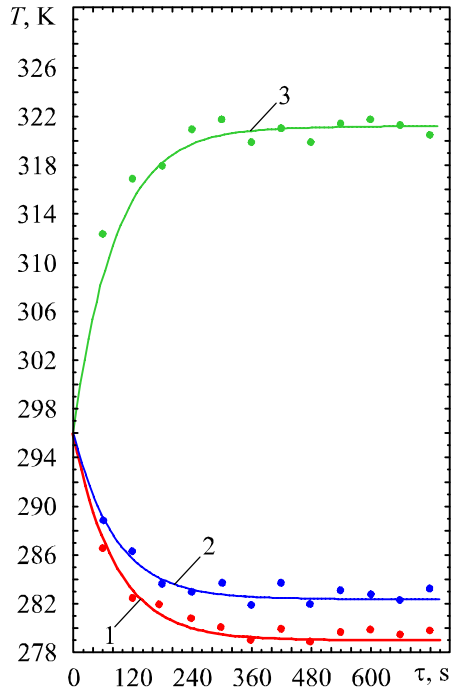

Fig. 3. Time history of temperature at control points of thermoelectric device with the thermopile operated in cooling mode for I = 1.8 A. 1 – working (cold) junction of the thermopile, 2 – curative solution imitator, 3 – reference (hot) junction of the thermopile.

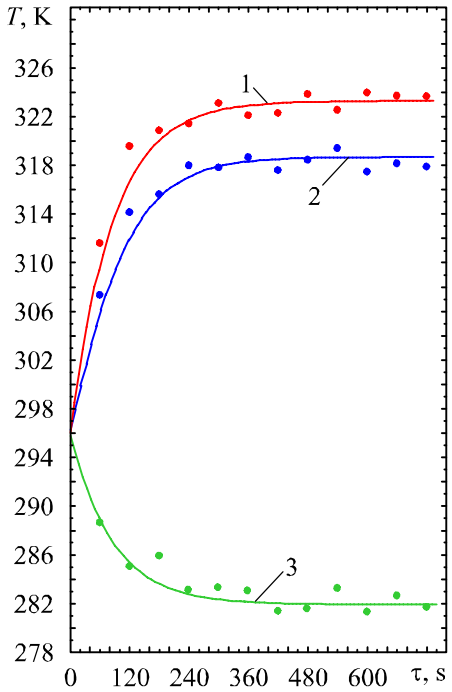

Fig. 4. Time history of temperature at control points of thermoelectric device with the thermopile operated in heating mode for I = 1.8 A. 1 – working (hot) junction of the thermopile, 2 – curative solution imitator, 3 – reference (cold) junction of the thermopile.

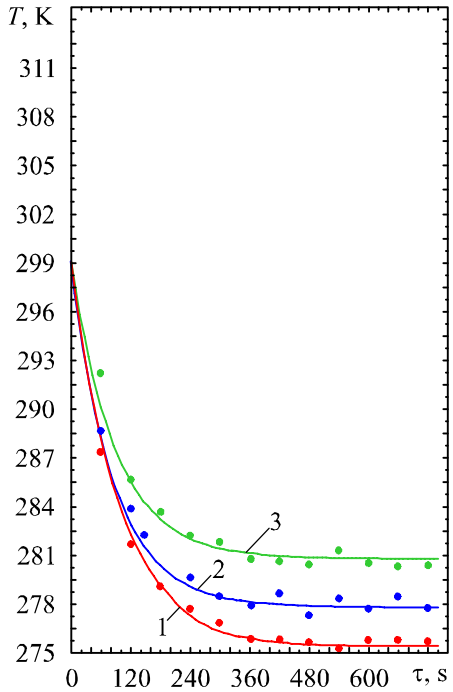

Fig. 5. Time history of the curative solution imitator temperature with the thermopile operated in cooling mode for different values of supply current 1 – I = 2.2 A; 2 – I = 1.8 A; 3 – I = 1.4 A.

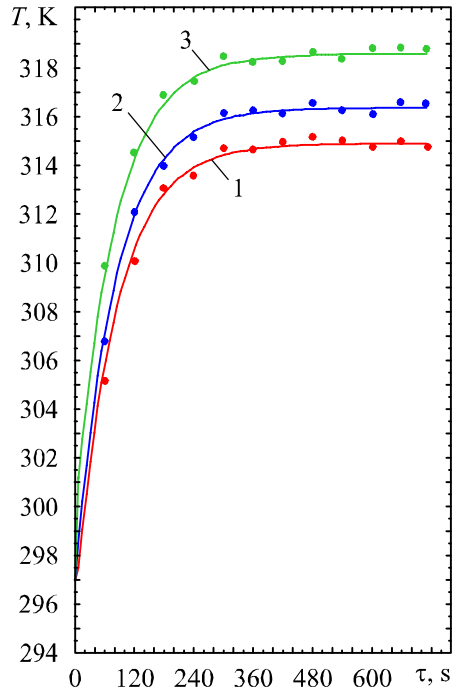

Fig. 6. Time history of the curative solution imitator temperature with the thermopile operated in heating mode for different values of supply current 1 – I = 1.1 A; 2 – I = 1.3 A; 3 – I = 1.8 A.

Thus, according to the experiment, for the implementation of required medical procedures determined primarily by the temperature of the curative solution imitator, the use of a standard thermoelectric module of TB-63-1.0-2.0 thermopile type is quite justified.

To analyze the possibilities of dynamic operating mode of thermoelectric device, the plots of time history of the curative solution imitator temperature with a change of device operation from cooling to heating mode and vice versa, are given in Figs. 7 and 8. In the first case the results are given for thermopile supply currents 1.2 A, 1.5 A and 1.8 A, in the second case – for supply currents 1.4 A, 1.6 A and 1.8 A. The experimental findings also correspond to calculation data. In both cases the duration of transition from cooling to heating mode and vice versa is of the order of 8 minutes, which corresponds to theoretical calculations with adequate accuracy.

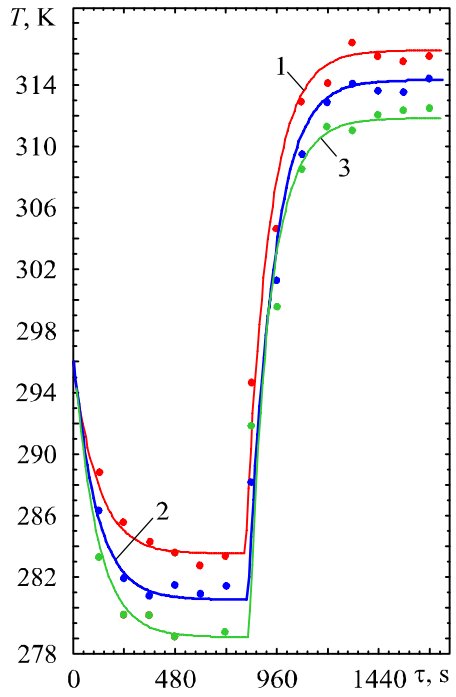

Fig. 7. Time history of the curative solution imitator temperature at contrast thermal procedure with thermoelectric device passing from cooling to heating mode for different values of thermopile supply current 1 – I = 1.8 A; 2 – I = 1.5 A; 3 – I = 1.2 A.

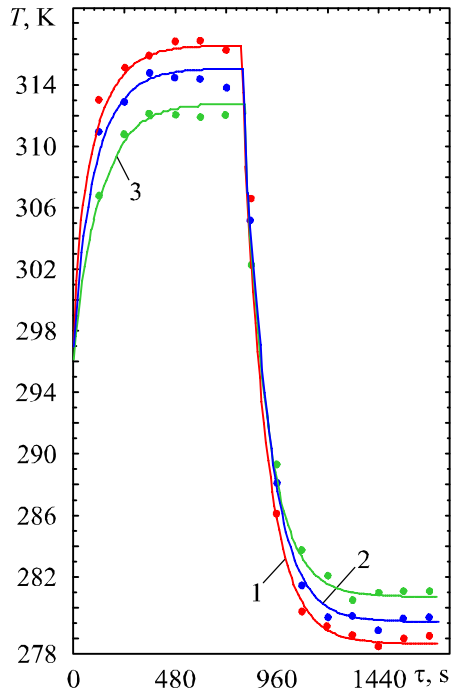

Fig. 8. Time history of the curative solution imitator temperature at contrast thermal procedure with thermoelectric device passing from heating to cooling mode for different values of thermopile supply current 1 – I = 1.8 A; 2 – I = 1.6 A; 3 – I = 1.4 A.

Fig. 9 represents the data related to time history of the biological object and the curative solution imitator temperature with thermopile operated in cooling and heating mode for $I = 1.8$ A. According to represented data, the temperatures of the curative solution imitator and the biological object as such do not correspond to each other. It is primarily due to finite values of heat capacity and thermal conductivity of the biological object, as well as to its internal heat release. For the investigated conditions the difference in temperature values of the biological object and the curative solution imitator is about 3.5 K.

Reliable operation of the elaborated thermoelectric device depends in many respects on the efficient heat pickup from the thermopile reference junctions. To estimate the possibilities of heat pickup from the thermopile hot junctions in the system, Fig. 10 represents the data on the time history of device base temperature under cooling effect for different values of thermopile supply currents.

From the represented plots it follows that the temperature value of thermopile hot junctions is quite

acceptable for the type of standard modules employed. This fact determines rather efficient heat pickup from the thermopile hot junctions under conditions being considered and gives grounds to suppose a reliable operation of the elaborated device when conducting the required medical procedures.

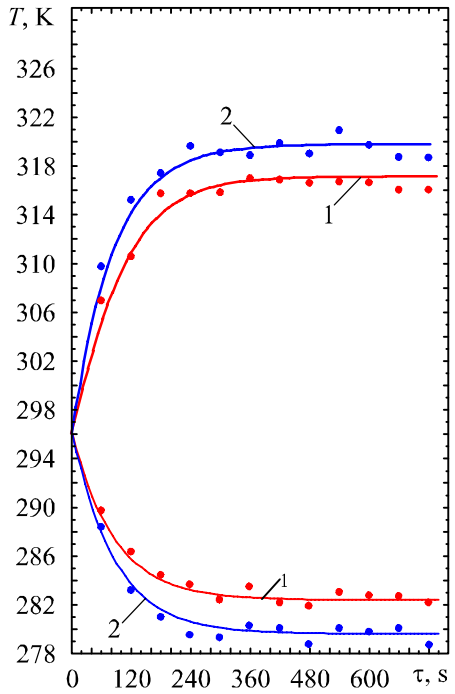

Fig. 9. Time history of biologic object (1) and the curative solution imitator (2) temperature with the thermopile operated in cooling and heating mode for I = 1.8 A.

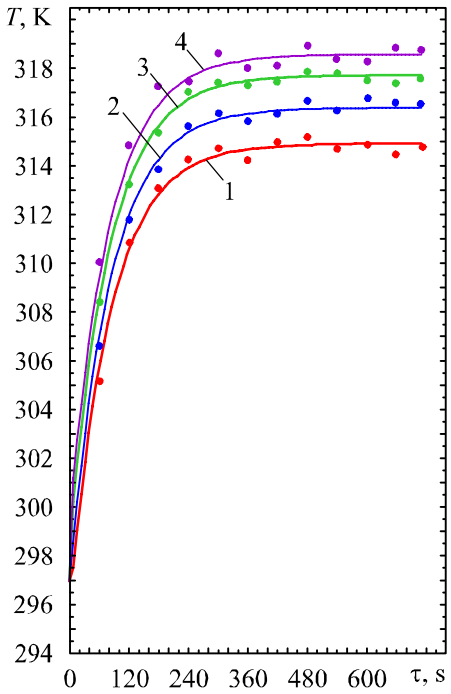

Fig. 10. Time history of the thermopile hot junction temperature when operated in cooling mode for different values of supply current 1 – I = 1 A; 2 – I = 1.2 A; 3 – I = 1.4 A; 4 – I = 1.6 A.

According to the results of the experiments, comparison of the design and experimental data has been conducted. Apart from the experimental points, Figs. 3 to 10 represent the results of theoretical research.

The represented research results determine the acceptable coincidence of the theoretical and experimental data. Their maximum divergence does not exceed 5 – 6 %. The greatest deviation of calculated data from the experiment is mainly observed on the time interval related to reaching the mode by the system which is determined by the environmental influence and non-perfect thermal insulation of "device-object" system, as well as certain spread in thermopile and measuring instrument parameters. In so doing, in case of cooling the experimental results have somewhat larger values than the calculated ones, and in case of heating – the lowest values over the entire measurement range. This fact is mainly due to imperfection of thermal insulation, which does not meet the requirements accepted in the design models, hence, heat penetration to the device.

Thus, based on the research performed, the following conclusions can be made:

1. Hypothermia method based on the thermoelectric device developed by the authors can be used for conducting medical procedures in the therapy of whitlow.
2. The thermoelectric device is a fast-response one, namely the time of reaching the steady-state working mode in the investigated range is 7.5 minutes.
3. The difference in temperature between the working junctions of thermopile and the curative solution does not exceed 3 K enabling to speak about minor thermal losses in the device.
4. When conducting the required medical procedures, for thermoelectric device it is sufficient to use a

standard thermoelectric module of TB-63-1.0-2.0 type with maximum supply current 2.3 A.

5. With device operated in the dynamic mode, the process of transition from cooling to heating mode and vice versa is of the order of 8 minutes.
6. According to the data obtained, the temperature of the curative solution and the biological object as such do not correspond to each other: in the investigated range the difference in their temperature is 3.5 K.
7. To assure normal operation of thermopile in thermoelectric device, it is sufficient to use forced air cooling.
8. When comparing the calculated and experimental data, their maximum divergence did not exceed 5 to 6 %.

References

1. A.D. Badikov, Application Beta-Therapy in a Combined Treatment of Whitlow on an Outpatient Basis, *PhD Thesis* (Saint-Petersburg, 2005), 146 p.
2. A.V. Meleshevich, *Whitlow and Phlegmon of Hand*, Manual for Surgical Curriculum for Students of all Specialties, in 3 Parts, Part 3 (Grodno, 2002), 264 p.
3. L.A. Komarova, L.A. Blagovidova, *Manual for Physical Methods of Treatment* (Leningrad: Meditsina, 1983), 264 p.
4. Rehabilitation of Patients with some Diseases and Injuries of Hand, *Proceedings of Gorky Research Institute of Traumatology and Orthopedics*, Ed. By V.V. Azolov (Gorky, 1987), 187 p.
5. Masai Taksahani, Clinical Experience of Combined Use of Hyperthermia and Radiation Therapy, *Medical Radiology* **12**, 25 (1988).
6. V.V. Kenz, A.I. Sukhenko, and T.M. Duca, Local Cold Effects in Physiotherapy, *Voprosy Kurortologii (Balneotherapy Issues)* 2, 83 – 87 (1983).
7. D.N. Kadanov, Yu.T. Bozhenkova, and V.I. Ivanov, Treatment of Suppurative Diseases of Soft Tissues by Cryogenic and Cryosurgical Methods in Ambulatory-Care Clinic, *Surgery* **5**, 141 – 143, 1985.
8. T.A. Ismailov, O.V. Yevdulov, M.A. Khazamova, and D.A. Gidurimova, Results of Mathematical Simulation of Thermoelectric Device for Treatment of Hand Fingers, *Thermal Processes in Engineering* **9**, 426 – 432 (2011).
9. http://www.kryotherm.ru.

Submitted 12.07.2013.

NEWS

INTERNATIONAL THERMOELECTRIC ACADEMY

VASYL MYKOLAYOVYCH HODOVANYUK

(DEDICATED TO 60-th BIRTHDAY)

In August this year Vasyl Mykolayovych Hodovanyuk – Doctor of Engineering Science, professor, academician of the Academy of Communications of Ukraine, full member of the Academy of Technological Sciences of Ukraine, corresponding member of the International Thermoelectric Academy, laureate of State Prize of Ukraine in Science and Technology, celebrated his 60-th anniversary.

V.M. Hodovanyuk was born on August 14, 1953 in Chernivtsi. In 1976 he graduated from Physics Faculty of Chernivtsi State University (Department of Thermoelectricity). In 1990 without giving up work he completed postgraduate studies at Chernivtsi Division of Institute for Problems in Materials Science of NAS Ukraine, and in 2000 he took Doctor's degree in Engineering.

Vasyl Mykolayovych started his labour career in 1976 as a process engineer of Central Design Office "Rytm". In subsequent years he held the position of the first deputy director and chief designer of this joint-stock company.

In 1997 he was elected director and chief designer of Open JSC Central Design Office "Rytm" which is the head scientific institution of Ministry of Industrial Policy of Ukraine in the scientific and technical support of direction "Development of solid-state photodetectors, photodetection devices and optically coupled devices".

The scientific works of V.M. Hodovanyuk include over 80 research papers and patents for inventions. In 2009 he co-authored a monograph on theoretical and experimental investigations and developments of modern high-performance devices of photo- and optoelectronics for communications systems.

V.M. Hodovanyuk is high achiever of education in Ukraine, professor of Department for Physics of Semiconductors and Nanostructures of Yu. Fedkovych Chernivtsi National University, deputy head of a Specialized Academic Board for conferring the academic degree of PhD in Engineering in the specialty "Solid State Electronics" and a member of a Specialized Academic Board for conferring the academic Degrees of PhD and DSc in Physics and Mathematics at Chernivtsi National University.

Professor V.M. Hodvanyuk is a member of editorial board of the journal "Tekhnologia i Konstruirovanie v Elektronnoi Apparature", scientific and production journal "Arsenal XXI" and the "Scientific Bulletin of Chernivtsi University. Physics, Electronics".

For the particular contribution to intellectual development of today's society V.M. Hodovanyuk has picked up "International Socrates Award".

International Thermoelectric Academy, Institute of Thermoelectricity of the National Academy of Sciences and Ministry of Education and Science of Ukraine, "Journal of Thermoelectricity" Publishers cordially greet professor Vasyl Mykolayovych Hodovanyuk on his jubilee, wishing him sound health, happiness and new labour achievements.

ARTICLE PREPARATION RULES

The article shall conform to the journal profile. The article content shall be legible, concise and have no repetitions.

The article shall be submitted to the editorial board in electronic version.

The text shall be typed in text editor not lower than MS Word 6.0/7.0.

Page setup: "mirror margins"- top margin – 2.5 cm, bottom margin – 2.0 cm, inside – 2.0 cm, outside– 3.0 cm, from the edge to page header – 1.27 cm, page footer – 1.27 cm.

Graphic materials, pictures shall be submitted in color or, as an exception, black and white, in .opj or .cdr formats, .jpg or .tif formats being also permissible. According to author's choice, the tables and partially the text can be also in color.

The article shall be submitted in English on A4 paper sheets; the number of pages shall not exceed 12. By agreement with the editorial board, the number of pages can be increased.

To accelerate publication of the article, please adhere to the following rules:

- the authors' initials and names are arranged in the centre of the first page at the distance of 1 cm from the page header, font Times New Roman, size 12 pt, line spacing 1.2;
- the name of organization, address (street, city, postal code, country) – indent 1 cm below the authors' initials and names, font Times New Roman, size 11 pt, line spacing 1.2, center alignment;
- the title of the article is arranged 1 cm below the name of organization, in capital letters, semi-bold, font New Roman, size 12 pt, line spacing 1.2, center alignment. The title of the article shall be concrete and possibly concise;
- the abstract is arranged 1 cm below the title of the article, font Times New Roman, size 10 pt, in italics, line spacing 1.2 ,center alignment;
- key words are arranged below the abstract, font Times New Roman, size 10 pt, line spacing 1.2, justified alignment. The title "Key words" – font Times New Roman, size 10 pt, semi-bold;
- the main text of the article is arranged 1 cm below the abstract, indent 1 cm, font Times New Roman. size 11 pt, line spacing 1.2, justified alignment;
- formulae are typed in formula editor, fonts Symbol, Times New Roman. Font size is "normal" – 12 pt, "large index" – 7 pt, "small index" – 5 pt, "large symbol" – 18 pt, "small symbol" – 12 pt). The formula is arranged in the text, centre aligned and shall not occupy more than 5/6 of the line width, formulae are numbered in round brackets right;
- dimensions of all quantities used in the article are represented in the International System of Units (SI) with the explication of the symbols employed;
- figures are arranged in the text. The figures and pictures shall be clear and contrast; the plot axes – parallel to sheet edges, thus eliminating possible displacement of angles in scaling;
- tables are arranged in the text. The width of the table shall be 1 cm less than the line width. Above the table its ordinary number is indicated, right alignment. Continuous table numbering throughout the text. The title of the table is arranged below its number, center alignment;
- references should appear at the end of the manuscript. References within the text should be enclosed in square brackets. References should be numbered in order of first appearance in the text. Examples of various reference types are given below.

– L.I. Anatychuk, *Thermoelements and Thermoelectric Devices: Handbook* (Kyiv: Naukova Dumka, 1979), p.766. (Book)
– T.M. Tritt, Thermoelectric Phenomena, Materials, and Applications, *Annual Review of Materials Research* **41**, 433 (2011). (Journal paper)
– U. Ghoshal, *Proceedings of the XXI International Conference on Thermoelectrics* (N.Y., USA, 2002), p. 540. (Proceedings Conference)

The article should be supplemented by:

• letter from the organization where the work was performed or from the authors of the work applying for the publication of the article;

• information on the author (authors): last name and initials; full name and postal address of the institution where the author works; academic degree; position; telephone number; E-mail;

• author's (authors') photo in color or, as an exception, in black and white. With the number of authors more than two their photos are not given;

• author's application to the following effect:

We, the undersigned authors, … transfer to the founders and editors of "Journal of Thermoelectricity" the right to publish the article…in Ukrainian, Russian and English. This is to confirm that the present publication does not violate the copyright of other persons or organizations.

Date Signatures

Below is given an example of article preparation.

Author's photo 3 × 4 cm

A.I. Casian[1], B.M. Gorelov[2]

[1]Technical University of Moldova,
168, Stefan cel Mare Ave.,
Chisinau, MD-2004, Moldova;
[2]Institute of Surface Chemistry of National Academy
of Sciences of Ukraine, 17, Gen. Naumov Str.,
Kyiv, 03164, Ukraine

Author's photo 3 × 4 cm

STATE OF THE ART AND PROSPECTS OF THERMOELECTRICITY ON ORGANIC MATERIALS

The aim of the paper is to analyze the expected thermoelectric opportunities of organic materials, including some highly conducting quasi-one-dimensional crystals. It is shown that interest of investigators in these materials has been growing recently. Quasi-one-dimensional organic crystals have high prospects for thermoelectric applications. These materials combine the properties of multi-component systems with more diverse internal interactions and of quasi-one-dimensional quantum wires with increased density of electronic states. It is shown that the values of the thermoelectric figure of merit ZT ~ 1.3 – 1.6 at room temperature are expected in really existing organic crystals of tetrathiotetracene-iodide, TTT_2I_3, if the crystal parameters are approaching the optimal ones.

Key words: thermoelectricity, tetrathiotetracene-iodide, polarizability.

Introduction

It is known that conducting organic materials usually have much lower thermal conductivity than the inorganic materials. Moreover, the organic materials can be fabricated by simpler chemical methods, and it is expected that such materials will be less expensive in comparison with the inorganic ones. Exactly these properties attracted attention to such materials for the use in thermoelectric (TE) applications long time ago [1, 2]. In spite of relatively high value of the thermoelectric figure of merit $ZT = 0.15$ at room temperature observed in polycopper phthalocyanine [2] as early as 1980, the thermoelectric properties of organic materials are still weakly investigated. This situation has the only explanation that thermoelectricians are still weakly interested in organic materials, and organic chemists are also weakly interested in thermoelectric materials. Moreover, in order to seek good organic thermoelectrics, it is necessary to organize multidisciplinary consortiums of physicists, organic chemists and engineers in the field of thermoelectricity. …

The aim of this paper is to present briefly the state-of-the-art of investigations in the area of new organic thermoelectric materials and to describe the nearest expected results for really existing quasi-one-dimensional organic crystals of tetrathiotetracene-iodide, TTT_2I_3.

Quasi-one-dimensional organic crystals of TTT_2I_3

The structure of quasi-one-dimensional organic crystals of tetrathiotetracene-iodide, TTT_2I_3, has been briefly described in [34]. These needle-like crystals are formed of segregate chains or stacks of planar molecules of tetrathiotetracene *TTT*, and iodine ions. The chemical compound TTT_2I_3 is of mixed-valence: two molecules of *TTT* give one electron to the iodine chain which is formed from I_3^- ions. The

conductivity of iodine chains is negligibly small, so that only *TTT* chains are electrically conductive and holes serve as carriers. The electrical conductivity σ along *TTT* chains at room temperature varies between 10^3 and $10^4\ \Omega^{-1}\text{cm}^{-1}$ for crystals grown by gas phase method [35], and between 800 and $1800\ \Omega^{-1}\text{cm}^{-1}$ for crystals grown from solution [36]. Thus, the conductivity is very sensitive to crystal impurity and perfection which depends on growth method. In the direction perpendicular to chains σ is by three orders of magnitude smaller than in the longitudinal direction and is neglected. …

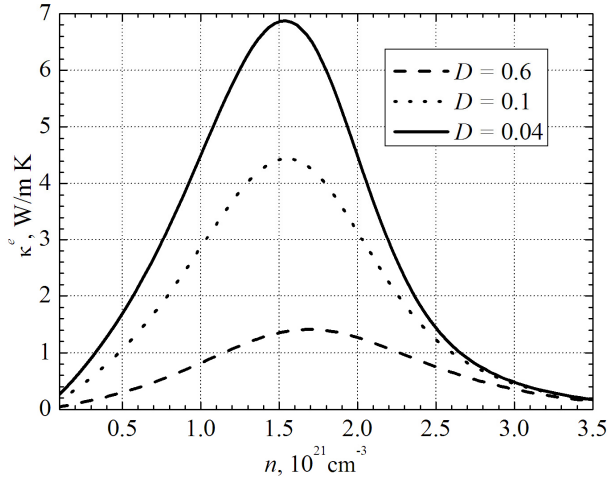

Fig. 1. Dependences of electron thermal conductivity κ^e on n.

$$\sigma = R_0,\ S = R_1 / eTR_0,\ \kappa^e = \left(e^2T\right)^{-1}\left(R_2 - R_1^2 / R_0\right), \tag{1}$$

Thermoelectric properties

Expressions (2) – (3) have been calculated in order to determine the thermoelectric properties of quasi-one-dimensional organic crystals of TTT_2I_3 with different degrees of purity….

Conclusions

The state-of-the-art of research on new organic materials for thermoelectric applications is analyzed. It is shown that the interest of investigators in these materials has been growing in recent years. The highest value of $ZT \sim 0.38$ at room temperature has been measured in doped acetylene, with the only problem that this material is not stable. Accurate control of the oxidation level in poly (3, 4-ethylenedioxythiophene) (PEDOT) gave the power factor $324\ \mu\text{W}\cdot\text{m}^{-1}\text{K}^{-2}$ and in combination with its low intrinsic thermal conductivity ($\kappa = 0.37\ \text{W}\cdot\text{m}^{-1}\text{K}^{-1}$) yielded $ZT = 0.25$ at room temperature, and this material is air-stable….

References

1. Ali Shakouri, Recent Developments in Semiconductor Thermoelectric Physics and Materials, *Annu.Rev.Mater.Res*.**41**, 399-431 (2011).
2. L.I. Anatychuk, *Thermoelectricity, Vol.2, Thermoelectric Power Converters* (Kyiv, Chernivtsi: Institute of Thermoelectricity, 2003), 376p.
3. M.E. Bengen, *German Patent Appl*. OZ 123, 438, 1940; *German Patent* 869,070, 1953, Tech. Oil Mission Reel, 143,135, 1946.

ISSN 1607 - 8829. Journal of Thermoelectricity. 2013. № 4. 1-92